Technical University of Denmark

DTU Artek & DTU Environment

Thesis for the Degree of Master of Science in Environmental Engineering

---

Snow Distribution Statistical Modelling and UAV-borne Remote Sensing of Snow Reflectance in the Arctic

---

August 22, 2015

Authors:

Marco MARCER (s131594) **Baptiste VANDECRUX** (s131053)

Supervisors:

Professor Carl BØGGILD, DTU Artek **Professor Fred SIGERNES**, UNIS

Abstract

The present study is part of a project that aims at mapping snow depth and snow optical properties using Unmanned Aerial Vehicle (UAV) -borne digital photogrammetry. It is organized in two parts, the first part aims at estimating snow distribution from snow depth point measurements by means of regression tree models, and the second at extracting Hemispherical Directional Reflectance Factor of snow from images taken by a digital reflex camera fixed to a UAV.

The objective of the first part is to assess the capacity of regression tree models and of a set of predictors to distribute snow over an area from point measurements and at testing whether they could be used in the future for high resolution snow depth data acquired by UAV-borne photogrammetry. In four sites around Longyearbyen in Svalbard, Norway, snow depth was measured by manual probing or Ground Penetrating Radar. Then a regression tree model was built for each site and for two Digital Elevation Models (5 m and 50 m resolution) to predict snow depth from elevation slope, two wind exposure indexes Sx and Sb, and a radiation index. For all sites except one the 5 m models showed higher R^2 than the 50 m ones indicating that regression trees successfully model snow depth at a small scale. The 5 m snow distribution models give R^2 ranging from 0.39 (4 snow classes) to 0.67 (2 snow classes) which is satisfactory compared to previous studies using regression trees. Most snow distribution models were found to be site specific and could not be applied on other sites. It was addressed to differences of snow distribution processes or to the effect of different snow depth sampling methods. The snow distribution model built in Longyearbyen and snow density data were used to estimate total Snow Water Equivalent (SWE) stored in the snow cover of Longyearbreen glacier. The regression tree model estimated a total SWE value of $8.13 \pm 2.90 \times 10^5$ m^3 and showed an improved precision when compared to the results of a constant snow depth model and of an elevation gradient model. Errors and limitations of the present modelling framework are discussed and suggestions are given for further studies.

In the second part, a method to estimate snow reflectance from UAV-borne digital images is investigated. The approach presented, uses the digital camera to measure luminance in a scene and then estimates the reflectance of a surface by comparing its luminance to the one of a surface of known reflectance in the picture. The calibration of the camera simply relates the camera response to variations in a target brightness, finding a linear relationship between luminance and pixel intensity. It has the advantage of requiring no specific equipment and to avoid the complex calculation of camera spectral sensitivity. Vignetting effect was corrected The camera accuracy is assessed by investigating shot noise and dark current. In the fieldwork conditions, shot noise is found to be the most relevant source of noise and sufficient exposure of the pictures is recommended to reduce its effect. The method was tested during a fieldwork campaign nearby Sisimiut, West Greenland. The UAV is flown vertically up to 7.6 meters and 17 pictures are used to estimate the the reflectance of a snow patch and of a 10% reflective validation surface. The estimated reflectance values of the snow patch range from 0.97 to 0.98 with an uncertainty of 0.04 to 0.08. This data could not be compared to other field measurement because of human mistake in the spectroradiometer measurement of the snow patch reflectance. The estimation of the validation surface reflectance showed that a minimum number of pixels are necessary to determine accurately the reflectance of a surface. Based on a first estimation of this threshold, the estimation of the validation surface reflectance gives a Root Mean Square Error of 0.05 which is relatively high compared to the surface real reflectance. It is attributed to the low brightness of the validation surface which increases noise. The necessity of a reference surface in the picture is discussed and suggestions for future work are given.

Preface

The present master's thesis is presented to DTU Environment and DTU Artek and conducted in collaboration with the University Center of Svalbard (UNIS) and represents 30 ECTS credits. It is supervised by Professor Carl Egede Bøggild from DTU Artek and Professor Fred Sigernes from UNIS.

This study is part of a larger project that was motivated as follows. In Svalbard, West-Greenland and more generally in Arctic regions, snow is the dominant form of precipitation. Thus, in these regions, most of the water resources are stored in the seasonal snow pack and released during a brief summer. Despite that, the planning of hydro-power production and drinking water management, among (many) others, require an estimation of this seasonal water storage, little effort has been made by the company in charge to establish methods for assessing this resource. A simple explanation would be that conventional methods have shown restrictions. Indeed, extensive field survey (manual probing, Ground Penetrating Radar... etc.) uses mainly costly human workforce. Also, remote sensing (airborne radar, LIDAR, satellite observation) makes use of technologies that are not readily available for companies and municipalities such as satellites or of expensive platform such as plane or helicopter.

The recent technological improvement of Unmanned Aerial Vehicles (UAVs) has enabled them to carry heavier payload over greater distances. In parallel, digital cameras also achieve always better results for always lower weight and affordable prices. The combination of these two technologies to survey snow depth lead to the creation of the present project that is divided into three axis. The first one is part of another master's thesis conducted by Emiliano Cimoli while the two others are covered by the present report written by Marco Marcer and Baptiste Vandecrux.

- The first axis of the project is conducted by Emiliano Cimoli also writing his master's thesis at Artek and DTU Environment. His work aims at using the digital images taken from the UAV to generate the Digital Elevation Model (DEM) of the snow surface and of the bare ground (in summer) and hence to map snow depth over an area. In his thesis, E. Cimoli describes the method, quantifies its accuracy and errors and eventually discusses how and how often this method can be used in the Arctic region.

- The second axis of the project investigates means to predict snow depth over an area from snow depth measurements. Indeed, since the autonomy of UAV is not unlimited, it is important to develop a method that uses the snow depth data collected by the UAV to determine snow distribution over a broader area. Therefore the Part I of the present report introduces a statistical model that can predict snow depth over an area from a set of snow depth measurements. Since the present study was conducted simultaneously with Cimoli's, the snow depth data from the UAV were not ready yet when the snow distribution model was developed. Snow depth data, collected with conventional methods (manual probing and Ground Penetrating Radar) were gathered during the winter in order to calibrate the statistical model. The model was then tested for a coarse (50m) and fine (5m) grid resolutions, in order to assess whether this approach could benefit from the high resolution snow depth data that can be acquired by the UAV survey.

- The third axis of the project aims at investigating a method to estimate optical properties of the snow from the digital images taken from the UAV. Indeed, the way snow reflect sunlight can give multiple information about its purity, its grain size or about the snow pack energy balance. Using camera to measure accurately light requires the calibration of the camera and accuracy assessment, a process whose complexity represents a limiting factor in the practical use of this method. Therefore, in part II of the present report

is investigated an alternative approach to estimate snow reflectance from digital images requiring less expertise and equipment. The calibration of the camera is introduced and snow reflectance is estimated in a first step from a single pictures where a reference surface is visible. Due to time limition, only one month and a half, out of the six months attributed to the Master's thesis could be dedicated to this part of the study. The presented work has to be considered as a preliminary study of a technology that ultimately is expected to furnish digital maps of snow surface properties estimated from UAV-borne digital imaging. In this sense, recommendations and future work possibilities are given.

Thus each axis represents an independent study that are nevertheless linked by the use of the same UAV-camera platform.

The field work campaigns in Svalbard and Greenland were conducted in collaboration with Emiliano Cimoli with whom all the tasks were shared. For administrative reasons it was not possible to present one thesis for three students so the separation was decided according to the workload of each part of the project.

Acknowledgement

First, we would like to express our gratitude to our supervisor Professor Carl Egede Bøggild which supported us during the whole thesis and in particular during the fieldwork campaigns.
Our sincere thanks to Professor Fred Sigernes from the University Center of Svalbard (UNIS) which also supervised our project and was a precious help for everything related to optics.
We would like to thank all the staff from DTU Artek and UNIS who gave us support during the entire thesis. Their kindness and availability were very precious to us. Special thanks go to Chris Borstad at UNIS and Martin Kotol at Artek for their great help in the preparation of our fieldworks and to Horst Machguth for the processing of GPR data.
Our thanks and friendship also goes to Timon Brüggemann and Marius Petersen who helped us with their drones. Without their hexacopter and their pilot skills, this project would not have gone very far.
This project was conducted with the financial support of the Research Council of Norway through the Artic Field Grant n°246151 and 246077 for the field work in Svalbard. The fieldwork in Greenland was funded by GrønlandsBanken and by the Society for Arctic Research and Technology (SAFT). Our sincere thanks goes to these institutions who trusted us and gave us the mean to reach our ambitions.
Last but not least, we thank Emiliano Comoli with whom we collaborated closely and shared all the good and bad moments of the fieldwork, as well as all our friends, families and buddinges who supported us during six month of hard work.

Table of Contents

Part I
Snow Distribution Modelling

1 Introduction

The understanding and modelling of how the snow is deposited or transported over topography is of great importance in many regards such as for its control on permafrost sequestration of CO_2 (Brooks et al., 1997; Lloyd et al., 1999); for its importance in global albedo and global climate modelling (Colman et al., 1994); for the vital importance it has on fauna and flora (Bruland and Cooper, 2001; Van Der Wal et al., 2000); for its influence on mountain hydrology (Hartman et al., 1999; Winstral and Marks, 2002), avalanche forecasting (Marsh, 1999; Lehning et al., 2006; Purves et al., 1998), glacier location (Jaedicke and Sandvik, 2001; Dadic et al., 2010) and ice cap mass balance (Sauter et al., 2013). Eventually since in the Arctic, hydro-power plants and drinking water reservoirs mainly depend on melt-water from the winter snow pack, accurate snow distribution models are necessary for a good management of the water resources.

Snow distribution being controlled by various climatic and topographic variables, intensive efforts have been made to predict its spatial distribution as a function of few parameters, easily accessible from weather station data or from topography. Physical models, reviewed non-exhaustively by Wurzer et al. (2010), have been developed to solve the equations governing the transport of snow grains as they roll on the ground (i.e. transport by creep), are projected from one place to another (i.e. transport by saltation) or are carried over long distances by the wind (ie. transport by suspension). These equations require to calculate wind speed and wind direction for every point of the area and consequently give best results when coupled with high resolution atmospheric models (Liston et al., 2007; Lehning et al., 2008). However this approach present some limitations. Indeed complexity of atmospheric modelling requires heavy computing as the resolution and precision increase. Also the interpretation of the result are made more difficult since it cannot be clearly determined which part of these complex models deviates from reality.

Topographical parameters have been used as proxies to describe the control of terrain on wind fields and wind-driven snow distribution and have been used in statistical models to distribute snow over mountainous terrain (Elder et al., 1998, 1995; Balk and Elder, 2000; Winstral and Marks, 2002; Molotch et al., 2005; Lehning et al., 2011; Grünewald et al., 2013). These methods, have shown good result for distributing snow from point measurements but also to predict snow accumulation over whole winter seasons when coupled with a snowpack energy and mass balance model (Winstral and Marks, 2002; Winstral et al., 2013). But these models have the drawback to be statistical, meaning that they learn from the data they are given for calibration and do not explain the underlying physical processes.

In Svalbard, it has been reported that snow depth up to several meters were observed only few meters away from snow free areas (Eckerstorfer and Christiansen, 2011), highlighting a real challenge in the snow distribution modelling framework. An overview of most snow studies has been compiled by Winther et al. (2003). From these, three studies tried to model snow distribution:

- Jeadicke et al. (2000) set up a physical model based on the work from Bang et al. (1994) and Thiis (2000) to describe the snowdrift pattern around a small hill in Adventdalen. The model was setup with one wind direction and with a Computational Fluid Dynamics solver determining wind flow. The simulation aimed at a meter accuracy but failed in locating accurately the snow accumulation zone, possibly because Jeadicke's work was based on a single wind direction. However the erosion zones were successfully determined.

Nevertheless, no statistical analysis was carried out limiting any comparison with other models.

- In another study, Jeadicke (2001) tried to apply a snow drift model inspired from Liston and Sturm (1998) and Pomeroy et al. (1997) and a mesoscale wind simulator to predict snow accumulation at a 50m resolution in two different sites in Svalbard (Blekumbreen and Drønbreen). Jaedicke's model was applied on a 50m grid and failed in simulating reasonable snow distribution in both sites. It was argued that the assumption of snow drift profile equilibrium was the reason of the model deviance.

- Bruland et al. (2004) studied snow distribution in two areas of Svalbard and one of them, the DeGeer Valley is located 20km north-east of Longyearbyen. They used the physically based SnowTran-3D model from Liston and Sturm (1998) and a curvature-based wind field model forced with the data from the weather station located at the airport of Longyearbyen. The model was tested either at 50 and 100 meters resolution. The quality of the model was assessed by correlating the observed and modelled snow distribution probability functions, and by visually comparing erosion and deposition areas. Even though the model proved to predict a snow distribution functions highly correlated with the data, it did not predict properly snow distribution over complex terrain, where most of the variability occurs. This indicates that pointwise comparison of simulated and observed snow depth showed significant errors. The result were independent on the grid resolution, presumably due to the coarse wind field model used that did not furnish additional informations when increasing the grid resolution.

Thus it can be seen that physical models successfully modelled large scale snow distribution but have failed explaining small scale (less than 100m grid) wind-driven snow transport. However, statistical models and topographical parameters have been used to describe small scale snow distribution (down to 10m grid Winstral et al., 2013), resolution that is closer to describe the interaction between topography and snow distribution (Clark et al., 2011). Additionally such models have never been tested in Svalbard to our knowledge.

Therefore, this study aims at testing the topographical parameters developed by Winstral and Marks (2002) to distribute snow from point measurements by mean of regression tree using two spatial resolutions: 5 m and 50 m. The study is conducted in four sites (Breinosa, Larsbreen, Longyearbreen and a South Facing Slope in Adventdalen) located on Nordenskjoldland, central Spitsbergen, Svalbard, Norway. In each site, snow depth data was collected by manual probing or Ground Penetrating Radar and was used to calibrate and validate two models at both resolution. The 5m and 50m models are then compared in each site to assess whether this approach can accurately distribute snow at small scale. Transferability of each model is then tested by applying it to other sites. Also the model built in Longyearbreen is used to predict the total Snow Water Equivalent stored in the snow pack. Errors and limitations are discussed and special attention is given to how the modelling approach could benefit from a snow depth data acquired with UAV-borne photogrammetry.

2 Study Sites and Local Climate

2.1 Study Sites

The field campaign took place between the 22nd of March and the 12th of April 2015 and was conducted in Nordenskjoldland, the central part of Spitsbergen, the largest Island of the Svalbard archipelago. The study investigated four sites: Breinosa, Larsbreen, Longyearbreen and a South Facing Slope of Adventdalen, all located in the vicinity of Longyearbyen, the main settlement of the Archipelago. The characteristics of each site are presented in the following sections.

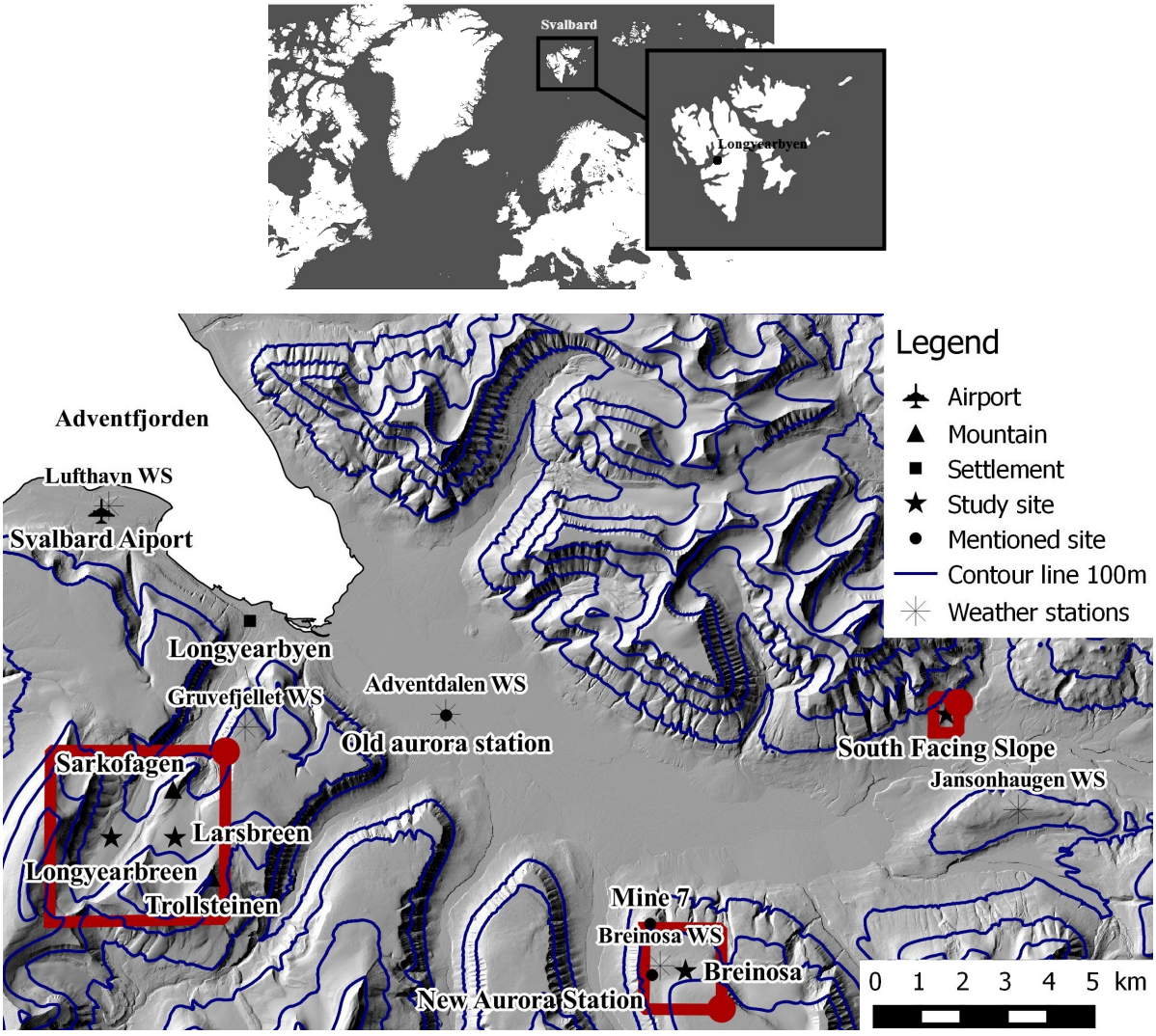

Figure 1: Map of the study areas. Zoomed view of the red framed areas are presented further.

2.1.1 Breinosa

The study area hereafter referred to as Breinosa is located 13km East of Longyearbyen (Figure 1) and on the NW side of the mountain of the same name. As displayed in Figure 2, it stretches on an area of 2km^2 with elevation ranging from 450 m.a.s.l. to 700 m.a.s.l. and globally facing NW. It is located 200m above Mine 7 and close by the New Aurora Station of UNIS. It rises southward in a homogeneous gentle slope (∼3°) until a short steeper slope (∼10°) leading to a

270m-wide plateau. Southward from the plateau rises a steep slope (∼15°) that is occupied by a small glacier. The topography then flattens on the uppermost part of the site.

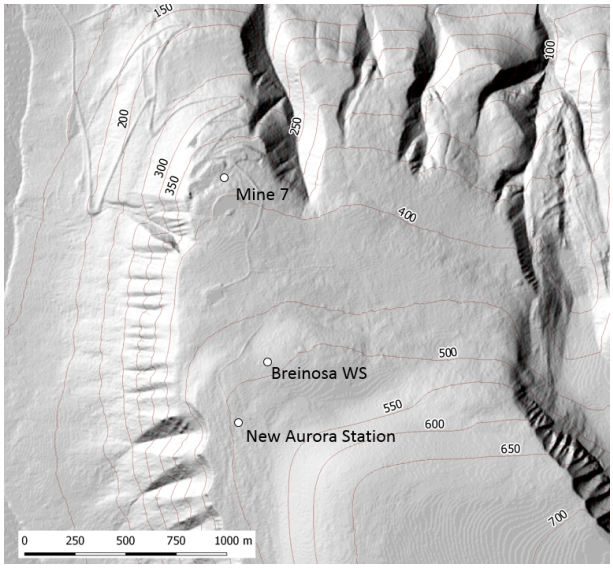

Figure 2: Map of the Breinosa area.

This area was expected to be exposed to wind coming from W, N and NE with the Breinosa mountain protecting from winds coming from S and SE. The road that is running from Longyearbyen to the border of the study site ensured an easy access to the site. A weather station, referred in this report as Breinosa WS is located in the vicinity of the study site as can be seen in Figure 2.

2.1.2 Larsbreen

Larsbreen is a glacier located 5km South of Longyearbyen (Figure 1) and the study area is located in its lower part, covering ∼0.6km². It spans from 300 m.a.s.l. to 550 m.a.s.l. with a steady slope of ∼6° facing NNE. Figure 3 show a close view of the site. The study also included the Sarkofagen ridge North-West of the glacier which consist of a 15° slope up to the 550m.a.s.l. Larsbreen can be considered as a well sheltered area from wind for every direction by the high

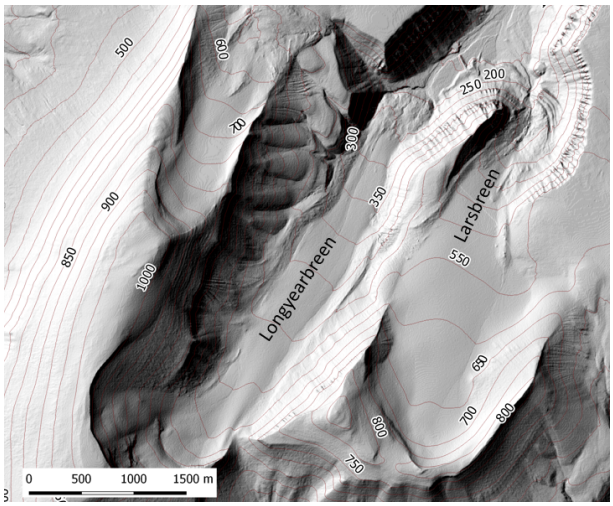

Figure 3: Map of Larsbreen and Longyearbreen areas.

ridge standing to the West, the cirque-shaped 800m high Trollstein mountain to the south and a 500m high plateau to the East. The presence of the glacier confirm the high snow accumulation rates in the area. In addition, its location close to Longyearbyen made it easy to access by ski. The closest weather station is Gruvefjellet 2.2km NNE.

2.1.3 Longyearbreen

The Longyearbreen glacier is located just 1km West of Larsbreen (Figure 1). Located 200 to 650 m.a.s.l. its surface has a gentle slope (∼3°) facing NE and is surrounded by high ridges rising up to 1000 m.a.s.l. on all sides as can be seen in Figure 3. The entire glacier which covers an area of ∼1.6km² has been covered by this study.

Longyearbreen, in the same way as Larsbreen, is well protected from the wind and is expected to receive significant amounts of snow from precipitation and/or blown snow. Moreover, the site was particularly easy to access on snowmobile. The closest weather station is Gruvefjellet WS located 4km NE (Figure 1).

2.1.4 South Facing Slope (SFS)

This small site spreads over ∼0.7 km^2 and is located 16km West of Longyearbyen (Figure 1). It is hereafter referred to as SFS. As it can be seen in Figure 4, it consists of a S-SSW facing slope spanning form 100 to 150 m.a.s.l. with an average slope of ∼4°.

Opening to Adventdalen to the South, this slope was thought to be relatively exposed to the main wind blowing along the valley. Some features were nevertheless offering wind-sheltered areas where snow drift was expected. The site was located nearby the main snowmobile track going through Adventdalen. The closest weather station was located on Jansonhaugen 3km south.

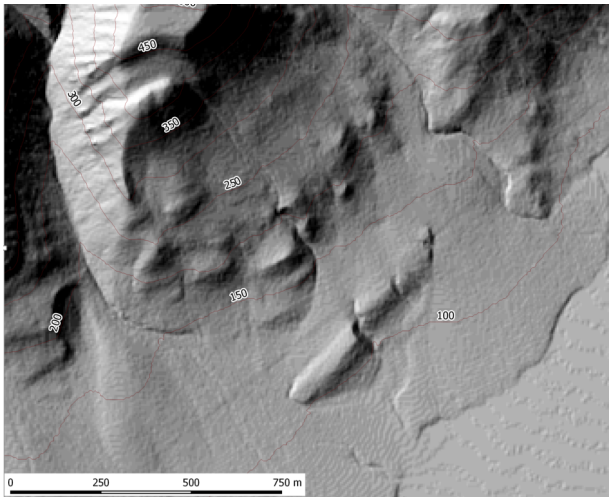

Figure 4: Map of the South Facing Slope area.

2.2 Local Climate

The climate of the Svalbard Archipelago is dominated by its high latitude and its location in the middle of the Greenland Sea. Here, the Siberian anticyclone from South-East determines cold and dry weather characterized by strong winds. Occasionally, humid and mild airflow coming from the South located Atlantic Ocean provides heavy precipitation and mid-winter snow melt

(Humlum et al., 2003). Exposed to this confluence, the Svalbard climate varies significantly at a local scale.

The climate in the Longyearbyen area has been characterized as "High Arctic maritime snow climate" Eckerstorfer and Christiansen (2011). The winter is 9-10 months long, characterized by an annual mean temperature of -3.8°C. Although Longyearbyen is located in one of the driest zones of the archipelago (Eckerstorfer and Christiansen, 2011), its coastal location guarantees a more humid weather than surrounding inland areas (Humlum, 2002). The annual precipitation recorded at the sea level (Longyearbyen airport) is 200 mm. However, due to wind-driven gauge under catch, a 100% correction factor should be applied to that value (Humlum, 2002). The snow pack is thin and cold, covering the land 8 to 10 months per year (Eckerstorfer and Christiansen, 2011). Due to the strong winds, the snow is unevenly distributed and wind exposed sites are often snow free.

3 Materials and Methods

In the present study, snow depth distribution is modelled using regression trees. This statistical approach investigates the relationships between snow depth data and a set of predictors assumed to control the distribution of snow depth. Unlike physically based models, statistical models do not simulate any physical process between predictors and response, but rather find statistically significant interactions between them. Since topography has a strong influence on both wind fields and snow distribution the following terrain-based variables are regularly given as predictors of snow depth and were therefore included in the present study (Winstral et al., 2002, 2013; Elder et al., 1995, 1998; Balk and Elder, 2000; Molotch et al., 2005): elevation, slope, wind exposure indexes (Sx and Sb) and a radiation index that accounts for heterogeneous solar radiation input to the surface. s a statistical model, regression trees require snow depth data from the site of interest in order to predict snow depth in areas that were not surveyed. The outline of the study is presented in Figure 5

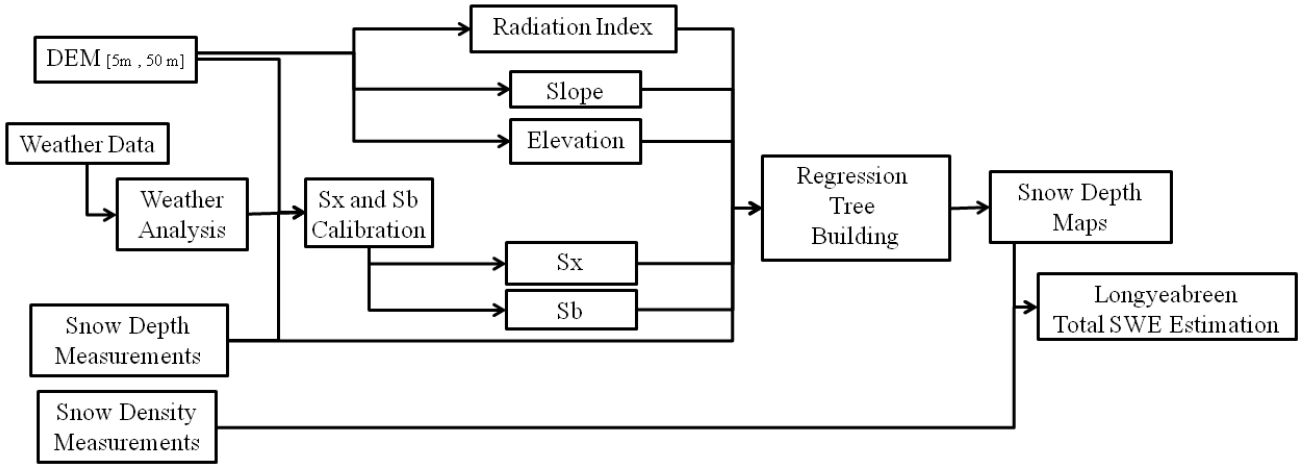

Figure 5: Outline of the regression tree modeling framework and how it can be applied to the estimation of the total SWE storage on Longyearbreen glacier.

In the following sections it is first described the fieldwork that was conducted to measure snow depth and snow density in the four study sites. Then each predictor, its expected influence on snow depth and its calculation method is explained. Eventually, the principle of regression tree as well as the way it was used are presented. Some concepts require a specific theoretical background but given that the theory is highly integrated with the method it was chosen to include it in the present methodology part.

3.1 Snow Depth and Snow Density Measurements

In all four study sites, snow depth was surveyed in order to calibrate and validate the snow distribution model. The measurement of snow density in Longyearbreen was necessary to convert

the snow depth map given by the model into total water content of the snow pack.

3.1.1 Snow Depth

Snow depth data was acquired using manual probing in Breinosa and Larsbreen, while in Longyearbreen and SFS Ground Penetrating Radar (GPR) was used.

Manual Probing The measurements were conducted using a 3m long avalanche probe graduated every centimetre. To anticipate the referencing of the results on a 5m grid, measurements were taken 5 to 10m from each other. At each measurement spot, a set of 2 to 4 additional measurements, randomly located within a 3m wide area around the measurement point to document the within cell variability. The probing track was determined to survey areas with very different topographical settings and wind exposure situations and to respect safety recommendations. Every measurement was geo-localised by a handheld Global Positioning System (GPS) with 5m accuracy.

Figure 6: Manual probing in Breinosa.

Ground Penetrating Radar The Ground Penetrating Radar (GPR) is a well established method to measure snow distribution over wide areas and have been used extensively in Svalbard (Jaedicke and Sandvik, 2001; Eckerstorfer and Christiansen, 2011; Bruland et al., 2001). The GPR used in this study was composed of a Malå ProEx control unit, a 800MHz unshielded antenna mounted on a sledge and a Malå XV monitor. The sledge was pulled by a snow scooter on which an operator was controlling and checking the GPR measurements via the monitor. A handheld GPS was linked to the control unit to locate every measurement with a 5 to 10m accuracy.

The principle of the GPR is displayed in Figure 7 and is based on the properties of propagation of electromagnetic waves in heterogeneous media (Neal, 2004). The antenna of the GPR is composed of a transmitter (or transmitting antenna) and a receiver (receiving antenna). The transmitter emits electromagnetic waves to the medium (snow in this case) and when the waves reach a medium with different electromagnetic properties (also called reflector, ie. rock or ice), part of the waves is reflected back to the receiver and the 2-way travel time of each wave is recorded by the control unit (Figure 7).

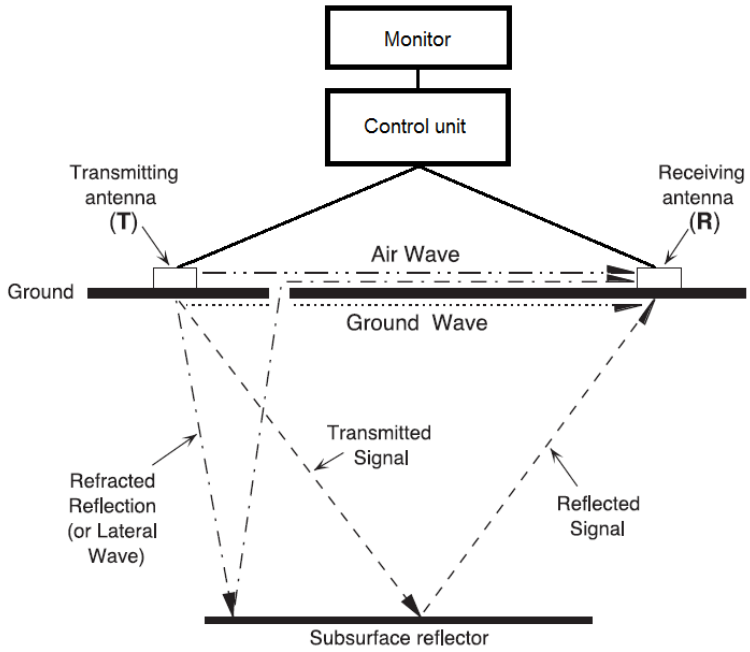

Figure 7: Schematic view of the GPR. Electromagnetic waves are emitted by the transmitter, travelling through the media, reflected by the reflector and received by the receiver. Modified from Neal (2004).

The monitor converts the 2-way travel time into depth using a user-define wave propagation velocity. For dry snow, the propagation velocity of electromagnetic waves can be simplified as a function of density (Ulaby et al., 1986). Assuming density constant throughout the thickness of the snowpack (Bruland et al., 2001), the appropriate propagation velocity was found empirically by comparing manual probing with the recorded 2-way travel time using the empirical equation developed by Ulaby et al. (1986) for dry snow below freezing temperature:

$$v = \frac{t}{2d} = \frac{c}{\sqrt{(1 + 0.51\rho)^3}} \tag{1}$$

Where d is the depth, t the 2-way travel time and v the propagation velocity of the signal, c is the speed of light and ρ is the snow density. At the beginning of the survey, agreement between manual probing and GPR measurement was found for a velocity of 0.230 m/ns. Using Equation 1 it leads to the realistic value of 380 g/cm^3 for the snow density. Comparison between probing and GPR snow depth was carried out at the beginning and at the end of each transect to make sure that density remained constant during the whole survey.

The choice of the frequency of signal is a compromise between resolution (high at higher frequency) and penetration depth (large at lower frequency) (Neal, 2004). According to Annan et al. (1995) the resolution of GPR measurements is equal to a third of the wavelength λ of the signal which can be estimated by knowing propagation velocity v and frequency f:

$$precision = \frac{\lambda}{3} = \frac{v}{3f} \tag{2}$$

In the present study, a 800 MHz antenna was used leading to a precision of 9.5 cm given by Equation 2. The signal was emitted every 0.1 s. This allows, moving the antenna at a

speed of 10-20 km/h, to acquire 1 sample every 10-20 cm. The transects (paths followed by the snowmobile hauling the GPR) were planned before the beginning of the survey and were limited by the safety recommendations related to driving a snow mobile in complex terrain.

The processing of the GPR data is made using Reflex-W software. Due to the shallow snowpack, the raw signal was already very clear and did not need any correction except shifting the depth origin from the antenna's transmitter to the snow surface. The snow/ice or snow/rock boundary was then selected manually following the line where the reflected signal had the highest amplitude. Figure 9 shows an example of GPR transect.

Figure 8: GPR used in Longyearbreen and SFS. The sledge pulled by the snow scooter allows to cover large areas in a short time.

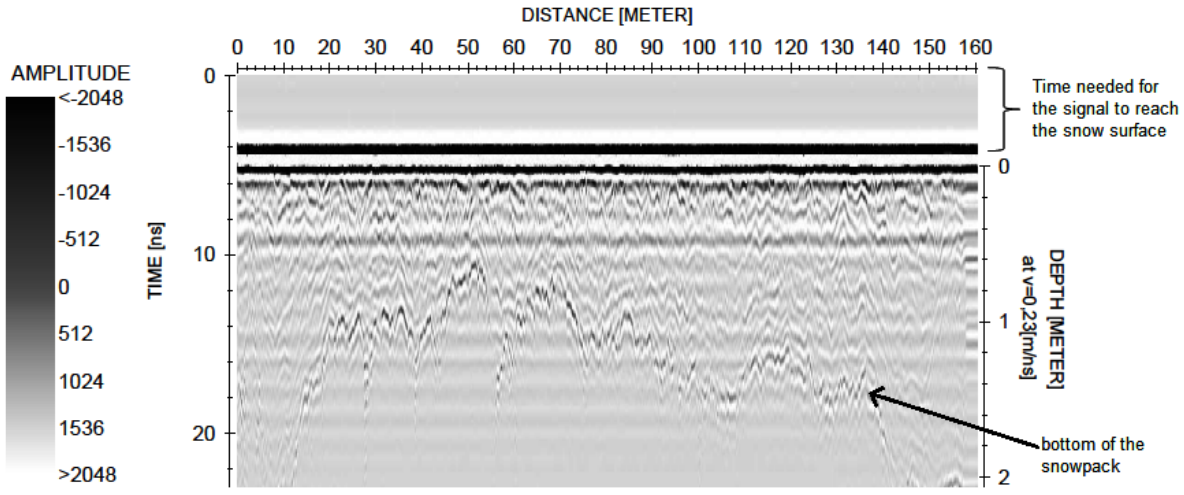

Figure 9: Example of GPR transect acquired during the snow depth survey of Longyearbreen.

GPR data quality is controlled by comparing measurements taken in intersecting transects. At the intersection the snow depth measurements are expected to match within a tolerance interval equal to two times the instrument resolution, i.e. 19 cm.

3.1.2 Snow Density

The main use of snow density data is to convert the snow depth prediction given by the snow distribution model into the total amount of water stored in the snow pack of Longyearbreen. As explained in the previous section, the calibration of the GPR is made by comparing manual probing and GPR snow depth readings and gives directly the average density of the snow pack with a precision of 6.3 kg/m^3 by combining Equation 2 and 1.

To complement these calculations snow density was also measured in six locations in Breinosa and in four locations on Larsbreen using snow sampler. It consists of an aluminium tube of volume $V_{tube} = 463cm^3$ which is fully inserted into the snow, dug out filled with snow and closed with two lids. The mass m_{tot} of the filled sampler is then measured on site using a spring balance with 10 g resolution. Knowing that the empty tube mass is $m_{tube} = 522g$, the sample density ρ_{snow} in kg/m^3 is calculated as follows:

$$\rho_{snow} = \frac{m_{tot} - m_{tube}}{V_{tube}} * 1000 \tag{3}$$

The results are then compared to the one of the GPR.

Figure 10: Snow density measurement in Breinosa.

3.2 Model Predictors

Statistical modelling approaches, such as regression tree, aim at finding a relationship between the dependant variable (here snow depth) and a set of predictors that are believed to control the behaviour of the dependant variable. The predictors that have been selected for the present study are elevation, slope, wind exposure indexes (Sx and Sb) and a radiation index. In this section, each predictor is introduced along with its calculation method and its effect on snow depth.

3.2.1 Elevation and Slope

Elevation and slope are indexes traditionally used in snow depth statistical modelling (Winstral and Marks (2002), Elder et al. (1998), Balk and Elder (2000), Molotch et al. (2005)). Elevation

is commonly associated with a positive gradient in snow depth due to orographic precipitation (Roe, 2005). Slope affects snow distribution in two ways. Very steep slopes will affect gravitational transport such as avalanches or snow creep and can lead to reduced snow depth. However, moderately steep slopes may determine a change in the wind flow, determining an enhanced snow deposition.

Elevation and slope are obtained by analysing the Digital Elevation Model (DEM) of the area of interest. A DEM is a geo-localized grid, where each grid cell is identified by three parameters: Northing, Easting and Elevation. The size of the cells is called grid resolution and determines the minimum size of a reproducible element by the DEM. Higher resolution DEMs can model complex terrain more accurately.

The Norwegian Polar Institute provides freely available DEMs covering the entire Svalbard archipelago (npi, 2014). The DEMs were obtained from aerial stereo-images and have a spatial resolution of either 50 m or 5 m. In the present study the topographic analysis is performed using both topographic resolutions, in order to compare the modelling results and assess the model sensitivity to the spatial resolution of the snow predictors. Elevation and slopes where calculated over the 5m and 50m DEM using the free GIS software QGIS.

3.2.2 Wind Exposure Indexes: Sx and Sb

The wind exposure indexes Sx and Sb are based on terrain analysis, as done in Winstral et al. (2002). Sx, also called maximum upwind slope, aims at delineating sheltered and exposed area given a specific wind direction (Figure 11). Sb, also called slope break, further analyses the upwind slope to spot features that would generate turbulent wind and enhance snow deposition (Figure 12). Sx and Sb are calculated according to a constant wind direction model and over the DEM.

First, the method used to analyse weather data and to determine the important wind directions used for the indexes calculation is presented. Then, the calculation and calibration procedures for Sx and Sb are presented.

Weather Data Analysis Since wind has a significant influence on snow distribution, the wind direction from which snow transport is expected needs to be determined prior calculation of the wind exposure indexes. The weather stations of Gruvefjellet, Breinosa, Lufthavn and Jansonhaugen were used to evaluate the dominant wind direction in terms of frequency and speed. Lufthavn WS is taken as a reference for the precipitation since it was the only weather station recording that parameter. Weather records from the 1^{st} of September 2014 to the 1^{st} of April 2015 are analysed.

Two wind directions are generally of great interest for studying snow drift:

- Firstly the wind that will be strong enough to generate snow drift, i.e. that will be able to extract the snow grains from the snow surface and to carry them away. A wind rose presenting both wind speed and wind direction is thus analysed to determine this wind direction.

- Secondly wind direction that brings most precipitation. Indeed, important part of the snow distribution is made during precipitation events (preferential deposition Lehning et al., 2006). Wind direction along with precipitation and other climate variables were plotted for the analysed period. The dominant wind direction during precipitation event was then determined.

Up-wind Slope: Sx Based on the two wind directions that were determined by weather data analysis, the upwind slope Sx can be defined for each grid cell as the maximum slope that can be encountered among the upwind cells within a certain distance d_{max} from the cell of interest (Figure 11). It is a basic indicator of sheltering or exposure of a cell from a specified wind direction.

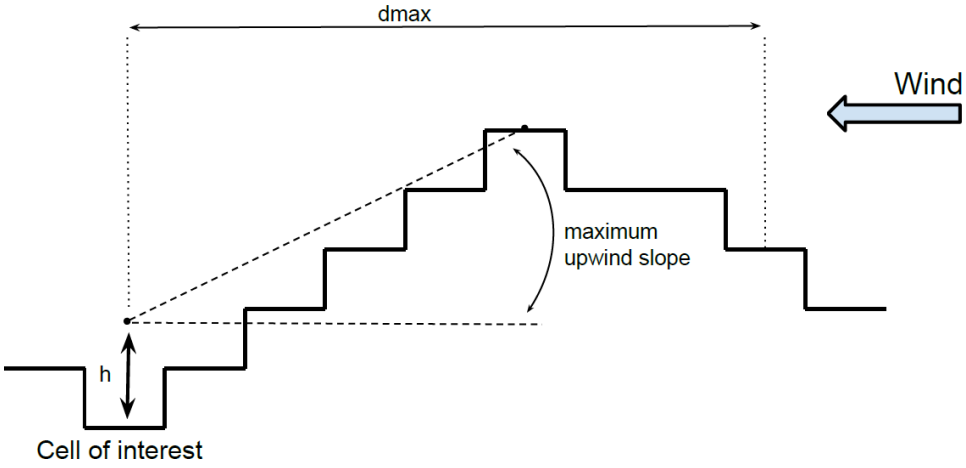

Figure 11: Schematic view of the up-wind slope Sx. From the cell of interest, the upwind cells of the DEM are investigated until a defined distance d_{max} to find the cell that has the greatest slope.

It can be calculated as follows (Winstral and Marks, 2002):

$$Sx_{A,h,d_{max}}(x_i, y_i) = \max_{0 \leq v \leq dmax} \left[tan\left(\frac{z_v - (z_i + h)}{\sqrt{(x_v - x_i)^2 + (y_v - y_i)^2}} \right) \right] \tag{4}$$

where :

- x, y and z are respectively easting, northing and elevation of the cell;
- i is the index of the investigated cell;
- v is the index of a cell located upwind of the investigated cell (in direction A) and at a maximum distance of d_{max};
- h is the user-defined instrument height to be added to the elevation of cell of interest z_i.

Equation 4 evaluates the extent of wind-sheltering effect of the up-wind terrain on the cell of interest. d_{max} defines the maximum upwind search distance, physically indicating the reach of terrain influence on the snow redistribution as visible in Figure 11. The instrument height h, introduced by Winstral et al. (2013) represents an additional height given artificially to the cell of interest as shown in Figure 11. With small instrument height, small surrounding terrain features will appear bigger to the cell of interest while remote terrain perturbation will have less influence due to their small optical size. Increasing the instrument height thus allows to give less importance to surrounding terrain and more to the remote topography.

In order to account for the wind variability, Sx values are calculated every 5° in a 40° wide wind window centered on the prevailing wind direction and $\overline{Sx}$ is then calculated as the average of these different Sx:

$$\overline{Sx}_{A,h,d_{max}}(x_i, y_i) = \frac{1}{n_v} \sum_{A_i = A_1}^{A_2} Sx_{A_i,h,d_{max}}(x_i, y_i) \tag{5}$$

Where A_1 and A_2 are the wind directions bounding the 40° wide wind window centered on the direction A. A_i take values within this wind window with 5° increment.
d_{max} and h are site specific and need to be determined empirically. The calibration of $\overline{Sx}$ refers to Winstral et al. (2002). A series of $\overline{Sx}$ maps is generated with $d_{max} = [20, 50, 100, 150, 200, 300, 500]$ and $h = [0, 1, 2, 4, 5]$. For each $\overline{Sx}$ map the wind exposure values correspondent to the snow sample location are extracted and linear regression is built between snow depth and $\overline{Sx}$ values. The best d_{max} and h values are the ones that give the best linear fit between calculated $\overline{Sx}$ and measured snow depth.

Linear modelling is ruled by a set of assumptions: residuals are to be normally distributed around zero, independent from each other. Therefore the residuals of each model are investigated to make sure that these assumptions are respected (assumptions and diagnostic plots are explained in Appendix C). Violation of these assumptions can bias estimation regression coefficients and error (Dormann et al., 2007). Transforming the data in a reversible way to comply with these assumptions is a common procedure in linear modelling. In the present study, two linear regression types are applied. Standard linear regression models snow depth as a linear function of $\overline{Sx}$. Guided by the analysis of the diagnostic plots a logarithmic transform of the response is also applied. This method models $log(SnowDepth)$ as a linear function of $\overline{Sx}$. The diagnostic plots in Appendix C were then used to determine which regression was the most reliable and could be used to calibrate $\overline{Sx}$. Spatial autocorrelation as explained is Appendix A was also investigated.

The removal of outliers (point that are showing a non-linear behaviour or that have too great impact on the model) is also recommended to improve the reliability of the linear regression. The study of diagnostic plots (Appendix C) is also used to spot single points that would have a too great effect on the model. These points are then removed from the model. In the present case, snow depth cannot take values lower than zero. For these areas, increased exposure (lower $\overline{Sx}$) will not have any effect on snow depth and this behaviour cannot be modelled by linear regression. Thus snow free area are ignored and regression is made only where sufficient snow pack existed.

Once the appropriate linear modelling approach selected, different models are built for various $\overline{Sx}$ (differing from one other by the d_{max} and h used for their calculation). The performance of each $\overline{Sx}$ as predictor of snow depth is then assessed by calculating the Mean Squared Error (MSE), as defined in Appendix A, of each model. The $\overline{Sx}$ map and related d_{max} and h that gave the model with lowest MSE is considered as the best predictor of snow depth. When no regression is found it is assumed that $\overline{Sx}$ is not a satisfying predictor of snow depth for that wind direction and for that site.

Slope Break Indicator: Sb A second predictor, Sb, is computed to take into account another characteristic of drifting snow. Sb aims at delineating drift zones generated by slope breaks. In other words it delineates changes in the upwind slope that generate turbulent and slower wind flow enhancing snow deposition (Figure 12).

It is obtained by calculating the difference between the maximum upwind slopes of surrounding and outlying topography:

$$Sb_{A,sepdist}(x_i, y_i) = Sx_1 - Sx_0 \tag{6}$$

where:

- Sx_1 is the maximal upwind slope of the surrounding terrain. It is calculated at the point of interest for a specific wind direction A, with no additional height ($h = 0$) and for $d_{max} = sepdist$. $sepdist$ is a site specific parameter and, as it can be seen in Figure 12, defines the extent of the turbulence area (ie. drift area) downwind of a slope break.

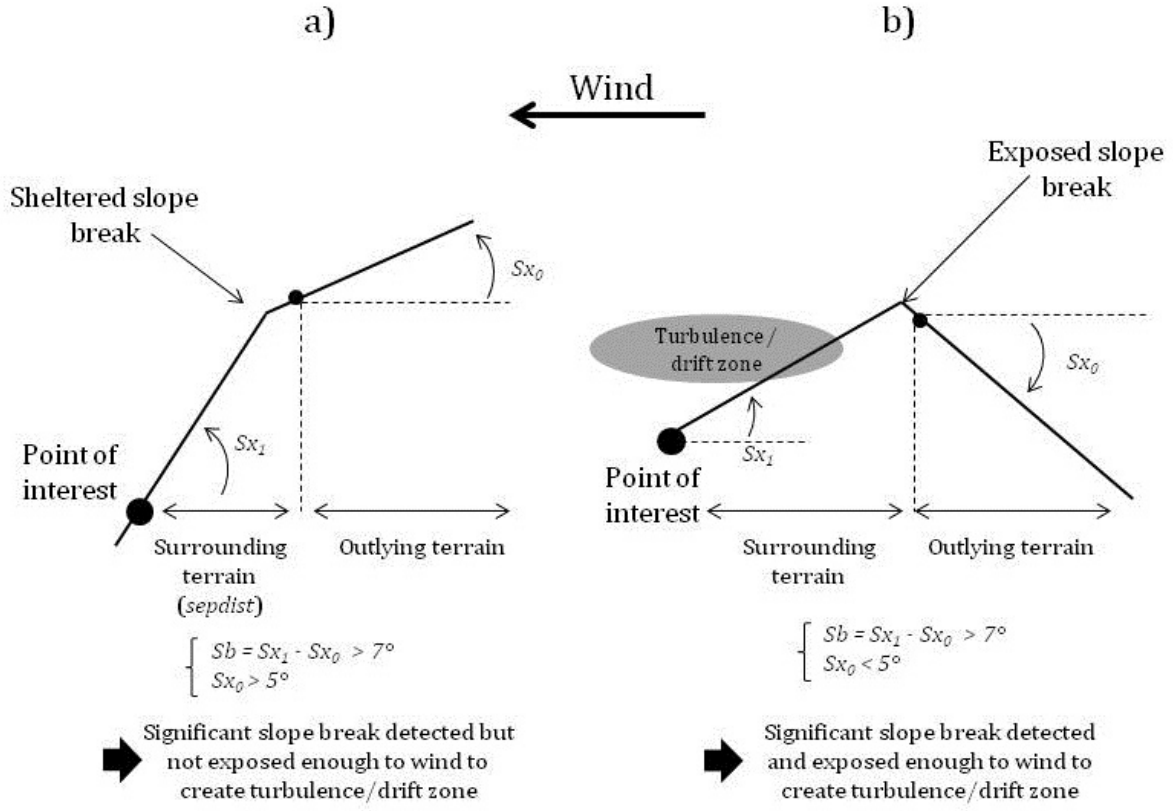

Figure 12: Sketch explaining the working principle of Sb. In order to have flow separation, wind speed reduction and snow accumulation it is needed to have sufficient slope break (Sb high enough) and that this slope break is located in an exposed area. In situation a) and b) the point of interest is sheltered from the wind ($Sx_1 > 0$) and are located downwind of a slope break ($Sb > 0$). But in a) the outlying terrain is already sheltered meaning that snow drift area might be located further upwind while in b) $Sx_0 < 5$ indicates that the slope break will receive enough wind to create a turbulence zone where enhance snow accumulation occurs.

- Sx_0 is the maximal upwind slope of the outlying terrain. As shown in Figure 12, it is calculated at the point located *sepdist* meters upwind of the point of interest (limit between surrounding/outlying terrain) and for the same wind direction A. A *dmax* of 1000m is used in order to encompass as much as possible of the outlying terrain. No additional height was used for Sx_0.

Sb are calculated every 5° in a 40° wind window around a prevailing wind direction. Then these Sb are averaged to give $\overline{Sb}$:

$$\overline{Sb_{A,sepdist}}(x_i, y_i) = \frac{1}{n} \sum_{A_i=A_1}^{A_2} Sb_{A_i,sepdist}(x_i, y_i) \tag{7}$$

Where A_1 and A_2 are the wind directions bounding the 40° wide wind window centered on the direction A A_i.A_i take values within this wind window with 5° increment.
As exposed in Figure 12, it is important not only to know where a slope break is located but also whether the wind hitting the slope break is sufficient to create turbulence. Indeed, if the upwind face of a slope break is already located in a sheltered area, the wind that hit the slope break will have been previously slowed down and will not cause significant additional snow

deposition (Figure 12, left). Therefore, two criteria are used to determine whether drift occurs: first, the slope break should be important enough meaning that $\overline{Sb}$ should be greater than a certain threshold. Second, the slope break itself should be exposed enough to wind so that wind speed reduction occurs meaning that Sx_0, the exposure index of the slope break itself, should be lower than a certain value. A binary map D is then computed with $D = 1$ where the two criteria are satisfied and $D = 0$ elsewhere.

Still *sepdist*, the thresholds in $\overline{Sb}$ and in Sx_0 need to be determined. Winstral et al. (2002) compared maps of D calculated for different *sepdist* values to a time series of aerial photographies during the melting season. Areas with persistent snow were assumed to be drift area and, once outlined, used to choose the best *sepdist*. For Winstral, threshold values were assumed equal to 7° for Sb and 5° for Sx_0 and justified by empirical aerodynamic considerations and validated by the aerial photographies.

Since no aerial picture was available for Svalbard, the *sepdist* values and threshold in $\overline{Sb}$ used by Winstral et al. (2002) could not be used directly. It is however expected that samples satisfying drift criteria (positive $\overline{Sb}$ and $Sx_0 < 5$) would show systematically higher snow depth as they are potentially located in a drift zone, ie. downwind of an exposed slope break. Scatter plots of snow depth versus $\overline{Sb}$ and Sx_0 were thus visually inspected for different *sepdist* in order to see if clusters of higher snow depth could indicate the presence of drift areas.

3.2.3 Radiation Index

The radiation index describes the relative distribution of solar radiation input over a complex topography. It is usually considered as a predictor of snow depth as it has great influence on the energy balance of the snow pack and therefore on melting events and metamorphic processes (Winstral et al., 2002; Molotch et al., 2005). It was calculated over the 5m and 50m DEMs using the Image Processing Workbench software of Frew (1990).

The solar radiation input was calculated over the DEM following the workflow presented in Figure 13 each first day of the month and every two hours from 00:00 to 22:00, for a period spanning from September to March 2014. This is done to account for polar night (no radiation input), and changing sun angle during the spring. First sun position, the part of the sky and of the surrounding terrain that are viewed by each cell, slopes and shaded areas are calculated using basic functions of Frew (1990). Then the intensity (in W/m^2) of direct and diffuse solar radiation received by each cell was calculated for clear sky and constant atmospheric conditions (Dozier, 1980; Frew, 1990). Eventually, the *TOPORAD* model from Dozier (1980); Dozier et al. (1981); Dozier and Frew (1990) corrected the radiation input by accounting for the radiation reflected by facing slopes. The radiation input maps were averaged over the whole period and scaled from 0 (areas less exposed to solar radiation) to 100 (areas most exposed to solar radiation).

3.3 Snow Distribution Modelling

The snow distribution modelling is done by means of regression trees. In the following section it would be given a general background on this statistical tool, with a focus on the best tree selection process. Also, practical applications of the model will be presented.

3.3.1 Theory of the Regression Trees

The regression trees are statistical models introduced by Wadsworth (1984) and widely used in statistics, data mining and machine learning. They aim at predicting a dependant variable (here snow depth) according to a set of predictors (here elevation, slope, Sx, Sb and the radiation index). It uses calibration (or training) data to analyse how the values of the predictors are

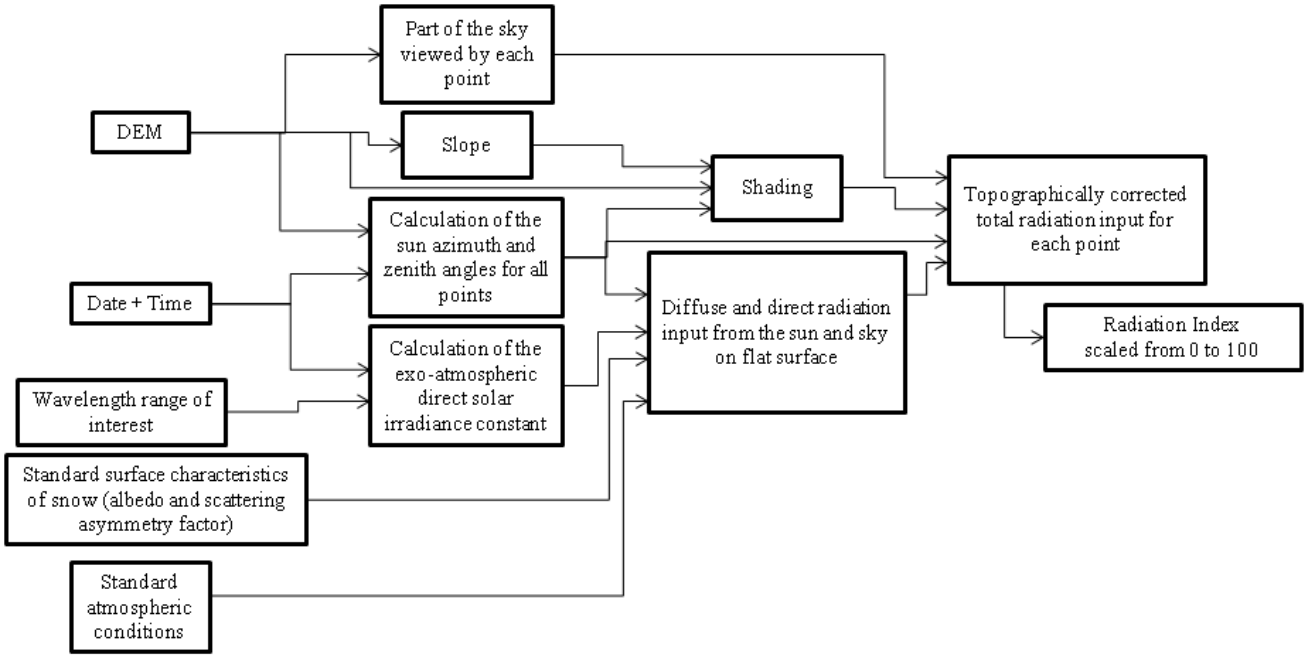

Figure 13: Schematic view of the calculation of the topographical index.

related to different ranges, or classes, of the dependant variable. The regression tree has the advantages of accounting for interaction between predictors and being an accessible non linear model. Indeed, this tool is able to find non-linear correlations within a large dataset of predictors-dependent variable, whatever could be the underlying physical law. However, its main limitation is given by the fact that the model is built on the data and therefore generally poor in generalizing the results on different datasets. In this study, the *rpart* algorithm (Therneau and Atkinson, 1997) from `R` statistical software was used. The algorithm, explained in Figure 14, can be summarized as follows.

Considering n observations of a dependant variable Y (i.e. snow depth) to which are related n observations of k predictors $X_{1..k}$ (i.e. elevation, slopes...etc.). For each predictor X_i, the algorithm will test all possible splits s that separate Y into two new subsets, also called leaves: Y_L, the samples for which $X_i < s$ and Y_R, the samples for which $X_i > s$. The Sum of Squares (SS) is used as a measure of within-class variability:

$$SS_C = \sum (Y_C - \overline{Y_C})^2 \tag{8}$$

where C is a given class, Y_C the samples of Y that are in C and $\overline{Y}$ their mean. Therefore, SS_L and SS_R are the variability of the data contained in classes L and R. SS_T being the Sum of Squares of the parent node, the reduction in Sum of Squares $SS_T - (SS_L + SS_R)$ is used as indicator of the performance of the split. Among all possible combinations, the split that gives the highest reduction in SS is made. The algorithm is called recursively in the two new classes. The algorithm stops when no split can reduce the SS significantly or when the existing classes do not contain enough samples to be split.

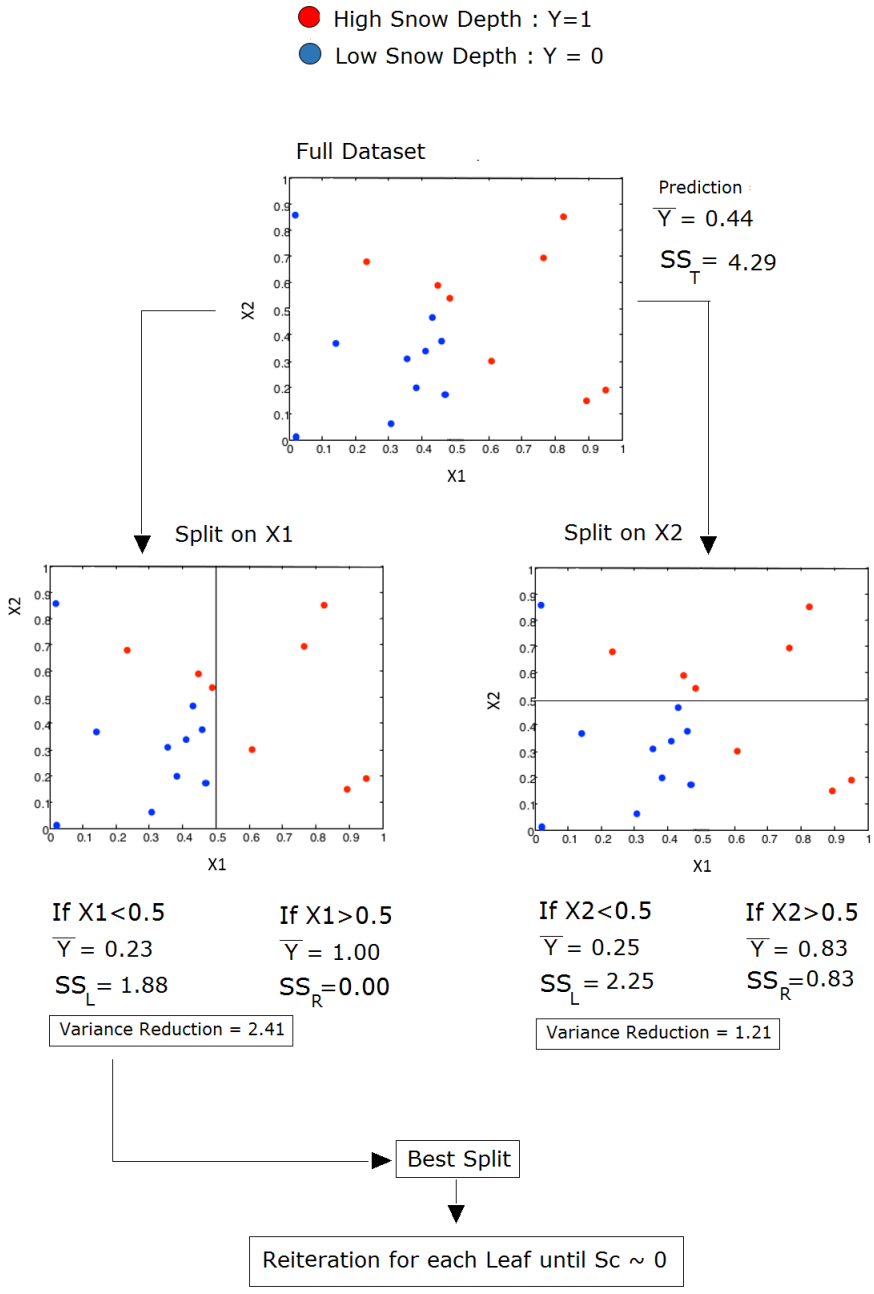

Figure 14: Example of regression tree algorithm working on two predictors, X1 and X2, of the dependent variable snow depth. Starting from a root, i.e. the full dataset, the algorithm estimates the first optimal split for each of the two predictors. In this case there are two possibilities : split on X1 or split on X2. Splitting the dataset creates two new subsets, also called leaves or snow classes. The mean value of a leaf is the prediction of the regression tree for the specific sequence of predictors' values that leads from the root to the leaf. In each snow class the variability of the data is evaluated according to equation 8. Eventually the total reduction in variability given by the split is evaluated and compared to the one achieved by splitting the root on a different predictor. The best split is the one that achieves the maximum reduction in variability, in this case the split on X1. The process is reiterated treating each leaf as a root until the total reduction in variance approaches the null value.

As an example a snow covered hill can be considered. If average snow depth on the wind-exposed site is lower than the depth on the wind-sheltered side, the regression tree will split the dataset in two snow depth classes, according to the wind exposures predictors. A snow class is the mean value of the snow depth data within a leaf and represents the output of the regression

tree. If wind does not play an important role but elevation gradient does, the dataset will be split according to elevation, attributing higher mean snow depth to the upper part of the hill and low snow depth to the lower part. This example can be extended to complex dataset, where participating predictors are many.

The quality of a tree can be assessed by two indicators. Firstly, the coefficient of determination R^2 (see Appendix A) that is the part of the dataset variance explained by the model and describes how well the tree is sorting the training data into consistent classes. Secondly, the cross-validation error assesses the capability of the tree to make predictions for values that have not been used to build the tree. The principle of cross validation is to leave aside a part of the dataset (called validation set) while building the tree and then to evaluate the error between the predicted values and observed values for the validation set. During a 10-fold cross validation, the dataset is divided into 10 subsets and cross validation is done 10 times taking each time a new subset as validation set. The trial that gave the lowest validation error is considered as the best tree and is called "cross validated tree" (Therneau and Atkinson, 1997).

Cross validation is also used to define the best tree size in order to avoid overfitting of the data. Overfitting means that, as the tree grows, it starts splitting consistent classes into insignificant sub-classes. It increases the overall R^2 but worsen its prediction capacity for new observations. Indeed the validation error first decrease with the first splits (better prediction capacity) but then increases again, indicating that the newly created classes are no longer improving the prediction capacity of the tree. This minimum in validation error determines the range of optimal tree sizes. The process of selecting the optimal tree size is called pruning. But since the partition used for cross validation is made randomly, some variation can appear from one cross validated tree to another depending on which data they have been grown on. To account for that, 100 cross validated trees were grown and their R^2 and cross validation error curves were plotted as a function of the number of splits to determine the optimal tree size Molotch et al. (2005). Once the optimal tree size is determined, different cross validated trees were grown, pruned to the right size and check manually for non-physicalities. Non-physical splits, ie. splits going against known physical relationships between the predictors and response, are related to minor inconsistencies in the dataset (such as unexpected low snow depth on sheltered area) and were therefore discarded.

The tree selection work flow can be summarized as follows:

- One hundred cross-validated trees are independently grown.
- The average R^2 and validation error of all trials are plotted as function of the tree size to find the optimal range of tree size.
- A new set of trees is grown and pruned to the best tree size.
- These trees are inspected one by one for non-physicalities.
- The best tree selected is the one that respect the physical meaning of the predictors and minimizes the validation error.

3.3.2 Snow Depth Mapping and Model Transferability Study

Following the procedure previously presented, regression trees are grown for each site. The snow depth maps are then computed for the 5m and 50m resolutions from the prediction that the regression tree assigns to each grid cell. The distribution and values of the residuals are also presented and discussed. Special interest is given to the differences between the two resolutions.

Each snow distribution model is then applied on the three other sites to assess the transferability of the model. The prediction accuracy of each model is assess in each site by calculating the R^2, the Mean Error and the prediction interval as defined in Appendix A.

3.3.3 Snow Water Equivalent (SWE) Storage in Longyearbreen Glacier

A practical application of the snow distribution model is presented. The regression tree modelling framework is used to estimate the total (SWE) stored in the snow cover of Longyearbreen glacier. This information is of prime importance for glaciologists and can put in regards to the recorded melt and thus estimate the mass balance of the glacier.

First the snow depth map and prediction interval is calculated as explained in the previous sections. Then the contour of the glacier was selected from the 5m DEM and a snow density was attribute to each grid cell according to the survey result. Eventually, the total SWE of the glacier is calculated as as the sum of each cell's SWE on the glacier surface:

$$TOT_{SWE} = \sum_{i \in Longyearbreen} y_i \rho_i c^2 \tag{9}$$

where y_i is the snow depth in meters, ρ_i is the snow density in kilograms per cubic meters, c is the cell size (5m or 50m depending on the DEM) and TOT_{SWE} is the total snow water equivalent on the glacier surface in cubic meters of water. Analogously, the 95% prediction interval of the prediction is evaluated as :

$$p.i._{SWE} = \pm \sum_{i \in Longyearbreen} p.i._{\cdot} \rho_i c^2 \tag{10}$$

This model is compared to two basic snow distribution models. The first one is the constant model that attributes to every cell of the area the mean observed snow depth. The second one is the elevation gradient model which derives from common knowledge (but not always true) that orographic precipitation controls the snow distribution in mountainous terrain. The elevation gradient model is built by linear regression of the snow depth samples versus their elevation for both the grid resolutions, therefore it takes the form:

$$y_{model} = \alpha z + y_0 \tag{11}$$

where α is the elevation gradient, while y_0 is the offset, i.e. the snow depth at zero meters level. The three models are then compared with specific interest for the precision of their estimation, i.e. their prediction interval.

4 Results and Discussion

In this section are presented the different results obtain, in a first time from the fieldwork and in a second time from the snow distributions models.

4.1 Snow Measurements

The data acquisition campaign conducted in Svalbard aimed at measuring snow depth in the four study sites. Snow density data was also collected for the SWE calculation in Longyearbreen.

4.1.1 Snow Depth

A total of 171 and 69 snow depth measurements were collected by manual probing respectively in Breinosa and Larsbreen. The GPR campaign brought 22 911 and 13 613 raw measurements respectively in Longyearbreen and on the South Facing Slope before averaging them over the DEMs.

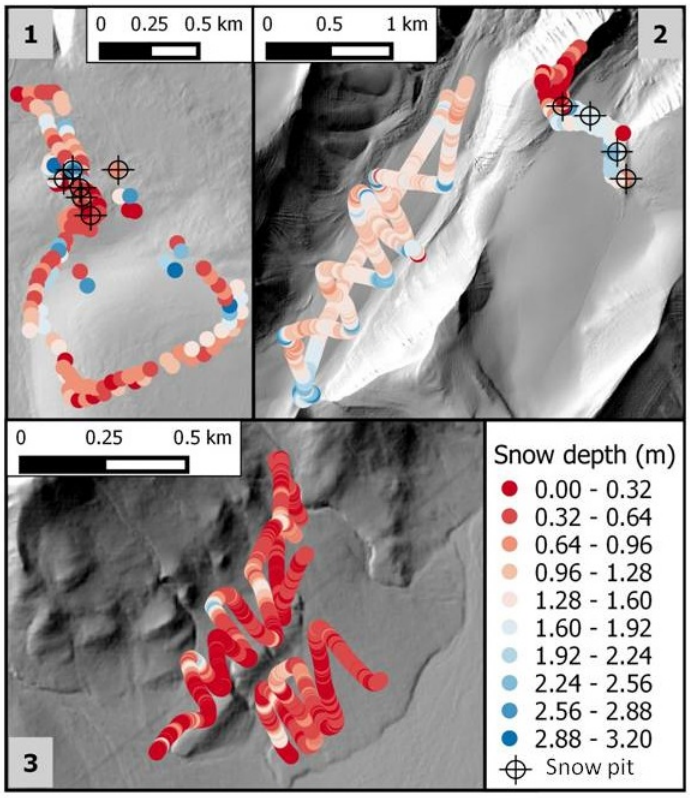

Figure 15: Snow depth measurements and snow pits in Breinosa (1), Larsbreen (2, right), Longyearbreen (2, left) and South Facing Slope (3)

The quality of the GPR data is assessed by comparing snow depth at the intersection of transects. For 10 intersections the average snow depth difference between transects is 8 cm, with a standard deviation of 5 cm and maximum difference of 17 cm. Therefore the GPR data are consistent (within the 19 cm tolerance interval given by the instrument precision) from one transect to the other.

The basic statistics of the data are summed up in Table 1 and the distribution of the snow depth measurements for each study site are displayed in Figure 15.

Table 1: Snow depth survey results

	Breinosa	**Larsbreen**	**Longyearbreen**	**SFS**
Number of raw measurements	171	69	23 061	13 613
For the 5 m DEM				
after average over grid cell	170	69	1737	898
Mean [m]	1.07	1.03	1.44	0.50
Standard deviation [m]	0.75	0.86	0.40	0.33
Within-cell Standard deviation [m]	0.09	0.10	–[a]	-[a]
For the 50 m DEM				
after average over grid cell	114	54	189	88
Mean [m]	1.01	1.13	1.42	0.50
Standard deviation [m]	0.65	0.82	0.36	0.28
Within-cell Standard deviation [m]	0.16	0.17	0.12	0.14

-[a]Below instrument resolution

As it can be seen from the Table 1 and Figure 15, the sites had very different snow distribution with a thin snowpack (0.3 m on average) in SFS while the other study sites offered snow-free ridges next to areas where snow cover reached 3 m. In Breinosa, the highest snow depth were found on North- an West-facing slopes (from 2 to 3 m) while flat areas had a much thinner snow pack (few centimetres). In Longyearbreen and Larsbreen the central area of the glaciers presented an homogeneous snow pack between 1 and 2 m thick. The North-West boundary of both glaciers showed reduced snow pack with even snow free areas while slopes located South-East of the glaciers presented deeper snow cover (up to 3 m).

4.1.2 Snow Density Measurements

The snow density on Longyearbreen was determined during the calibration of the GPR and lead to a estimated snow density of of 380 kg/m^3 with a uncertainty of $\pm$6.3 kg/m^3.

Additionally ten snow density measurements were taken in other sites: six in Breinosa and four in Larsbreen (Figure 15). Their mean and standard deviation values are reported in Table 2. It can be seen from Table 2 that the uncertainty of the density values in Breinosa and Larsbreen do not show any difference between the different sites. This result is in agreement with previous studies in the area, that confirms that the snow pack has low variability in the density (Eckerstorfer and Christiansen, 2011).

Table 2: Snow Density statistics

	Method	Snow Density ± Std. Dev.
Longyearbreen	GPR vs Manual Probing	$380 \pm 6.3[kg/m^3]$
Breinosa	6 snow pits	$375 \pm 24[kg/m^3]$
Larsbreen	4 snow pits	$348 \pm 53[kg/m^3]$

4.2 Weather Data Analysis

The analysis of weather data was conducted to determine first, the dominant wind direction during precipitation events, and second, the direction for which winds were strongest. These two wind directions were then used for the calculation of $\overline{Sx}$ and $\overline{Sb}$.

In Figure 16, the most relevant weather variables for the period spanning from September 1, 2014 to the April 1, 2015 are summarized. At Lufthavn WS the precipitation measured indicates a wet winter, with 244 mmSWE. Most of the precipitation occurred between September and end of December, while the polar night was drier. It can be observed that four major storms occurred, one in late September, two in November and the last one in April. Ranking the storms, the wettest storm (occurred in early November with 13 mmSWE/day) and the third and fourth came from South. Observing the temperatures plot, it can be noticed that also south coming storms determine an increase in temperatures, indicating that these events are determined by the North Atlantic weather system, in agreement with (Humlum et al., 2003). The second wetter storm (10 mmSWE/day) however came from East lasting six days and carrying low temperatures (-15 °C in Gruvenfjellet). This event is interpreted as a perturbation of extraordinary intensity coming from the Siberian area. Therefore it can be inferred from Figure 16 that the precipitation mostly come with southern winds.

The wind speed analysis shows that strongest and more frequent winds come from a wind window centred on the East, reaching 20 m/s (Figure17).

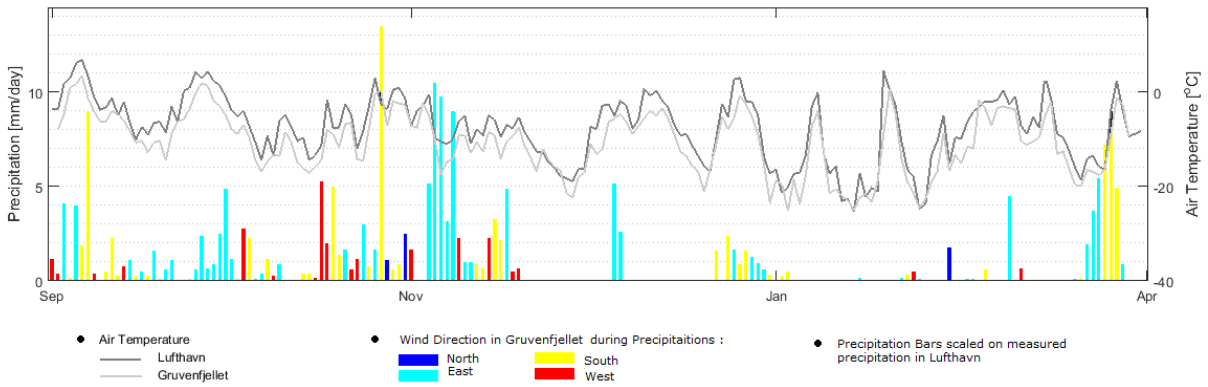

Figure 16: Summary of the weather data analysed from 1^{st} of September 2014 to the 1^{st} of April 2015. The histogram represents the precipitation measured in Lufthavn, while the bar color is given by the wind direction measured meanwhile in Gruvenfjellet. The grey-coloured plots show the air temperature behaviour. Combining these data it is possible to characterize storm events by means of prevailing wind direction and temperature.

The weather analysis suggests that the snow distribution is influenced by two wind directions, South and East. Therefore, the wind parameters $\overline{Sx}$ and $\overline{Sb}$ are evaluated in the two wind directions:

- The **precipitation** wind direction is a wind window of 40° centred on South. This wind

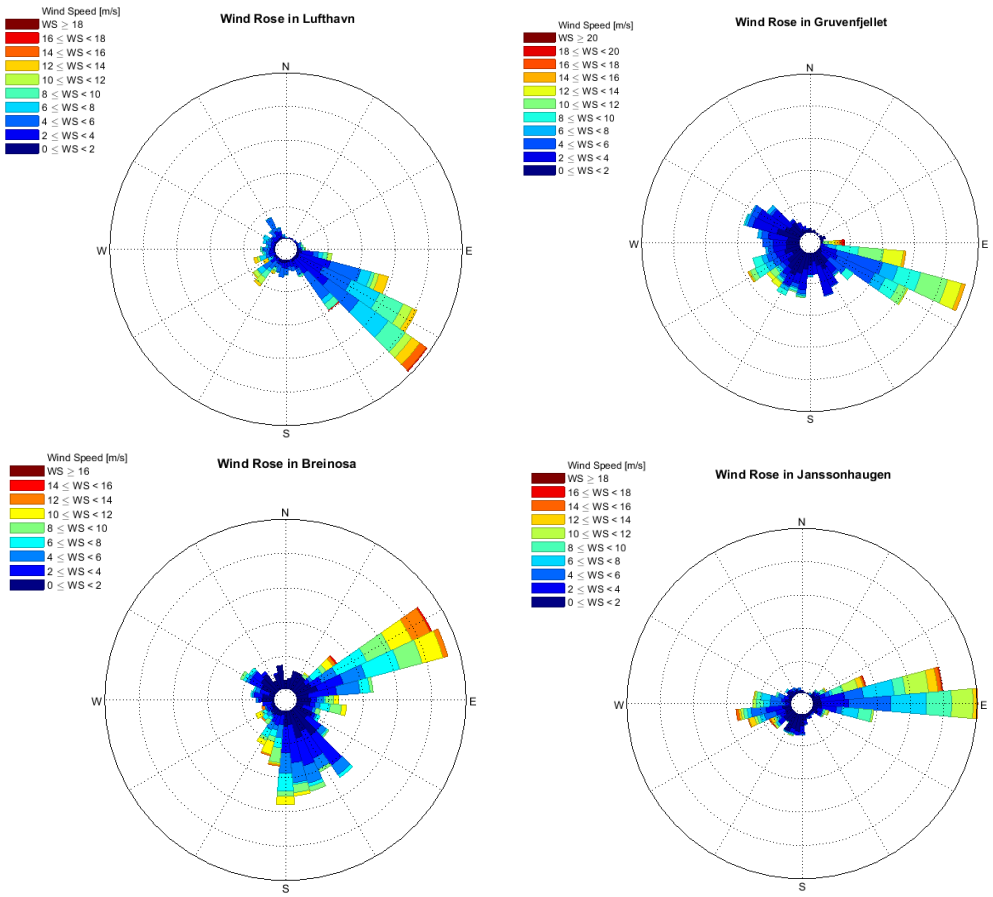

Figure 17: Wind roses in Lufthavn, Gruvenfjellet, Breinosa and Jansonhaugen. Each angular section represents a wind direction. The size of an angular section indicates the frequency at which wind direction is measured for that specific direction. Each angular section is divided according to the velocity that is measured while wind is coming from that direction. For each division, its color gives the wind velocity that was then recorded and its relative size represent the frequency at which that velocity was measured. It can be observed that the most frequent (large angular sections) and the highest wind speed (orange/red divisions) comes from a wind window centred on the East direction.

direction is expected to model the snow preferential distribution occurred during the three North-Atlantic storms.

- The **drift** wind direction is a wind window of 40° centred on East. This wind direction is expected do describe the snow redistribution due to the strong winds coming from East and the Siberian storm in November.

Key Findings

- Strong winds are identified as coming from East. They are expected to trigger snow drift. This wind direction is hereafter referred to as "drift wind direction".
- Winds carrying peak precipitation and storms are identified as coming from South. They are expected to control the distribution of snow during the storm by preferen-

tial deposition (Lehning et al., 2008). This wind direction is hereafter referred to as "precipitation wind direction"

- Since $\overline{Sx}$ is built on one prevailing wind direction, "$\overline{Sx}_{drift}$" refers to the $\overline{Sx}$ that was calculated using East as prevailing wind direction and "$\overline{Sx}_{precip}$" to the one that uses South as prevailing wind direction. They are used as distinct predictors. The same applies to "Sb_{drift}" and "Sb_{precip}".

4.3 Calculation of $\overline{Sx}$ and $\overline{Sb}$

Once that the drift and precipitation direction has been determined, the wind-exposure indexes $\overline{Sx}$ and $\overline{Sb}$ could be calibrated.

4.3.1 Calibration of $\overline{Sx}$

Diagnostic of the Linear Models As mentioned in the methods part, selection of the best h and d_{max} values for the calculation of $\overline{Sx}$ for the two wind directions was made by means of linear modelling. Analysis of the diagnostic plot for each model allow to select between standard linear modelling or with logarithmic transformation (Appendix C). The diagnostic plots are also used to detect and remove outliers. Moran's I is calculated (according to Appendix A) to determine to which extent residuals were spatially auto-correlated.

For Breinosa, Longyearbreen and SFS, log-transformation of the response and removal of some outliers increased the performance of the linear regressions. Only for Larsbreen the residuals showed very skewed behaviour. It can be explained by the type of data that has been collected in Larsbreen. A large number of samples were taken on Sarkofagen, the wind-exposed ridge on the right side of the glacier, where snow depth was small or equal to zero and since snow depth cannot go lower than zero after a certain threshold of exposure to the wind it can be expected that strong non-linearities can be found for these values. Nevertheless, even when removing these points from the dataset, there was not enough samples left to reach a satisfying linear models. Therefore it has been decided to discard the result given by the unreliable linear model in Larsbreen and to use the one given by the nearby and similar site of Longyearbreen. This is a way to estimate the extent of topography's influence on snow depth in Larsbreen but might not be the actual best d_{max} and h for that site. Thus the performance of $\overline{Sx}$ in Larsbreen could be increased if these best values were known. Spatial auto-correlation of the residuals is

a violation of the independence of the residuals in linear modelling. The Moran's I level and their respective p-values are displayed in Table 3. The p-values show that there is significant spatial auto-correlation of the residuals but the Moran's I value is still of the same level (or lower) than the one obtained by Winstral et al. (2002) which did not bring any correction to account for this phenomenon. Therefore the spatial auto-correlation of the residuals were not accounted for in this study. However, the authors recommend that for further calibration of $\overline{Sx}$ other regression models that account for spatial auto-correlation such as those reviewed by Dormann et al. (2007) should be used. The complexity of these models are often dissuasive but they are the only way to be in accordance with the principle of linear modelling.

Table 3: Spatial autocorrelation of the linear model residuals. Moran's I observed value should be as low as possible. Winstral et al. (2002) reported a value of 0.09 and did not correct it) and the p-value should be above 0.05 to discard spatial autocorrelation.

	Breinosa	Larsbreen	Longyearbreen	South Facing Slope
Drift direction:				
Moran's I	-[a]	0.12[b]	0.06	0.02
p-value	-[a]	0.00[b]	0.00	0.00
Precipitation direction:				
Moran's I	0.01	0.06[b]	0.09	0.01
p-value	0.05	0.01[b]	0.00	0.00

[a]No successful linear regression found.
[b]Values calculated from the optimal d_{max} and h values of Longyearbreen.

Influence of h and d_{max} on $\overline{Sx}$ For each site and for both resolutions, linear regression was conducted between snow depth and $\overline{Sx}$ built with different h and d_{max} when possible. Figures 18 and 19 display the MSE given by each regression as function of d_{max} and h values. From these curves, the effect of d_{max} and h on the performance of $\overline{Sx}$ can be interpreted with regards to the physical meaning of d_{max} and h. The values of h and d_{max} that gave the model with lowest MSE were considered optimal and reported in Table 4 and 5. The linear regressions built with optimal d_{max} and h and for the 5 m resolution are displayed in Figures 69 and 70 in Appendix C.3.

Table 4: Summary of the calibration result for $\overline{Sx}_{drift}$ and$\overline{Sx}_{precip}$ for the 5 m resolution. The α and β are the coefficients in the linear regression with logarithmic transformation of the response ($log(SD) = \alpha\overline{Sx} + \beta$) with $\overline{Sx}$ calculated for optimal h and d_{max}.

	Breinosa	Larsbreen	Longyearbreen	South Facing Slope
Drift direction:				
Optimal d_{max} [m]	-[a]	200[b]	200	200
Optimal h [m]	-[a]	1[b]	1	5
R^2	-[a]	0.01[b]	0.21	0.09
(α,β)	-[a]	(0.01, 0.29)[b]	(0.02, 0.33)	(0.08, -0.41)
Precipitation direction:				
Optimal d_{max} [m]	50	150[b]	150	200
Optimal h [m]	4	1[b]	1	5
R^2	0.25	0.52[b]	0.24	0.04
(α,β)	(0.04, -0.24)	(0.07, -0.14)[b]	(0.05, 0.10)	(0.06, -0.44)

[a]No successful linear regression found.
[b]Values calculated in Larsbreen from the optimal model of Longyearbreen.

For $\overline{Sx}$ calculated over the 5 m DEM: Satisfactory regressions between snow depth and $\overline{Sx}$ could be found in all cases except two: In Larsbreen as explained in the previous section, linear regression was not possible and optimal h and d_{max} from Longyearbreen were used. In Breinosa for the drift wind direction, no significant correlation could be found as shows the

$R^2 = 0$ in Figure 69 a). As a result it can be assumed that the $\overline{Sx}$ calculated for the drift wind direction is not a significant predictor of snow depth in Breinosa. Table 4 also shows that R^2 values are significantly higher for the precipitation wind direction. It indicates clearly that $\overline{Sx}$ calculated on the precipitation wind direction fits the data better than the one calculated on the drift wind direction. In other words, that the Southern winds are more important in the snow distribution processes than the Eastern winds.

When a good linear fit could be made, the effect of h and d_{max} could be assessed. As expected the influence of d_{max} and h depends greatly on the site. Indeed the extent of the influence of a terrain feature (d_{max}) can vary according to the complexity of the terrain while the way close or remote features are accounted for (h) depends on the site-specific terrain roughness.

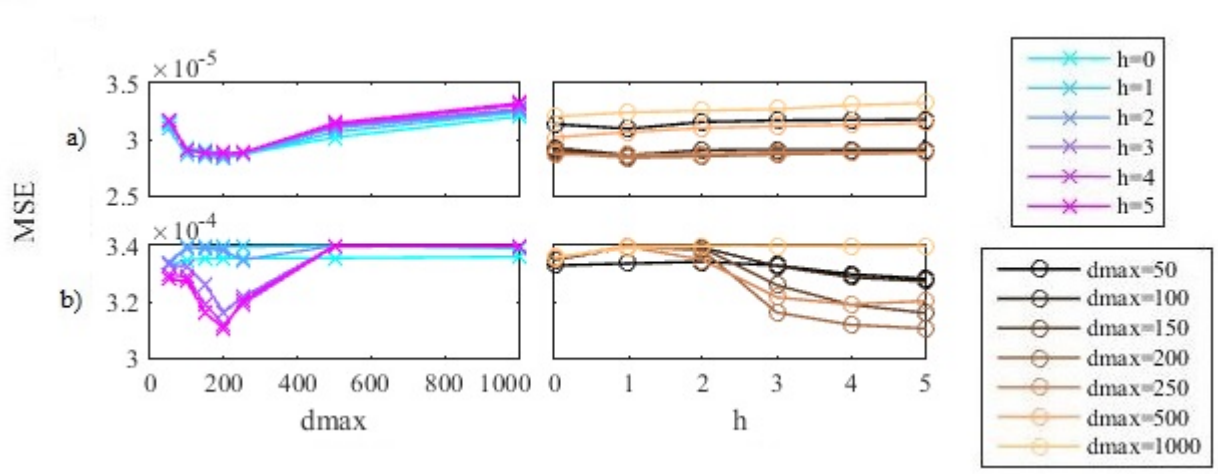

Figure 18: Calibration result of drift $\overline{Sx}$ for the 5 m resolution in a) Longyearbreen, b) SFS. The plot on the left shows MSE as function of d_{max} for different h values while the plot on the right shows MSE as function of h for different d_{max} values. The small values of MSE are due to the logarithmic transformation of snow depth.

For $\overline{Sx}_{drift}$:

As shown in Figure 18 (left), the MSE of the linear regressions in Longyearbreen and SFS is relatively high for low d_{max} values. It reaches minimum at d_{max}=200 m and increase again after that value. It means that $\overline{Sx}$ fits better to snow depth when "scanning" 200 m upwind. In other words, features that are controlling the wind-driven snow deposition are located between 150 and 200 m since $\overline{Sx}$ fits less to snow depth when scanning less or more than 200 m upwind. In Longyearbreen the value of h did not influence in a great extent the predicive capacity of $\overline{Sx}$. Since the instrument height h allows the $\overline{Sx}$ algorithm to "look over" close features and to give more importance to remote features, the smooth surface of the glacier does not need this adjustment. Thus an optimal value of $h = 1m$ was found. In SFS, however, the surface roughness is more important and the $\overline{Sx}$ was fitting better to snow depth when giving more importance to remote features. Thus an optimal value of $h = 5m$ was found.

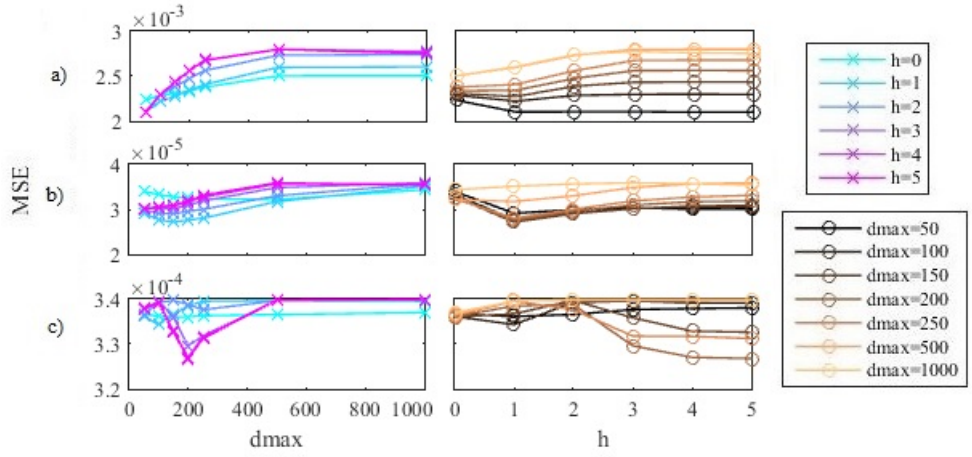

Figure 19: Calibration result of $\overline{Sx}_{precip}$ for the 5 m resolution in a) Breinosa, b) Longyearbreen and c) South Facing Slope. The plot on the left shows MSE as function of d_{max} for different h values while the plot on the right shows MSE as function of h for different d_{max} values. The small values of MSE are due to the logarithmic transformation of snow depth.

For the $\overline{Sx}_{precip}$:

The same analysis was made for Southern winds. Errors given by the linear regressions made between $\overline{Sx}_{precip}$ (calculated for different d_{max} and h) and snow depth are displayed in Figure 19. This time $\overline{Sx}$ appeared to be a good predictor of snow depth in Breinosa. The optimal value of $d_{max} = 50m$ indicates that in Breinosa, the snow distribution is controlled in each point by the topography located 0 to 50 m upwind. For Longyearbreen and SFS, the optimal values of d_{max} were found to be 150 m and 200 m respectively. Appropriate instrument height h was found to reduce the error in all three sites. Particularly in Longyearbreen and SFS, an obvious minimum can be seen in Figure 19 (right) for $h = 1m$ and $h = 5m$ respectively. In Breinosa, the effect of h was less pronounced but a minimal error was found for $h = 5m$.

For $\overline{Sx}$ calculated over the 50 m DEM: $\overline{Sx}$ calculated from the 50 m cell gave exactly the same results as the 5 m DEM. $\overline{Sx}_{drift}$ was not a good predictor of snow depth in Breinosa and Larsbreen data was not suitable for linear regression. Table 5 below gives the result of the calibration process for the 50 m DEM.

Table 5: Summary of the calibration result for $\overline{Sx}_{drift}$ and $\overline{Sx}_{precip}$ for the 50 m DEM. The α and β are the coefficients in the linear regression with logarithmic transformation of the response ($log(SD) = \alpha\overline{Sx} + \beta$) with $\overline{Sx}$ calculated for optimal h and d_{max}.

	Breinosa	Larsbreen	Longyearbreen	SFS
Drift direction:				
Optimal d_{max}	-[a]	200[b]	200	200
Optimal h	-[a]	1[b]	1	5
R^2	-[a]	0.01[b]	0.21	0.09
(α,β)	-[a]	(0.05, 0.41)[b]	(0.02, 0.36)	(0.03, -0.7)
Precipitation direction:				
Optimal d_{max}	50	150[b]	150	200
Optimal h	4	1[b]	1	5
R^2	0.25	0.52[b]	0.24	0.04
(α,β)	(0.04, -0.23)	(0.06, -0.2)[b]	(0.04, 0.09)	(0.03, -0.5)

[a]No successful linear regression found.
[b]Values calculated in Larsbreen use the optimal $\overline{Sx}$ of Longyearbreen.

4.3.2 Calibration of $\overline{Sb}$

Scatter plots of snow depth versus $\overline{Sb}$ and Sx_0 (not displayed) did not indicate any reasonable drift areas with higher snow depth in three sites out of four. Indeed, for the unsuccessful cases, the combination of the two following reasons prevented any use of $\overline{Sb}$ as a predictor of snow depth:

1) Samples satisfying drift criteria did not show higher snow depth meaning that $\overline{Sb}$ was not a significant predictor of snow depth. It would be the case in Breinosa for the drift wind direction where $\overline{Sx}$ was already proven as bad predictor of snow depth. Indeed since $\overline{Sb}$ and $\overline{Sx}$ are calculated in a similar way, it can be expected that $\overline{Sb}$ is not significant predictor when $\overline{Sx}$ also showed not to be good at predicting snow depth.

2) Few or no samples were satisfying drift criteria meaning that the potential drift areas were not surveyed or were absent from the site. In these cases, the significance of $\overline{Sb}$ remains unknown since the areas where its effect is visible were not sampled.

In Breinosa and for the precipitation wind direction only, samples with $\overline{Sb} > 6°$ and $Sx_0 < 5°$ showed significantly higher snow depth indicating drift areas (Figure 20). As a result, the drift map D, calculated from $\overline{Sb}$ and Sx_0 in Breinosa and for the precipitation wind direction was the only case where D could be used as a predictor predictor in Breinosa. This map of D of drift areas is shown in 21

The same calibration process is then applied to the 50 m DEM, obtaining similar results: the drift map D could only be used as a predictor in Breinosa and when calculated for the precipitation wind direction.

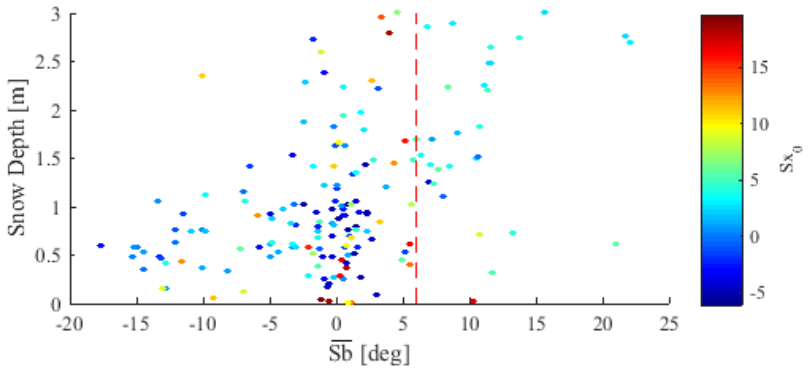

Figure 20: Scatter plot indicating snow depth versus $\overline{Sb}$. The scatter is graduated with Sx_0. Blue points that have also high $\overline{Sb}$ represent locations that are located in the influence zone of a slope break exposed to wind. They are therefore more likely to be subjected to enhanced snow accumulation.

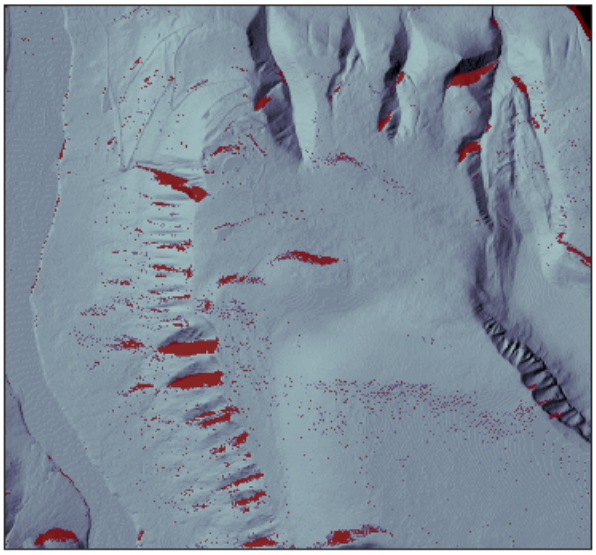

Figure 21: Valid drift areas map obtained by selecting the gridcells with $\overline{Sb} > 6°$ and $Sx_0 < 5^o$ in Breinosa.

Key Findings

- Calibration of $\overline{Sx}$ is done by linear regression between snow depth and $\overline{Sx}$ and optimal values for h and d_{max} are found for each site and for both resolutions (Tables 4 and 5).
- Spatial autocorrelation of the residuals in the linear models was detected. It was not accounted for. However, in future work advanced regression methods accounting for spatial autocorrelation are recommended to overcome this limitation of linear modelling.
- Linear modelling between $\overline{Sx}$ and snow depth indicates that Southern winds are more important for wind-driven snow distribution than Eastern winds.

- Calculation of optimal d_{max} showed that the extent of the influence zone of sheltering features are different from site to site and ranged from 50 m to 200 m.
- Adjustment of the instrument height h improved the prediction capacity of $\overline{Sx}$ in all sites, although to a small extent.
- Calibration of $\overline{Sb}$ was only possible in Breinosa and for the precipitation wind direction. In all other cases, it appeared that $\overline{Sb}$ was not a good predictor of snow depth or that data did not allow the testing of $\overline{Sb}$ as a predictor.

4.4 Model Predictors

The values of the predictors (elevation, slope, radiation index, $\overline{Sx}$ and $\overline{Sb}$) were calculated from the DEM for each location of snow depth measurement. Table 6 gives the basic statistics of the predictors once co-registered with available snow depth measurements.

Table 6: Mean value and standard deviation of the predictors for the four study sites when calculated over the 5 m DEM.

	Breinosa		**Larsbreen**		**Longyearbreen**		**SFS**	
	Mean	σ	Mean	σ	Mean	σ	Mean	σ
Elevation [m]	530.8	82	483.6	25	479.6	69	127.8	30
Slope [°]	10.9	7.1	13.8	6.8	6.6	2.9	7.6	3.1
Dominant aspect	NE		NNE		NNW		S	
Radiation index (out of 100)	23.8	10.1	20.9	5.9	22.7	2.6	35.3	3.1
$\overline{Sx}_{Drift}$ [°]	5.4	6.6	-3.2	10.2	0.1	5.1	-5.2	1.9
$\overline{Sx}_{Precip}$ [°]	3.2	7.6	3.5	7.5	5.1	2.7	-7.5	2.0

The distribution of these values have a direct effect on the predictive capacity of each model within its training site and when applied on another area. Indeed, from Table 6 it can be seen that the predictors take very different values from one site to another. Meaning that in SFS for example, the relationship between snow depth and elevation at that altitude will not be the same as the relationship between the same two variables in Breinosa located ∼400 m higher. Also, within each site, the survey was conducted to sample areas where the predictors were expected to be different.

However, some specific areas such as steep slopes or high ridges could not be surveyed due to difficult accessibility, or avalanche risks. Under-represented values of a variable are known to reduce the reliability of the prediction in areas where predictors take such values. Figure 22 shows the distribution of sampled $\overline{Sx}_{drift}$ values. It can be seen that more than 70% of the samples are taken in areas where $\overline{Sx}$ is between -5° and 5°. It can thus be expected that the model will perform well in areas where $\overline{Sx}$ takes such values and will be less accurate in areas where $\overline{Sx}$ takes under-represented values. The same conclusions can be made by visual inspection of the distribution plots of all predictors displayed in the Appendix B.

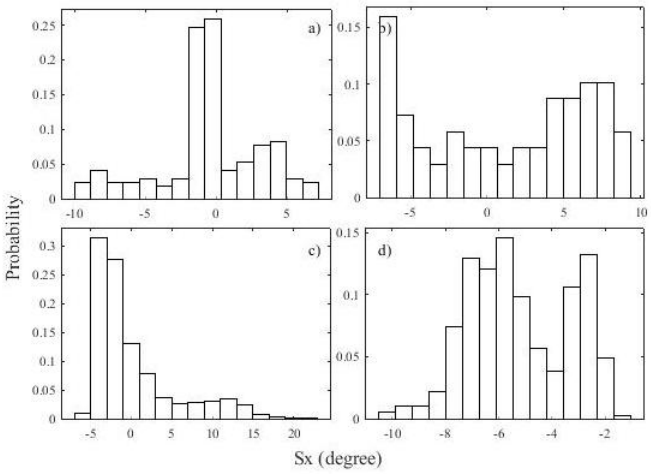

Figure 22: Distribution of samples $\overline{Sx}_{Drift}$ values for the 5 m DEM in a) Breinosa, b) Larsbreen, c) Longyearbreen and d) South Facing Slope.

4.5 Regression Trees

Regression trees were grown for each study site and for both resolutions. An overview of the different models is displayed in Table 7 and 8. Each model is presented, discussed and the two resolutions are compared.

Table 7: Regression trees results for the 5 m resolution.

Site	R^2	Residuals Stand. Dev.	No. Snow Classes	Predictors
1	0.39	±0.59 [m]	4	$\overline{Sx}_{precip}$
2	0.67	±0.57 [m]	2	$\overline{Sx}_{precip}$
3	0.55	±0.27 [m]	9	$\overline{Sx}_{precip}$, Slope, Elevation
4	0.40	±0.20 [m]	9	$\overline{Sx}_{precip}$,$\overline{Sx}_{drift}$,Elevation

Table 8: Regression trees result for the 50 m resolution.

Site	R^2	Residuals Stand. Dev.	No. Snow Classes	Predictors
1	0.36	±0.52 [m]	3	$\overline{Sx}_{precip}$, *Slope*
2	0.84	±0.34 [m]	4	$\overline{Sx}_{precip}$, $\overline{Sx}_{drift}$, Slope
3	0.47	±0.27 [m]	9	$\overline{Sx}_{precip}$, $\overline{Sx}_{drift}$, Elevation
4	0.00	±0.28 [m]	1	Constant model

4.5.1 Breinosa

Model built on the 5 m DEM In Breinosa the regression tree model was cross-validated excluding 10% of the data set. The optimal tree size, evaluated with the the lowest validation error in Figure 23 (left), is achieved for 3 to 4 snow classes. The tree selected for this site, shown in Figure 23, predicts the snow depth accounting four classes based on $\overline{Sx}_{precip}$, indicating that winds coming from South carrying precipitation are the most relevant predictors in the snow redistribution in this area. The model explains 39% of the snow distribution variance.

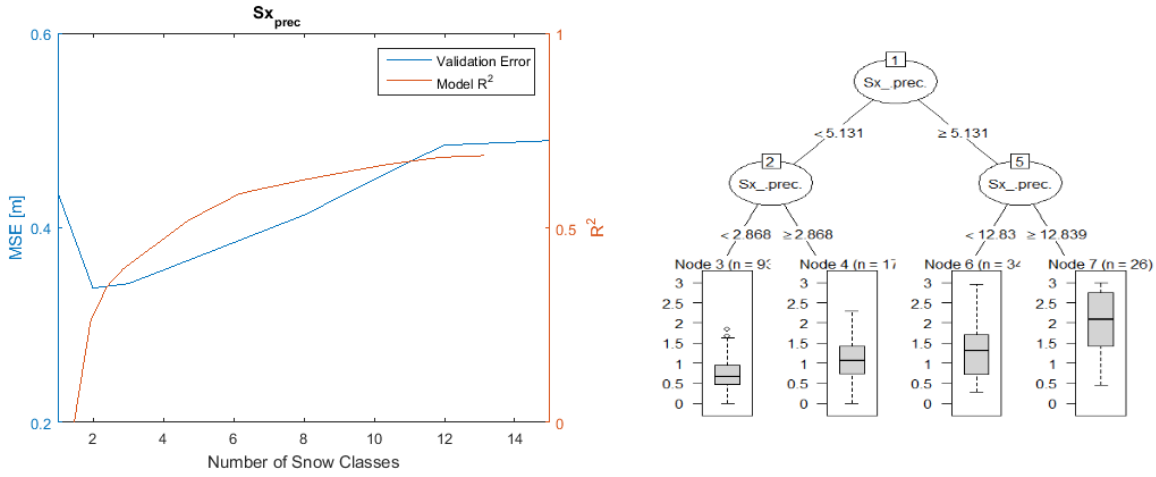

Figure 23: Result of the regression tree growth in Breinosa for the 5 m resolution. On the left side can be seen the average validation error and average R^2 for 100 cross validated trees as a function of tree size. The minimum in validation error is the optimal tree size. The tree that was selected is displayed on the right hand side and box plots show the distribution of snow depth within each class.

In Figure 24 is shown the spatial distribution of the snow depth predicted from the model, compared to the data samples. Also, are shown the residuals of the model. It can be observed that large positive and negative residuals are found close to each other. This indicates that some processes dominating snow distribution for these areas were not explained by the model. However large areas of homogeneous snow depth controlled by the sheltering and exposure to the south-blowing winds (snowy north facing slopes and shallow snow pack on the southern half of the site) were successfully detected.

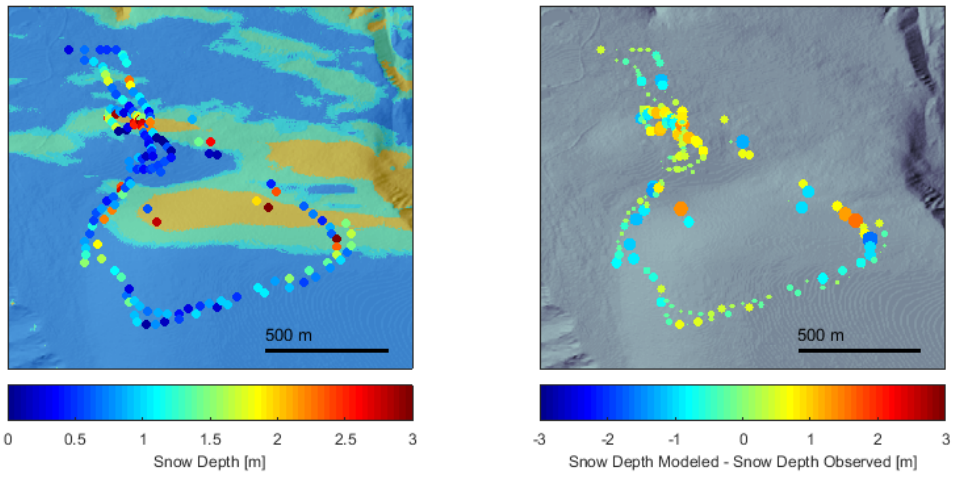

Figure 24: Snow depth map for Breinosa and for the 5 m resolution along with observed snow depth (left). Map of the model's residuals (right).

Model built on the 50 m DEM Using the coarser DEM, the lowest validation error is achieved for 3 snow classes according to the validation error plot of Figure 25. The tree uses $\overline{Sx}_{precip}$ and slope as best predictors. This indicates that the model, regardless the DEM resolution, assigns to the south coming winds most of the explainable variance.

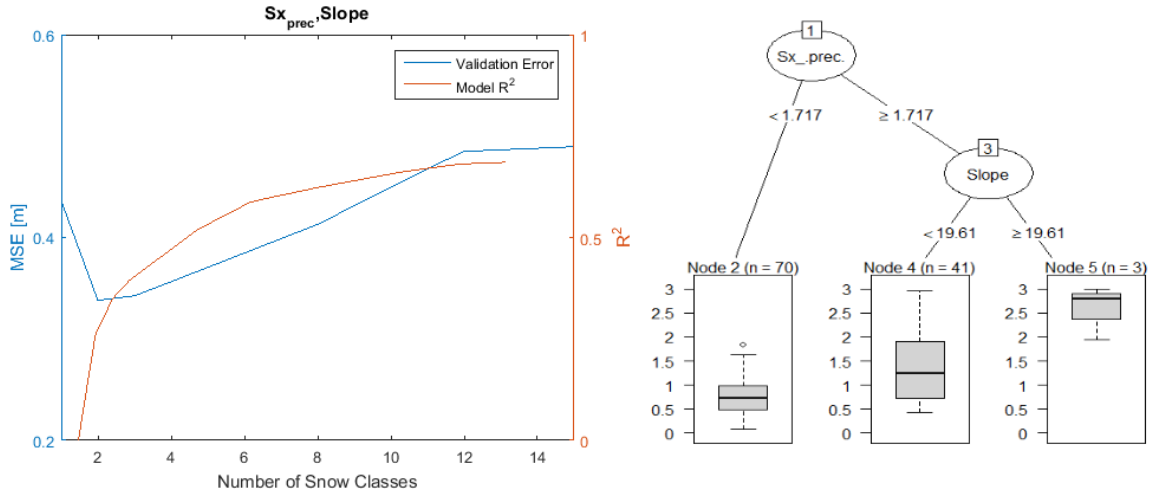

Figure 25: Result of the regression tree growth in Breinosa for the 50 m resolution. On the left side can be seen the average validation error and average R^2 for 100 cross validated trees as a function of tree size. The minimum in validation error is the optimal tree size. The tree that was selected is displayed on the right hand side and box plots show the distribution of snow depth within each class.

By observing the snow depth map and the distribution of residuals in Figure 26 it can be seen that high residuals are located in the same areas as the ones of the 5 m model.

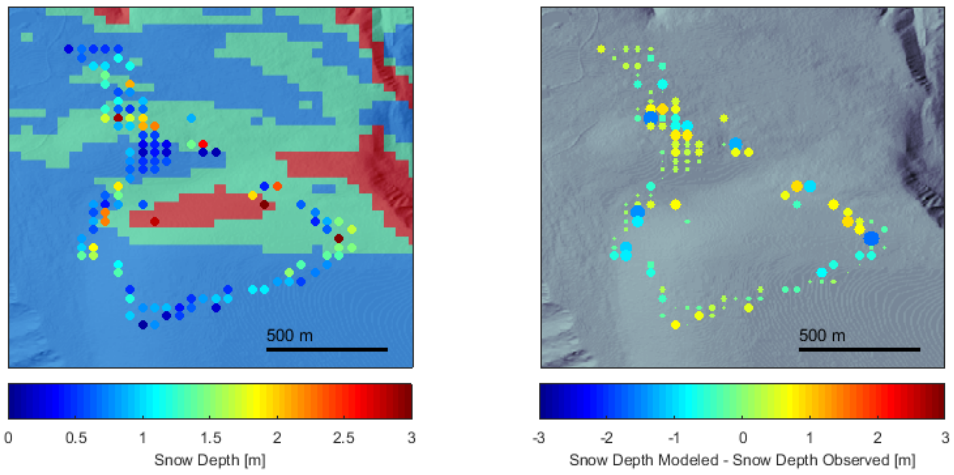

Figure 26: Snow depth map for Breinosa and for the 50 m resolution along with observed snow depth (left). Map of the model's residuals (right).

Comparison Comparing the snow maps generated with the 5 m and 50 m models, it can be noticed that the two regression trees reproduce the same patterns. This results in a similar distribution of the residuals as well and similar performance. In general, since snow depth data averaged on 50 m scale are smoother and therefore "easier" to fit, it was expected a better performance of the model on this resolution. However, the regression tree proved to be able to predict as well small scale variability, with performance indicators of the 5 m model analogue to the 50 m model. This indicates that the model is actually able predict small scale variability and therefore suitable to work with high resolution data obtained by UAV-borne

digital photogrammetry.

It must be also noticed that the snow depth data to be fitted are mean values obtained averaging a certain number of samples over two different grid resolutions. This leads to an uncertainty on the mean snow depth values expressed by the *within cell standard deviation* in Table 1. While the within cell standard deviation is 0.09 m on the 5 m grid, it increases up to 0.16 m when averaging the data on the 50 m grid. The 5 m model fits "more certain" snow depth data making therefore a more reliable estimation of the snow distribution. It must be also noticed that this result is a direct consequence of the sampling method used. If it was known the exact mean snow depth value of each grid cell, regardless the grid resolution, the two model would perform the same in terms of snow volume estimation.

4.5.2 Larsbreen

Model built on the 5 m DEM As for Breinosa, the model in Larsbreen was cross validated excluding 10% of the dataset. Growing the tree it has been noticed that the elevation as predictor produced a negative gradient with snow depth. This is in agreement with the data, since the glacier, where deep snow was measured, is lower than the ridge on the left side of the site, where snow is shallow due to wind exposure. Since this effect is due to the sampling method, the elevation was removed from the model in order to avoid non physically correct prediction. As shown in Figure 27 the optimal tree size accounts 2 to 3 snow classes. But the tree containing 3 snow classes was non-physical so only two classes could be used. The best regression tree achieved, presented in Figure 27, predicts snow depth using $\overline{Sx}_{precip}$ and explains 67% of the measured variance.

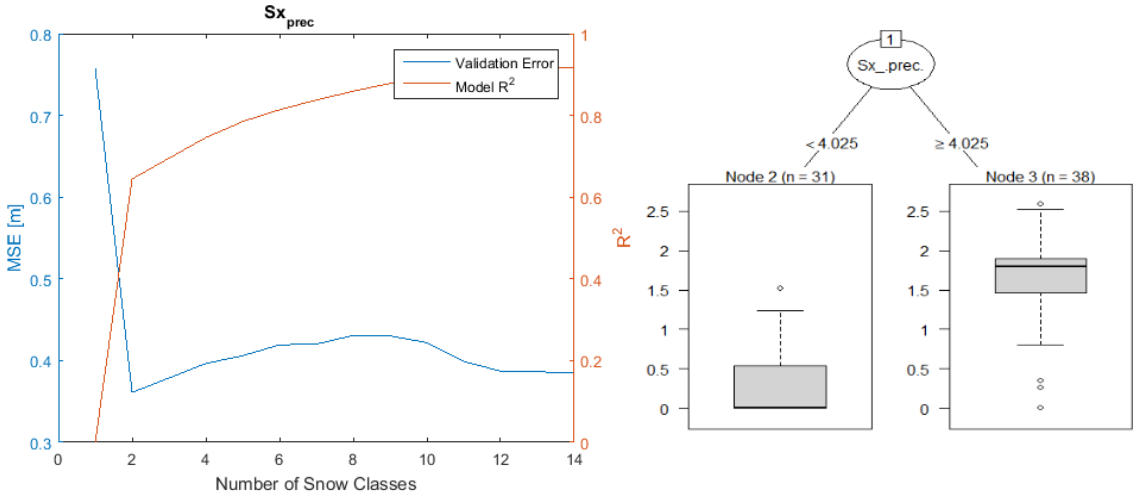

Figure 27: Result of the regression tree growth in Larsbreen for the 5 m resolution. On the left side can be seen the average validation error and average R^2 for 100 cross validated trees as a function of tree size. The minimum in validation error is the optimal tree size. The tree that was selected is displayed on the right hand side and box plots show the distribution of snow depth within each class.

In Figure 28 it can be observed that the model predicts successfully deeper snow on the glacier, that is sheltered from the Southern winds and shallow snowpack on the blown ridge on the left side of the glacier. Considering the residuals map, it can be noticed that high residuals are achieved where the terrain is complex, e.g. on the side of the glacier and over the ridge on the left side of the glacier. In particular, it can be seen that snow depth is overestimated on the North-Eastern side of the ridge and underestimated on the South-Western side of the ridge as if the simulated area was shifted southward. This shift was also reported by Prokop et al.

(2013), and is addressed as a systematic but minor mismatch between simulated and actual accumulation/drift areas.

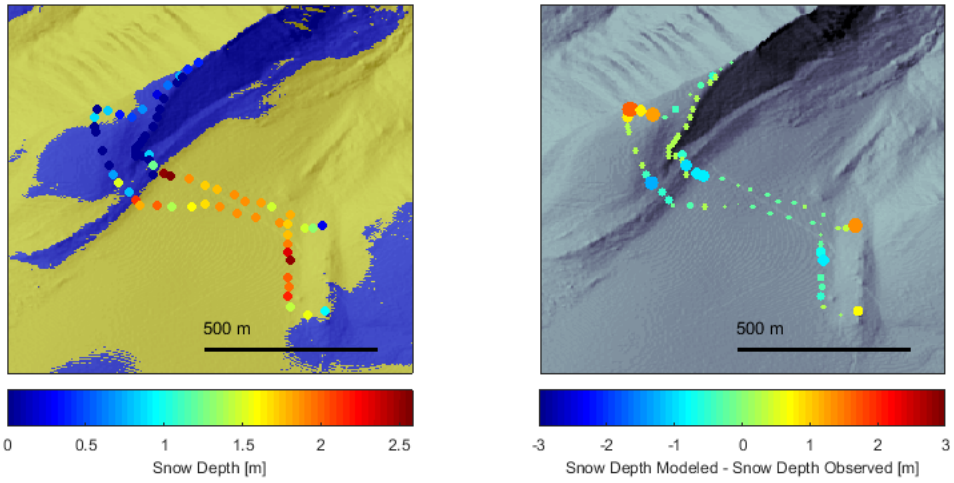

Figure 28: Snow depth map for Larsbreen and for the 5 m resolution along with observed snow depth (left). Map of the model's residuals (right).

Model built on the 50 m DEM As for the 5 m tree, the 50 m tree produced a non physical behaviour of the elevation, which is not used as a predictor. Using the coarse grid improves remarkably the performance increasing by 17 percentage points the explained variance and reducing by half the standard deviation of the residuals (Table 8) using as predictors $\overline{Sx}_{drift}$, $\overline{Sx}_{precip}$ and slope (Figure 29). The snow depth and residuals maps are displayed in Figure 30.

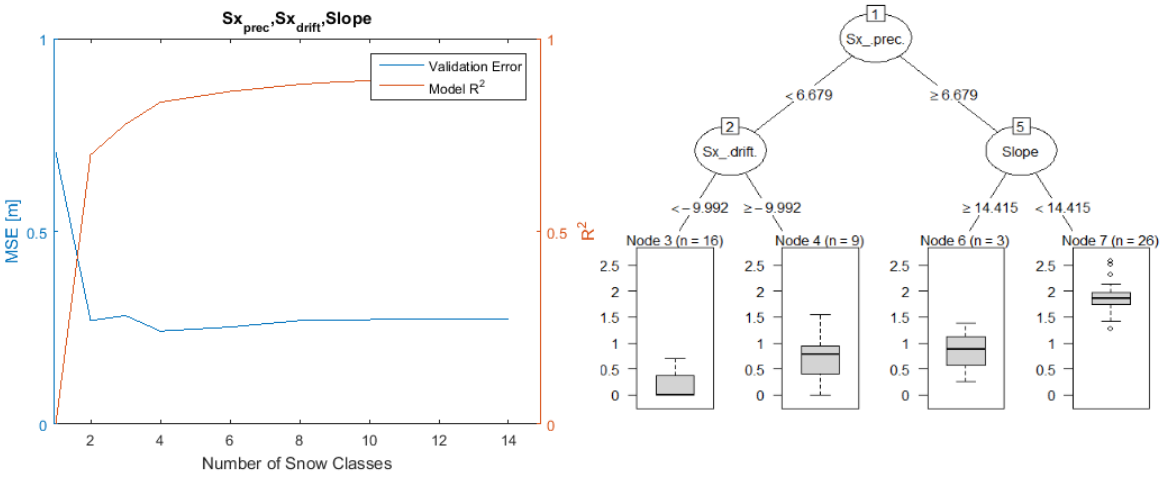

Figure 29: Result of the regression tree growth in Larsbreen for the 50 m resolution. On the left side can be seen the average validation error and average R^2 for 100 cross validated trees as a function of tree size. The minimum in validation error is the optimal tree size. The tree that was selected is displayed on the right hand side and box plots show the distribution of snow depth within each class.

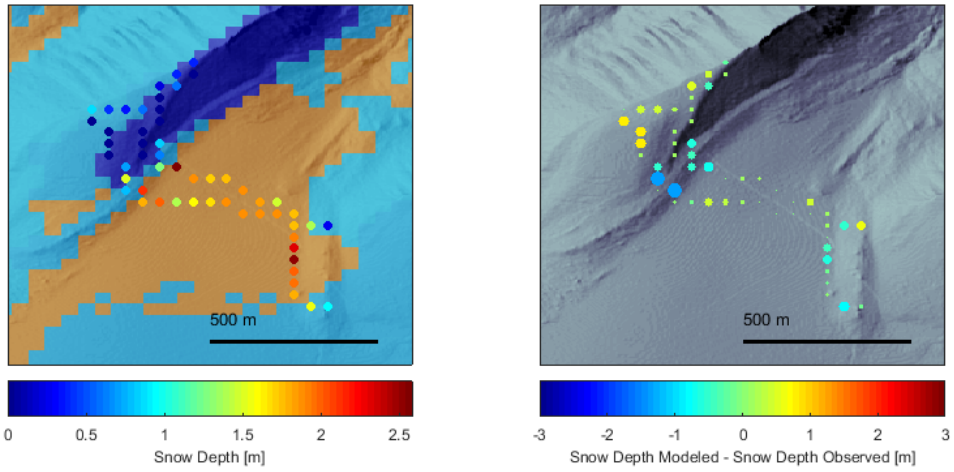

Figure 30: Snow depth map for Larsbreen and for the 50 m resolution along with observed snow depth (left). Map of the model's residuals (right).

Comparison The snow map in Figure 30 shows that the model describes better the sides of the ridge where the 5 m model showed high residuals. This can be addressed to the averaging of snow depth measurements over 50 m cells that smoothed the transition between deep and shallow snow packs. It is interesting to notice also that in the 50 m model $\overline{Sx}_{drift}$ participates to the low snow depth on the ridge to the left while it was not used in the 5 m model.

4.5.3 Longyearbreen

Model built on the 5 m DEM In Longyearbreen the model was cross validated excluding 50 % of the dataset due to the large number of measurement provided by the GPR campaign. In Figure 32 it can be observed that the validation error does not reach an absolute minimum. It rather flattens for more than 14 snow classes (not displayed). This indicates that, after a certain tree size, more complex trees do not improve the performance of the model. Observing the trees it is noticed that trees more complex than a certain number of splits present non physical behaviour of the predictors. Therefore, the optimal tree here is chosen as the biggest tree that does not presents non physical behaviour of the predictors. The resulting tree uses $\overline{Sx}_{precip}$, elevation and slope, predicting nine snow classes and explaining 53% of the data variance.

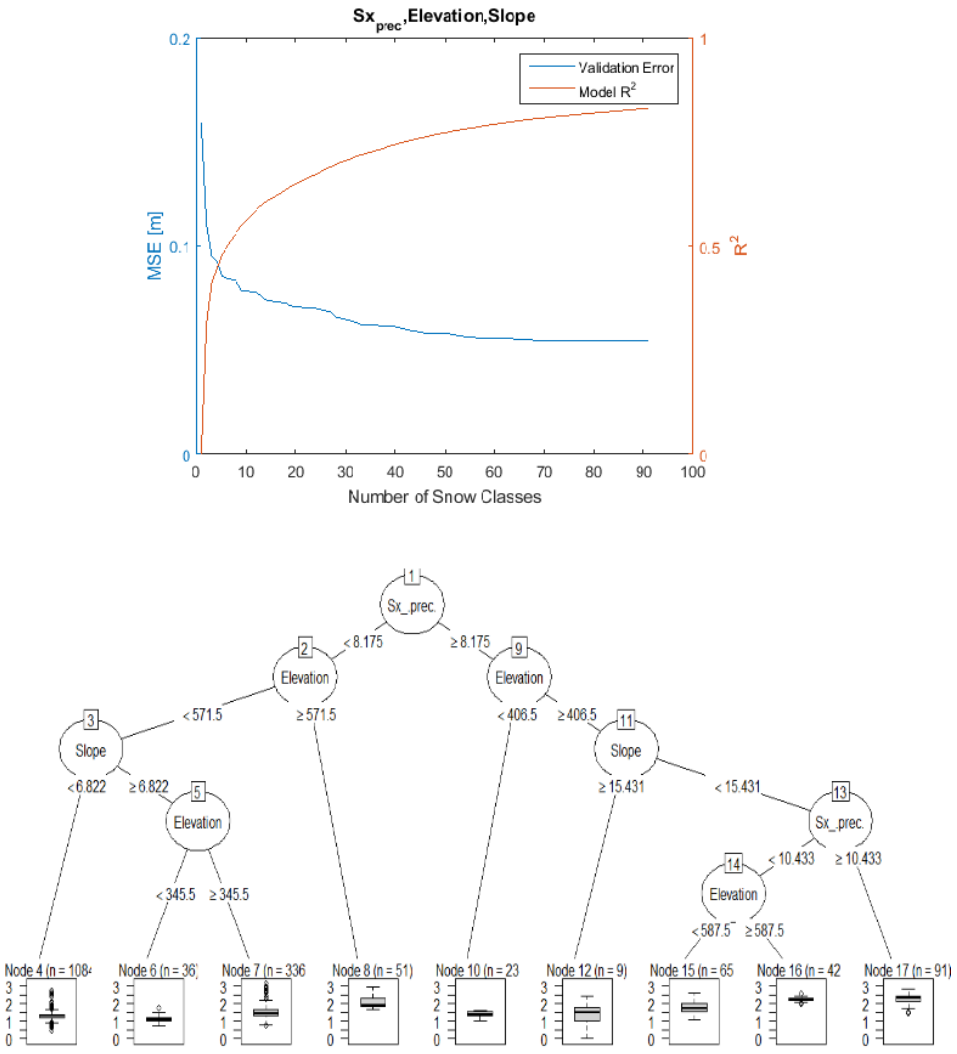

Figure 31: Result of the regression tree growth in Longyearbreen for the 5 m resolution. On the left side can be seen the average validation error and average R^2 for 100 cross validated trees as a function of tree size. The minimum in validation error is the optimal tree size. The tree that was selected is displayed on the right hand side and box plots show the distribution of snow depth within each class.

In Figure 32 it can be seen how the model gets the general trend of the snow distribution. Deep snow is predicted on the sides of the glacier, where snow accumulates on the bottom of the lateral moraines. High snow depth is well modelled also on the top of the glacier, due to the sheltering from the South winds. There is also a clear elevation trend.

Analysing the residuals it can be observed that the model performs well on the glacier surface, while high residuals take place on the side of the glacier, where are located lateral moraines and more complex terrain. This can be due to two things: 1) The central part of the glacier is a more even surface and more samples are taken there. Therefore the model tends to fit this area at the expense of the side of the glacier that is less represented in the dataset. Therefore, this result is a consequence of the sampling design. 2) The processes that determine the snow distribution on the sides of the glacier might not be described by the predictors used in the model.

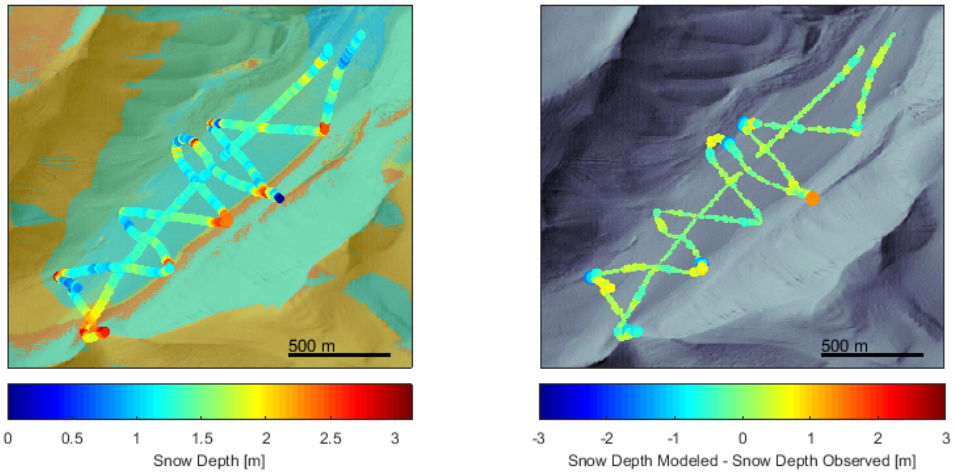

Figure 32: Snow depth map for Longyearbreen and for the 5 m resolution along with observed snow depth (left). Map of the model's residuals (right).

Model built on the 50 m DEM and Comparison Due to the reduced dataset resulted by the coarse grid averaging, the 50 m tree was validated with 10% of the dataset. The optimal performance is achieved at 5 snow classes, using $\overline{Sx}_{precip}$, $\overline{Sx}_{drift}$ and elevation as displayed in Figure 33. The snow depth map along with the model's residuals are shown in Figure 34. The model presents a R^2 of 0.47.

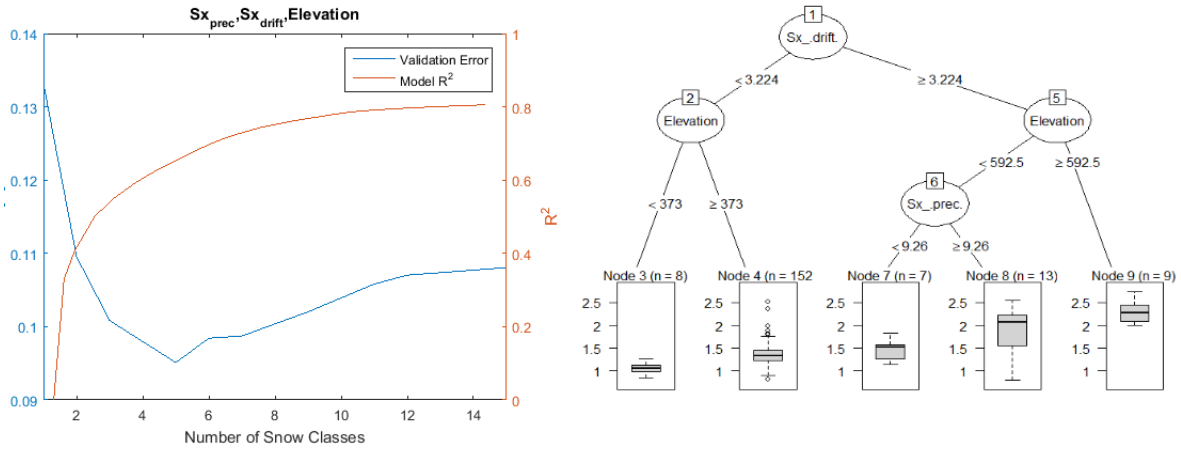

Figure 33: Result of the regression tree growth in Longyearbreen for the 50 m resolution. On the left side can be seen the average validation error and average R^2 for 100 cross validated trees as a function of tree size. The minimum in validation error is the optimal tree size. The tree that was selected is displayed on the right hand side and box plots show the distribution of snow depth within each class.

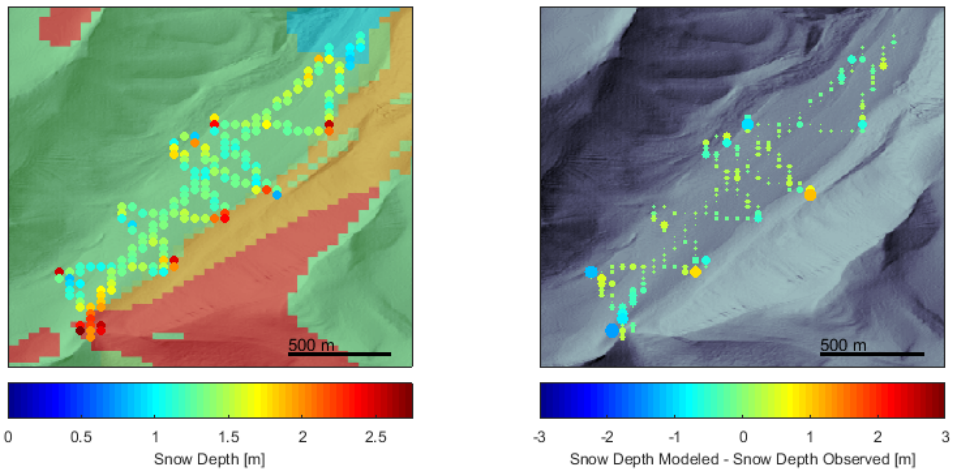

Figure 34: Snow depth map for Longyearbreen and for the 50 m resolution along with observed snow depth (left). Map of the model's residuals (right).

Comparison The R^2 at 50 m resolution is significantly lower than the result achieved with the 5 m model. This indicates that the 50 m model explain more variance of the 50 m grid dataset than the 5 m models does for the 5 m grid dataset. However, since the 50 m dataset has less variability than the 5 m dataset, the standard deviation of the residuals of the two models is eventually equal. This case is similar to the one described for Breinosa. The two models perform the same with regards to snow depth data, meaning that the smoothing of the data due to the 50 m grid averaging does not increase the performance of the model and the regression tree is able to predict small scale variability. Additionally, in the same way as in Breinosa, the snow depth mean values have higher uncertainty on the 50 m grid with a within cell variability of 0.12 m in the 50 m grid versus a within cell variability below 9.5 cm in the 5 m grid. This leads to the conclusion that the 5 m model makes a more reliable prediction than the 50 m model.

4.5.4 SFS

Model built on the 5 m DEM In SFS, as in Larsbreen, the model was cross validated using 50% of the dataset. In Figure 36 it can be observed that the validation error of the regression tree has a similar behaviour as for Longyearbreen, i.e. the increase in tree size after a certain threshold does not improve the prediction capacity of the model. Therefore,the best tree is chosen using the principle of biggest tree that did not present non-physical behaviour described for the 5 m model built in Longyearbreen. The resulting model predicts 9 snow classes using $\overline{Sx}_{precip}$, $\overline{Sx}_{drift}$ and elevation and explaining 40% of the data variance.

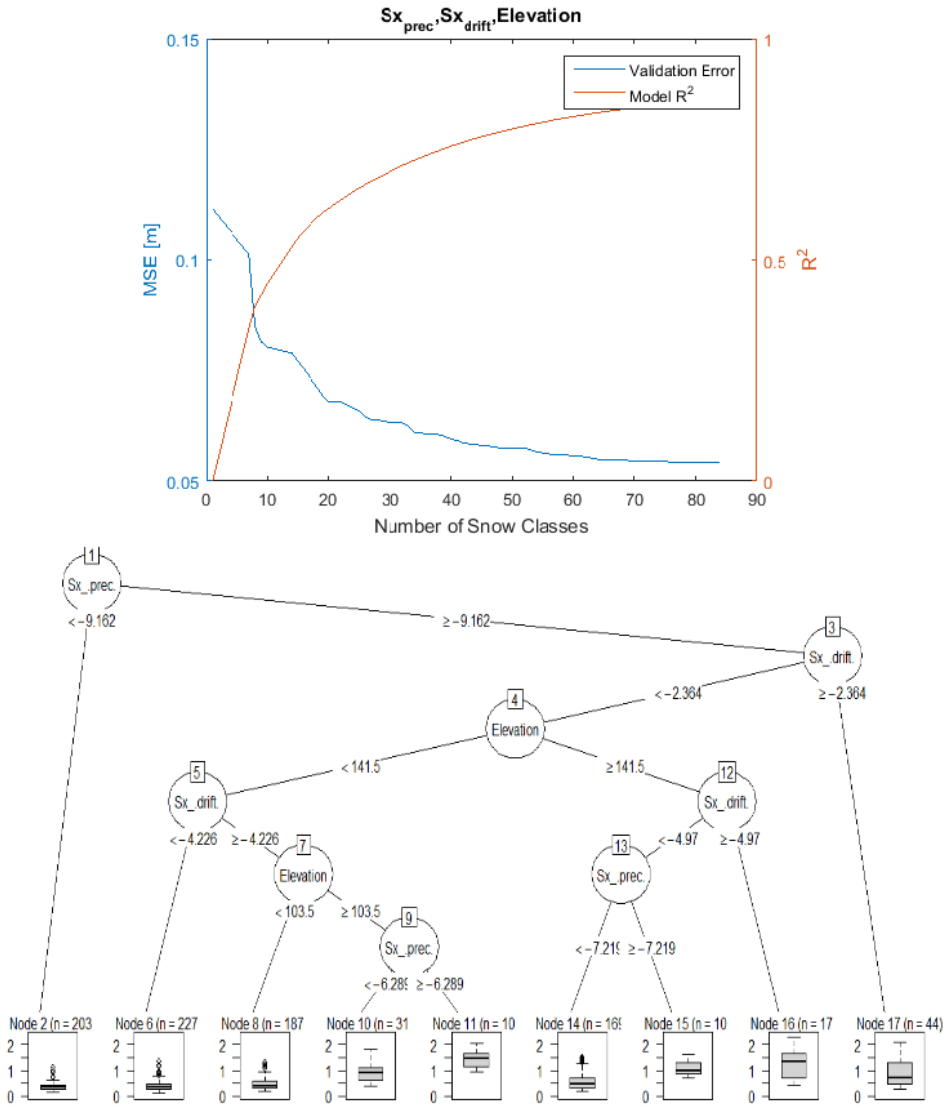

Figure 35: Result of the regression tree growth in SFS for the 5 m resolution. On the left side can be seen the average validation error and average R^2 for 100 cross validated trees as a function of tree size. The minimum in validation error is the optimal tree size. The tree that was selected is displayed on the right hand side and box plots show the distribution of snow depth within each class.

Observing the residuals of the model (Figure 36) it can be noticed that the there are specific zones where the model gives higher residuals. However, the complex topography of the site makes difficult determine the cause of these deviations.

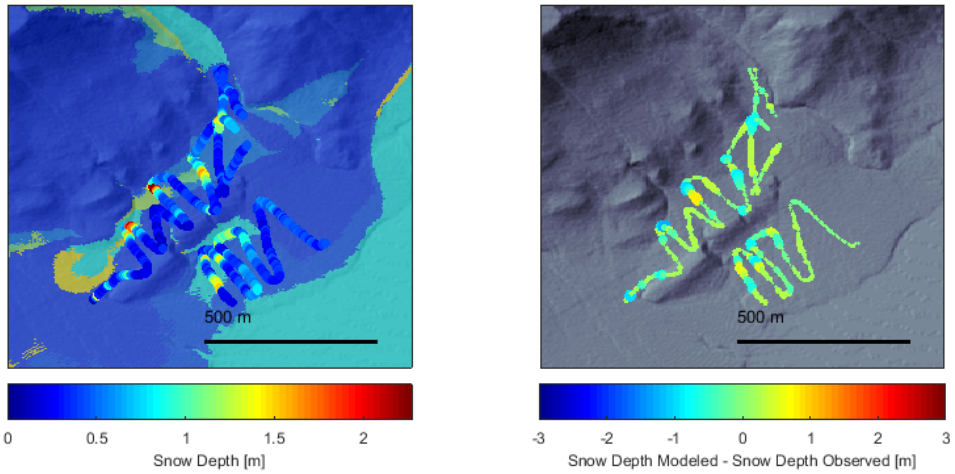

Figure 36: Snow depth map for SFS and for the 5 m resolution along with observed snow depth (left). Map of the model's residuals (right).

Model built on the 50 m DEM and Comparison Due to the reduced dataset resulted by the coarse grid averaging, the 50 m tree was validated with 10% of the dataset. As it can be seen in Figure 37, the validation error increases from the first split and for all tree sizes. It shows that splitting the dataset into classes can only increase the validation error. Therefore the regression tree is not capable to make a reliable prediction. Since no split can help to explain the data variability, it is usually said that a model assigning average snow depth to all points of the area would be more accurate that a regression tree model.

Another interpretation is that by averaging snow depth over a coarser grid, the predictor are not able to describe snow depth any more. Indeed if the features that create high or low snow depth in SFS are less than 50 m wide, they do not appear on the DEM and the predictor cannot account for them. Therefore it is concluded that in SFS the snow distribution processes occur to a scale smaller than 50 m. Considering the small size of the site ($\approx$0.7 km^2), its homogeneous snow pack and rolling topography, this result was expected.

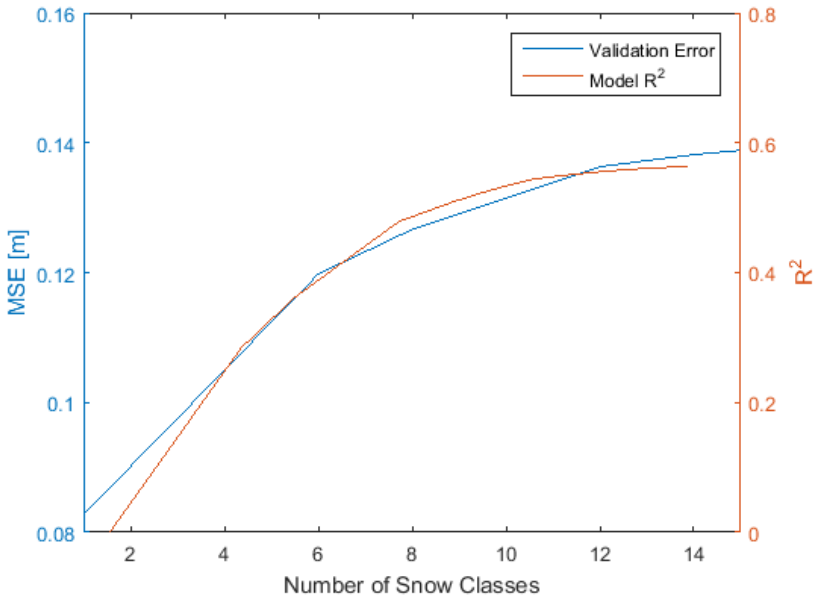

Figure 37: Result of the regression tree growth in SFS for the 50 m resolution. The increasing validation error indicates the failure of the regression tree model.

Key Findings

- Regression trees successfully models snow depth distribution giving R^2 ranging from 0.36 to 0.84.
- Only in SFS for the 50 m DEM no model could be found because of distribution processes acting at a smaller scale than 50 m grid cell.
- In three sites out of four the models built using the 5 m DEM performed better than the one using the 50 m DEM, meaning that the chosen predictors and the regression tree models perform better for higher resolutions.

4.5.5 Comparison with Previous Studies

As already mentioned, statistical modelling has already been tested outside of the Arctic, showing good agreement between data and simulations. In this section are presented the results of some previous researches involving the use of regression trees in order to compare the results of the present study. A summary of previous findings is shown in Table 9. It must be noticed that quantitative comparisons are problematic due to the nature of the regression trees. As discussed previously, these models are very sensitive to the data, to survey design, to grid resolution, to the size until which the tree is grown and even to the quality of the DEM it is built on (Molotch et al., 2005). Each study therefore represents a specific case.

Additionally, in the present study the trees are grown avoiding non-physical splits in order not to over-fit the data. However, it was noticed that this criteria was not always respected in other studies. Nevertheless, a qualitative comparison is still reported to contextualize the goodness of the present results.

By comparing the model performances, i.e. R^2, it can be observed that the current study is in line with previous work. The best reported model is the one presented by Winstral and Marks (2002), achieving R^2=0.50. His regression tree, grown to 16 snow classes, is built on a 2.25 km^2 watershed using a grid resolution of 10 m. The most similar model in the present study is the 5 m model built in Longyearbreen because of site dimension, tree size and DEM resolution. The 5 m regression tree model of Longyearbreen achieves a R^2 = 0.55 using 3 predictors in 9 snow classes and is therefore very similar to the result of Winstral and Marks (2002).

Erxleben et al. (2002) models snow distribution on a small site, characterized by a low variance snow depth distribution, using a coarse DEM. The model performance is relatively low, achieving a R^2=0.25. This result can be compared to the one obtained in SFS using the 50 m DEM. In both cases the regression tree was hardly (or not) able to find a valid correlation between predictors and snow data. Comparing these two results it can be inferred that in small sites where snow distribution does not show much variability, high resolution grids might be necessary to improve the modelling performance.

In general, the models obtained in the present study achieve good performance by using a relatively small set of predictors. This indicates that in the Central Svalbard the snow distribution is controlled by fewer processes than in other regions where previous studies were conducted. The importance of the wind exposure index Sx or the absence of Radiation Index from all models are in agreement with the climate of Svalbard. Indeed severe winds and storms shape the snow distribution while snow melt triggered by solar radiation rarely occurs during the period of the study. It shows that regression tree models could successfully infer the specificities of the local climate from the snow distribution.

Table 9: Summary of previous studies concerning snow depth distribution modelling using regression trees built on the same predictor set used in the current study.

Other Studies :	R^2	**Snow Classes**	**Study Area**	**Grid Resolution**
Erxleben et al. (2002)	0.25	12	1 km^2	30 m
Winstral et al. (2002)	0.50	16	2.25 km^2	10 m
Molotoch et al. (2005)	0.27 - 0.35	7 -8	19 km^2	27 - 30 m

4.5.6 Transferability of Models to Other Sites

The transferability of the models was tested by applying each model to the remaining sites, following the so called cross simulation. This part aims at assessing whether the control of the predictors on snow depth are similar from site to site or if each model is site specific. The performance of each model in each site are assessed using the R^2, Mean Error (ME) and the 95% prediction interval (p.i.). In Tables 10 and 11 are presented the results for the 5 and 50 m models. In most cases, the models have poor accuracy in predicting snow distribution in other sites, producing negative or null R^2 coefficients.

Table 10: Cross-prediction of 5 m models. Model 1, 2, 3 and 4 are the models built respectively in Breinosa, Larsbreen, Longyearbreen and SFS.

		Breinosa	**Larsbreen**	**Longyearbreen**	**SFS**
	R^2	0.39	0.01	-0.72	0.07
Model 1	ME [m]	0.00	-0.29	0.56	-0.21
	p.i. [m]	1.15	1.35	1.58	1.46
	R^2	0.35	0.67	-0.28	0.05
Model 2	ME [m]	0.06	0.00	0.62	-0.08
	p.i. [m]	1.32	1.11	1.47	1.64
	R^2	-0.50	-3.03	0.55	-1.57
Model 3	ME [m]	-0.29	-0.28	0.00	-0.43
	p.i. [m]	0.77	1.47	0.53	0.93
	R^2	-0.41	-0.46	-0.14	0.40
Model 4	ME [m]	0.21	-0.23	0.70	0.00
	p.i. [m]	0.65	0.65	0.70	0.52

Table 11: Cross-predictions of 50 m models. Model 1,2 and 3 are the models built respectively in Breinosa, Larsbreen and Longyearbreen. No model could be built in SFS for the 50 m DEM.

		Breinosa	**Larsbreen**	**Longyearbreen**	**SFS**
	R^2	0.36	-0.07	-0.71	
Model 1	ME [m]	0.00	-0.16	0.46	
	p.i. [m]	1.03	1.29	1.41	
	R^2	0.27	0.84	-0.35	
Model 2	ME [m]	0.08	0.00	0.32	
	p.i. [m]	1.38	0.66	1.53	
	R^2	-0.16	-1.93	0.47	
Model 3	ME [m]	-0.09	-0.34	0.00	
	p.i. [m]	0.75	0.97	0.52	

This result is interpreted as follow. Even though almost all the models have Sx_{prec} as root predictor, indicating that in almost all the sites the precipitation wind direction is the dominant process redistributing snow, the data-based models fit the site-specific data only. This leads to an intrinsic specificity of the model with respect to the data that the model itself is built on. In other words, in two different sites where $\overline{Sx_{prec}}$ is recognized as dominant process, similar snow depths can be still described by very different values of $\overline{Sx_{prec}}$, depending on the specificity of site and the sampling strategy. Since no explicit physical process is taken into account into statistical modelling, data are controlling the models making them not suitable for transferability on different datasets.

Furthermore, it must be remembered that the regression trees are grown on the optimal wind exposure indexes, that are obtained by calibration. The calibration is performed site by site, leading to site-specific values of d_{max} and h, as shown in tables 4 and 5. On the other hand, the cross simulation process consists in simulating snow depth distribution in a site using wind-driven predictors that are not necessarily optimal for that specific site, because calibrated elsewhere. This leads in a reduction in significance of Sx in the simulation, reducing the model performances when tested in other sites.

The only model producing positive results is the tree built on Larsbreen when tested in Breinosa for both the grid resolutions. The R^2, the bias and the confidence interval are comparable to the values obtained with Breinosa's own model. This is due to the fact that in both

the sites samples were acquired in sheltered-exposed areas from the south winds. In Figure 38 it can be observed that Larsbreen's model reproduces the same wind shelter pattern as Breinosa's model does. It has to be noticed that the Breinosa's model does not produce positive results when applied in Larsbreen, since it tends to over estimates the snow depth on the right slope and underestimate it on the glacier surface.

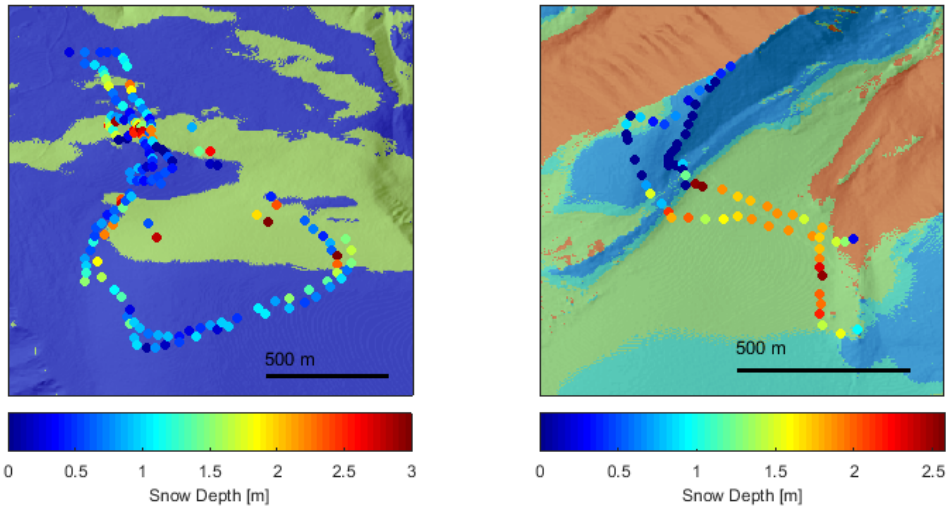

Figure 38: Snow depth map for Breinosa as predicted by the model built for Larsbreen (left) and snow depth map in Larsbreen as predicted by the model built in Breinosa (right) at 5 m resolution.

It is quite surprising that models built for Larsbreen and Longyearbreen are not performing well on each other's site. The two glaciers, close to each other and in similar topographic situations, could easily be assumed to undergo the same snow distribution processes. It can be explained by the different survey techniques that were used in the two sites. In Larsbreen for example, the survey focused on gathering snow depth information about sheltered/exposed areas and the effect of elevation could not be assessed since the higher part of the glacier could not be surveyed. In Longyearbreen however, the elevation plays an important role since four splits are made on elevation for the 5 m model. The survey was made with snowmobile-hauled GPR areas of drastic changes in exposure/sheltering could not be surveyed because of limited accessibility. Thus it can be seen that manual probing and snowmobile-hauled GPR will emphasize different processes because of the different areas that they cover due to accessibility restrictions.

This leads to the necessity of development of better techniques to survey snow depth in complex terrain. Indeed, a suitable survey technique should give the same importance to rolling areas and to steep slopes. This limitation of the conventional methods (manual probing and GPR) are commonly known and motivated the investigation UAV-borne photogrammetry to map snow depth in complex terrain without restriction on the accessibility. It is then believed that regression tree modelling would benefit in great extent from the high resolution data from the UAV.

Key Findings

- Most models were found to be site specific, indicating that they perform well only on the dataset they are built on. Statistical models are known to present this feature, which is their weak point.
- This issue is mostly due to the fact that regression tree models focus on the few most dominant distribution processes that are different for each site.
- Only the model built in Larsbreen could be successfully used in Breinosa.
- The lack of transferability of the models is addressed to survey methods limitations. Other snow depth survey techniques, such as UAV-borne digital photogrammetry, are expected to address these limitations.

4.6 Longyearbreen SWE Storage Estimation

In this part, three models (regression tree, constant model and elevation gradient model) are used to estimate the total storage SWE in Longyearbreen's snow cover. Their results are then compared.

Regression Tree Model: The regression trees grown for Longyearbreen using the 5 m and 50 m DEM are used to generate a SWE map over the entire glacier surface. SWE was calculated for each cell using equations 9 and 10 considering a constant snow density $\rho = 380[kg/m^3]$. Figure 39 presents the results of the SWE distribution models, while in Table 13 are presented the total SWE storage of the glacier as calculated by the regression tree models for both resolution.

The two regression tree models using different resolutions assign the same snow depth in most of the site. They agree in assigning the highest SWE to the right side of the top of the glacier . This suggests that most of Longyearbreen's accumulation takes place in that area. Also, both models predict a significant elevation gradient. The main difference between the two models is given by the left side of Longyearbreen's upper part, where the first model predicts a relatively high SWE, while the second model assigns the same SWE as the central part of the glacier. But scarce data for this specific area makes it difficult to assess which simulation is closer to the reality.

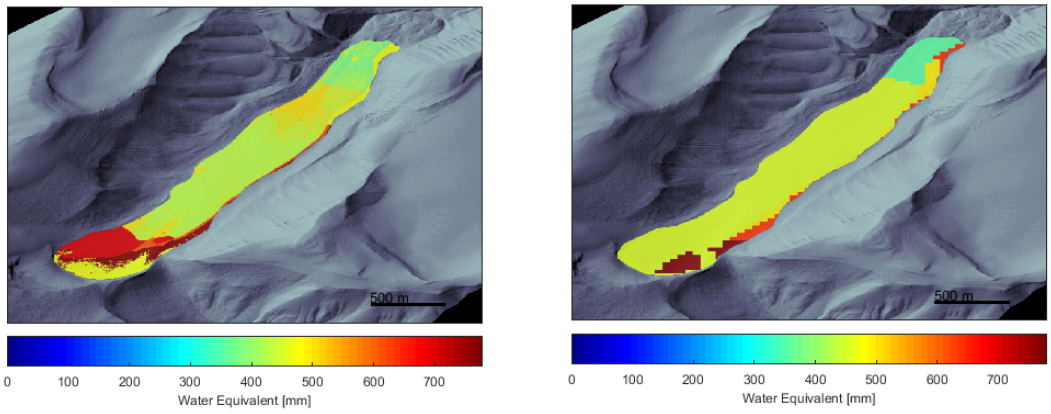

Figure 39: Regression tree models for SWE distribution on Longyearbreen using the 5 m (left) and 50 m (right) resolutions.

The two models estimate a very similar total SWE storage for the snow cover of the glacier (Table 13). The prediction interval of the 5 m model is about 9 percentage point lower than the confidence interval of the 50 m model. This is due to the fact that the 5 m grid has higher precision in defining the glacier boundaries, while the 50 m gird exceeds the boundaries due to the coarser resolution of the cells.

Constant model: As a consequence of Equation 30, a model that predicts for each point the mean observed snow depth will have a R^2 of zero. Also the prediction interval of this model is defined by the standard deviation of the snow depth data at 5 m or 50 m resolution. The total SWE storage that this model predicts on Longyearbreen is reported in Table 13.

Elevation Gradient Model: In Figure 40 is shown the linear regression between snow depth and elevation, while in Table 12 are presented the results of the linear regression. The two resolutions, 5 m and 50 m, lead to the same elevation gradient of 15 cm / 100 m, presenting only a slightly different offset. It can already be noticed that with low R^2 of 0.07 and 0.08, this model fits poorly the snow depth data compared to what was presented for the regression tree model.

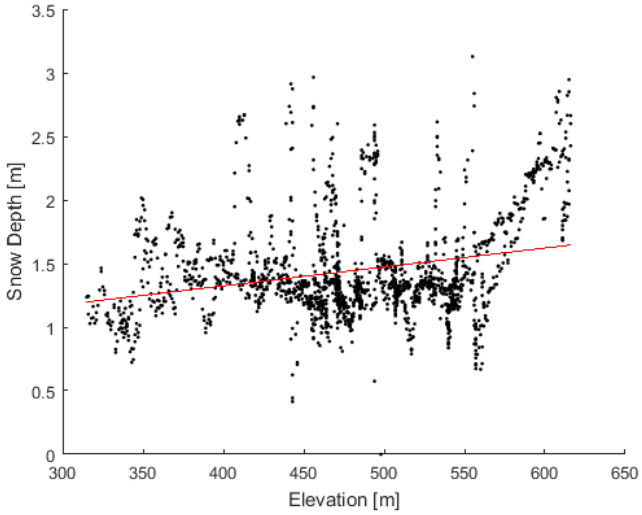

Figure 40: Linear regression to obtain the elevation gradient model in site 3 for 5 m resolution. The regression confirms that there is a positive correlation between elevation and snow depth.

Table 12: R^2 and parameters of the elevation gradient model $SD = \alpha z + y_0$ for both resolutions.

	R^2	α	y_0
5 m resolution	0.07	0.0015	0.73
50 m resolution	0.08	0.0015	0.69

Comparison between the three models Table 13 shows the total SWE storage estimate for all three models and at both resolutions along with the prediction interval.

It can be observed that the uncertainty (i.e. the prediction interval) of the SWE estimation given by the elevation gradient($\sim$ 3.76 and $\sim$ 4.31 for the 50 and 5 m model) is similar the one given by the constant model ($\sim$3.76 for both resolution). In other word, using an elevation gradient to describe SWE is not more precise than the SWE is constant in the whole area.

Addiotionally, by comparing the p.i. of the regression tree models with the other two models,it can be seen that the regression tree modelling framework reduces the uncertainty by the 33% using the 5 m grid and 15 % using the 50 m grid. This could have been expected by comparing the R^2 of the different models: 0 for the constant model, 0.08 for the elevation gradient and 0.47 to 0.55 for the regression tree model. However, this application gives a realistic illustration of how regression tree snow distribution models reduce substantially the uncertainty in Snow Water Equivalent estimations.

Table 13: Models prediction of the total water equivalent volume other the Longyearbreen surface.

	TOT_{swe}	$\pm p.i._{swe}$ $[\times 10^5 m^3]$
Regression tree model		
built on 5 m DEM	8.13	±2.90
built on 50 m DEM	7.72	±3.18
Constant model		
built on 5 m DEM	7.95	±4.31
built on 50 m DEM	7.85	±3.76
Elevation gradient model		
built on 5 m DEM	8.02	±3.76
built on 50 m DEM	7.95	±3.39

Key Findings

- A total SWE of $8.13 \pm 2.90 \times 10^5 m^3$ was estimated in the snow pack of Longyearbreen with the regression tree model at a 5 m resolution.
- Considering its precision interval, the regression tree built at a 5 m resolution demonstrates to give the most precise estimation when compared to a 50 m resolution, to a constant model or to an elevation gradient model.

5 Conclusion and Recommendations

Snow depth and snow density were surveyed in four sites around Longyearbyen in Svalbard and for each site regression tree models for snow distribution based on elevation, slope, $\overline{Sx}$ and a radiation index were built based on a 5 m and 50 m DEM. Each regression tree model was tested on the remaining sites to assess their transferability. Eventually, the snow distribution model built for Longyearbreen was used to estimate the total SWE storage of the snow pack over Longyearbreen glacier and was compared to constant and elevation gradient models.

The snow distribution models presented here showed performances (in term of R^2) that are in agreement with previous studies (Table 9). The 5 m regression tree models had R^2 ranging from 0.39 to 0.67, giving a satisfying agreement between model and snow depth data. They also showed higher R^2 than the 50 m model in all sites except Larsbreen, indicating that the regression tree benefit from finer grid resolution. In SFS this fact was even more pronounced since a 5 m resolution was required to capture snow distribution processes. The 50 m model indeed, failed at finding significant relationship between predictors and snow depth due to the coarse resolution. Erxleben et al. (2002) encounters the same issue by observing low performance of the regression tree for coarse resolution and for small areas presenting low snow depth variability witch is also the case of SFS. It correlates the present result that high resolution grids is beneficial, and even necessary in some case, to snow distribution modelling using regression tree. It can be reminded that the present work was also aiming at assessing the capacity of regression tree models to be calibrated on high-resolution snow depth data acquired by UAV-borne photogrammetry. And to this regards, the present result shows that the regression trees benefit significantly from a higher resolution which make them perfect candidates to be calibrated by the snow depth data acquired from UAV-brone digital photogrammetry.

By analysing the predictors used in the regresssion trees models, other interesting conclusions can be made.

In this study, it is proposed to use of two wind directions and therefore two $\overline{Sx}$: one for the direction of strong winds and the other for the direction of precipitation-carrying winds. This addition to previous studies using $\overline{Sx}$, where only the strongest wind were accounted for, appeared to increase the quality of the model. Indeed, for all models, the most relevant predictors (first split in the regression tree) were $\overline{Sx}_{drift}$ and $\overline{Sx}_{precip}$ with highest relevance for this last one (since it is present in all trees). It clearly indicates that the precipitation-carrying winds have greater influence on snow distribution than strong winds. Therefore the addition of $\overline{Sx}_{precipitation}$ for is thus recommended to future uses of $\overline{Sx}$ in snow distribution modelling. Also, this improvement indicates that the presented method would benefit from wind field modelling and should be conducted in further work.

Furthermore, it could be observed that satisfactory regression trees could be built using a reduced list of predictors ($\overline{Sx}_{precip}$, $\overline{Sx}_{drift}$, Elevation and Slope) that in previous studies. It indicates snow distribution in Svalbard is controlled by fewer predictors than other regions where these models were tested. Additionally, in all presented trees, high importance is given to the wind exposure indexes (presnt in all trees and in successive splits) while the radiation index was not found to correlate with the snow depth data in any site. This is in agreement with the climate of Svalbard, where severe winds play a major role in snow redistribution and radiation-driven snow melt events are rare due to low temperature and low sun angle in winter. This result indicates that regression trees, by determining which processes control the snow distribution, are able to infer the specificities of the local climate from the snow depth data.

The regression tree models built in Longyearbreen lead to a reduction in total SWE esti-

mation uncertainty of 33% (or 15%) compared with constant snow depth model and elevation gradient model when conducted at a 5 m (or 50 m) resolution. This result indicates that this modelling framework is a suitable tool to reduce the uncertainties in SWE estimations in glaciology or hydrology.

However, several limitations of the presented method could be found and recommendations to address them were presented.

Spatial autocorrelation has been detected in the residuals of the linear regressions used for the calibration of $\overline{Sx}$. This violation of the linear modelling assumption can lead to biased estimate of the linear regression coefficients and to reduce the predictive capacity of $\overline{Sx}$. Also, studying the residuals of the snow distribution models, it could be seen that high residuals were located close to each other leading to some extent to spatial autocorrelation. Though this issue was not accounted for in this study. Advanced regression methods, that account for spatial autocorrelation of the residuals, can therefore improve the calibration process and hence the regression tree performance.

The second predictor for wind-driven snow transport $\overline{Sb}$ could not be calibrated and its influence on snow distribution could not be assessed. This problem is addressed to the snow depth measurement method, that could not capture areas where $\overline{Sb}$ is expected to affect snow depth because of inaccessibility. It is believed that the remote sensing of snow depth, e.g. from UAV-borne photogrammetry, could allow to survey areas where $\overline{Sb}$ could be calibrated and by adding $\overline{Sb}$ to the list of predictors, improve the regression tree models.

The regression trees appeared to be very site specific, i.e. snow distribution models are not interchangeable between different sites. For sites such as Breinosa and SFS, it is normal to see that their snow distribution models are not interchangeable since their difference in elevation, in exposure to the wind will enhance different snow distribution processes. But for similar sites such as the neighbouring Longyearbreen and Larsbreen, the snow distribution processes could be expected to be the same. Nevertheless, their snow distribution models were different. It is addressed to the difference of snow survey methods that lead to different datasets in the two sites. Indeed while manual probing allowed to survey relatively steep slopes and wind exposed ridge on Larsbreen, the smooth surface of the glacier could be sampled only in its lower part because to stay away from crevices. On the contrary, the use of GPR on Longyearbreen allowed to survey the entire surface of the glacier, but the steeper slopes and exposed/sheltered areas could not be accessed. In that situation the regression tree model will just fit to its dataset and different datasets will lead to different models. To address this issue, the authors recommend a different snow survey method, such as UAV-borne photogrammetry, that can capture at the same time large rolling areas, ridges and steep slopes not accessible by conventional methods.

Part II
Snow Reflectance Estimation Using DSLR Camera

6 Introduction

Unmanned Aerial Vehicles (UAVs) have undergone great technological improvement in the last decade with extended autonomy and increased payload. In the same way consumer grade digital cameras have offered always better imagery possibilities for always lighter and smaller devices. Additionally increasing interest has been given to digital cameras to extract spectral radiance, luminance or reflectance data from the numerical images (Debevec and Malik, 1997; Wüller and Gabele, 2007; Dymond and Trotter, 1997; Tohsing et al., 2013). Mounted on aircrafts to survey optical properties of clouds (Erhlich et al., 2012) or vegetation (Dymond and Trotter, 1997) or combined with UAVs for observation on crop (Lebourgeois et al., 2008; Lelong et al., 2008), digital cameras have however been used in few occurrences to measure snow and ice reflectance or albedo (Hakala et al., 2010; Corripio, 2004).

Snow albedo and snow reflectance (the former being inferred from the latter) influence to a great extend the energy balance of snow covered areas (Cline, 1997; Marks and Dozier, 1992) and thus can be used to predict snow melt (Marks et al., 1999). Also, by its link to snow physical characteristics (Warren and Wiscombe, 1980; Wiscombe and Warren, 1980), reflectance and albedo can be used as a validation tool for snow transport model (Corripio et al., 2004) and to map different types of snow. Standard approaches to estimate snow reflectance in large areas are interpolation of ground measurements or remote sensing from satellites. However, while the former method can introduce large errors, due to the spatial variability of snow reflectance (Knap and Oerlemans, 1999), the latter presents severe cost and use limitations. In that regards, UAV-borne imagery can embody an affordable, fast and accurate tool to map albedo and reflectance of large and complex snow covered areas where conventional methods would be more pricey, more time-consuming or dependant on external services.

The present study investigates an alternative approach to Hakala et al. (2010) to extract snow reflectance from digital aerial images with a different camera calibration and a different snow reflectance estimation method. The new calibration does not require the complex experiment to extract spectral sensitivity of the camera and the snow reflectance is inferred by estimating luminance from the digital images (Roy et al., 1998; Wüller and Gabele, 2007; Tohsing et al., 2013). Furthermore, no discussion of the precision of digital cameras in reflectance mapping has been found in the litterature. Therefore the present study also discusses sources of noise and errors related to the digital camera which affect the reflectance measurement.

Due to restrictions in time, the study was limited to the following points:

- The scientific background necessary for the understanding of the scope of this method and defining the quantities that are to be measured.
- A simple calibration method for the camera.
- A discussion of the error linked with digital camera imagery and of the precision of the method.
- The estimation of snow reflectance values from a single pictures.
- A study of the stability of the measurement from picture to picture.

- Recommendations for the further work to conduct.

The process leading to the estimation of snow reflectance is illustrated in Figure 41.

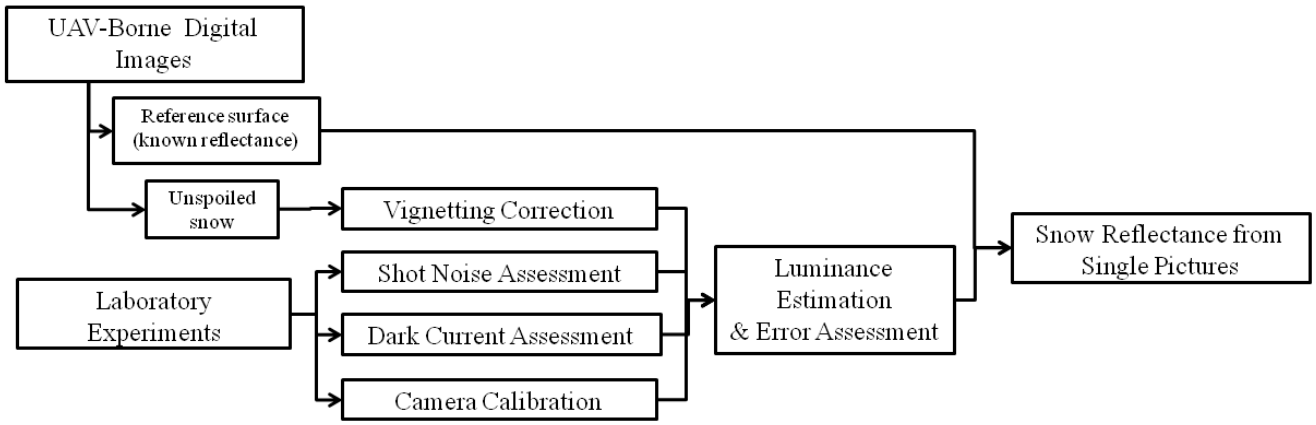

Figure 41: Schematic view of the snow reflectance estimation process from single picture.

7 Background

In this section, the technical terms and theories are introduced. In a first part, the vocabulary of light physics is defined. In a second one, the capabilities and limitations of the digital camera as scientific instrument to measure light are introduced. Eventually, the definition of snow reflectance and the way it can be determined using a digital camera is presented.

7.1 Photometric and Radiometric Quantities

In this report, the radiometric (radiation of all wavelengths) and photometric (radiation restricted to the visible light) quantities are defined as follows according to Tohsing et al. (2013):

- The radiant flux (or power) is the measure of the power of an electromagnetic signal and thus of the number of photons carried by that signal. It has unit $W = J/s$.
- Irradiance refers to the total amount of radiant flux (for all wavelengths) received from all directions by an elementary surface. Its unit reads W/m^2.
- The radiance is the radiant flux emitted, transmitted or received by a surface in a specific direction. Its unit is $W/m^2/sr$.
- The luminous flux (or power) quantifies the visible part of a radiant flux. The human eye spectral sensitivity has been defined for long in standards (CIE, 1932) and is described by the luminous efficiency function $\overline{y}(\lambda)$ (as seen in Figure 42). To convert radiant flux into luminous flux, the function $\overline{y}$ is applied to the spectrum of the radiant flux. The unit of the luminous flux is lumen lm.
- The illuminance is the equivalent of the irradiance for visible light. It is the total amount of luminous flux received by an elementary surface from all directions. Its unit is lux, $lx = lm/m^2$.
- The luminance is the equivalent of the radiance for the visible light. It quantifies the luminous flux travelling through an elementary surface in a particular direction. It reads candela per square meter as unit, $cd/m^2 = lm/sr/m^2 = lx/sr$.

7.2 Principles of Digital Photography

Using a digital camera as a scientific tool to measure optical properties requires an understanding of digital cameras and of what is actually captured in a digital image. In this section, the mechanisms of a digital camera are explained in a first part. Then its use as a light measurement device will be presented. Eventually, the sources of noise and the errors intrinsic to the digital camera are listed.

7.2.1 The Digital Camera Mechanics

As described in Figure 43, a camera is a device to impress light on a photosensitive film (analogical camera) or sensor (digital camera) that is located in the camera body. The amount of light that enters the body is controlled by three factors : the camera lens, the aperture and the shutter. The camera lens is a system of jointed optical lenses that control the field of view and the focus of the scene to be captured.

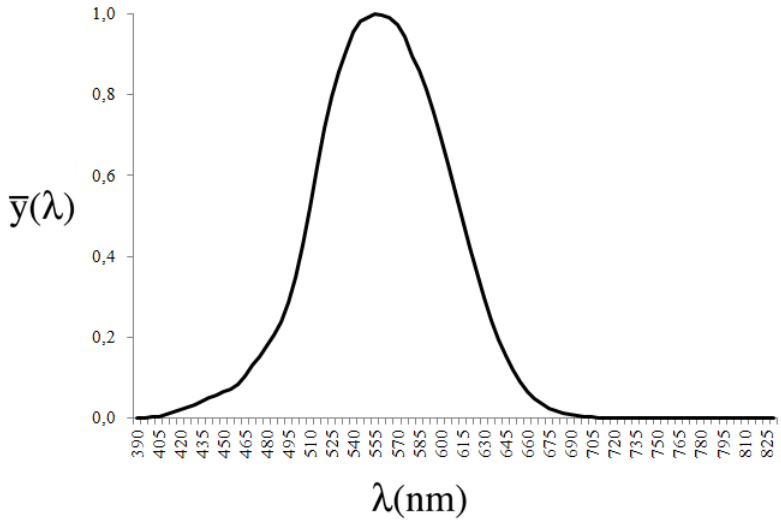

Figure 42: Luminous efficiency function as defined in CIE (1932). It describes how the human eye perceives a radiant flux depending on its wavelength. The sensitivity peeks in the green ($\lambda = 555nm$) and decreases toward blue and red wavelengths and eventually reaches zero outside of the visible.

- The focal length of the lens, expressed in millimetres, controls directly the field of view of the camera and indirectly the field of focus. The aperture is the diameter of the entrance pupil, a mechanical curtain in the lens that directly controls the amount of light and field of focus entering the body.

- The aperture is commonly expressed in relation to the focal length with the $f - number$, e.g. the dimensionless ratio between focal length and entrance pupil diameter. The amount of light entering the body is inversely proportional to the $f - number$.

- The shutter is the mechanical device that opens in order to let the light into the camera body. Commonly, digital cameras shutters are diaphragm type and consist in a series of blades that open a space for the light by rotating. The time that the shutter stays open determines the amount of light entering the body.

The digital imaging sensor consists of an array of photo-diodes, also called pixels, that produce an electric current when hit by the photons. But the photo-diodes react with little specificity to the wavelength so in order to create a color image, a so called Color Filter Array (CFA) has to be placed on top of the digital imaging sensor. The CFA, as seen in Figure 43, is an array containing three types of filters: 25% transmit only red wavelengths, 25 % blue wavelengths and 50 % green wavelengths (Figure 43). So each pixel on the sensor receives only one color and pixels belonging to the same color form a monochromatic image also called channel. The way the CFA (and some other filters inside the camera body) filters incoming light of different wavelengths is called spectral sensitivity of the camera. It is the relation between the optical input and the output current for each channel. The characteristic curves that describe the spectral sensitivity are specific to each camera model but their details are seldom released by the manufacturers.

The ISO sensitivity is an electronic amplification of the currents emitted by the sensor. ISO values commonly range from 100 up to 6400. Each time the ISO value is doubled, the amount of light needed to obtain the same picture exposure is divided by two. However, high ISO values are well known in photography to generate noise. Therefore keeping ISO as low as possible is a

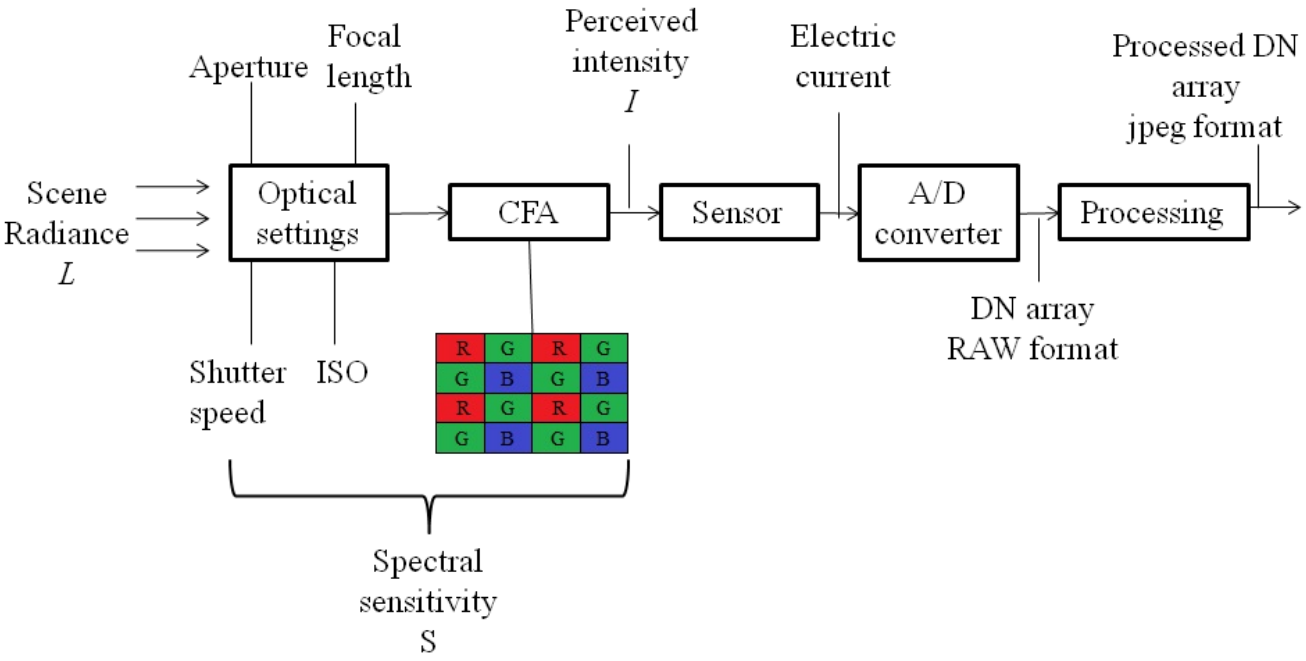

Figure 43: Schematic view of a digital camera.

must when using the camera as scientific instrument and, in the present study, the ISO is not considered a variable parameter.

Finally, an Analogic to Digital Converter converts the current generated by the photo-diodes into Digital Numbers (DN). The array of DN at this stage is called RAW image. Each pixel has a certain DN which is linked to the amount of light received and the wavelength it reacts to, according to CFA. From this stage further processing and compression of the image will lead to a compact image appealing to the eye using well known protocol such as JPEG format. But precious information is lost during that last step. Therefore all the present study was conducted with RAW images directly extracted from the sensor.

7.2.2 The Digital Camera as a Light Measurement Device

To use the digital camera as a light measurement tool, the optical and numerical chain presented in Figure 43 needs to be described thoroughly. Indeed one needs to know which part of the scene radiance will reach the sensor and how the sensor will transform the light input into Digital Numbers.

As explained in the previous paragraph, the amount of radiation that is let inside the camera is controlled by the camera settings and the CFA that filters the incoming light into the red, green and blue pixels according to the spectral sensitivity function. Thus, from a scene emitting a radiance of spectrum $L(\lambda)$ toward the camera, the sensor will actually perceive the intensity I presented in Figure 43 and defined as follows (Schwaebel et al., 2013):

$$I_k = n \int_0^{+\inf} L(\lambda) S_k(\lambda) d\lambda \tag{12}$$

Where k can be either R, G or B depending on the channel that is used, n defines the exposure settings used and is a function of focal length, aperture, shutter speed and ISO; and S_k is the spectral sensitivity of the channel k.

Then the intensity I_k perceived by each photo-diode of the sensor will be converted into DN and stored in the RAW image. This transformation can be assumed linear. Since the camera manufacturers do not disclose the spectral sensitivity function S of their camera, the experimental estimation of S as described in Sigernes et al. (2009) and the inversion of Eq. 12 would be required to determine the radiance of a scene from the DN of an image. However the complexity of such an experiment and of the following calculations, made it impossible in the time given to the present study.

An alternative approach is to consider that the red, green and blue channels together can describe the whole visible spectrum and thus quantify the luminance of the scene. In the human visual system, lights of different spectra are given different colors. These colors can be described as a combination of primary colours (ie. RGB system) or even better by their chromacity (absolute color) along with their luminance or brightness. The CIE (1932) xyY colour space describes any colour by its chromacity (x,y) and its luminance Y (Figure 44). In this standard is also describes how to calculate the CIE luminance Y from a linear RGB color space. As mentionned before, red, green and blue DN given by a digital camera can be assumed proportional to the input light in each wavelengths range. Therefore Roy et al. (1998); Wüller and Gabele (2007); Tohsing et al. (2013) used these relationships to extract the luminance from the DN in red, green and blue channels of a RAW digital image.

$$L = \frac{Y^{a_T}}{b_T E_v} \tag{13}$$

$$Y = 0.2125R + 0.7154G + 0.0721B \tag{14}$$

$$E_v = \frac{179}{200}\pi ISO\frac{T}{f^2} \tag{15}$$

Where L is the luminance for each pixel in cd/m^2, Y is the luminance as defined in CIE (1932) by a linear combination of R, G and B the DN of red, green and blue channels of a RAW digital image. E_v is the exposure coefficient depending on the ISO number, shutter time T and the f-number used for that picture and a_T and b_T parameters of the camera determined during the calibration process.

Therefore the luminance of an object can be determined from digital images. Nevertheless, the R, G and B values given by a digital camera still depend on the camera itself. Indeed, from the same scene, two cameras will not give the same red, green and blue counts and thus will not lead to the same luminance. The luminance Y is therefore relative to the camera. In the present study, since the reflectance of snow is determined relatively to a surface of known reflectance, it is not a problem to work with relative luminance. Another limitation is linked with the fact that the RGB color space, that is used by all digital cameras, cannot describe all existing colors, as explained on Figure 44. Therefore, nuances that can be perceived by the human eye will not be rendered properly on a digital image, mainly in the turquoise shades (Figure 44). But for the snow that has a white colour this limitation should not have a great impact.

7.2.3 Accuracy of Digital Images

Since the digital camera is used as a scientific measurement device, its accuracy needs to be assessed. Previous studies concerning snow reflectance from optical pictures only partially treated this issue. Here, it is presented a more extensive description of the sources of error known in image processing. In the Materials and Methods section there will then be presented the techniques used to correct and assess these errors. Most of the definitions bellow are taken from Berry and Burnell (2006).

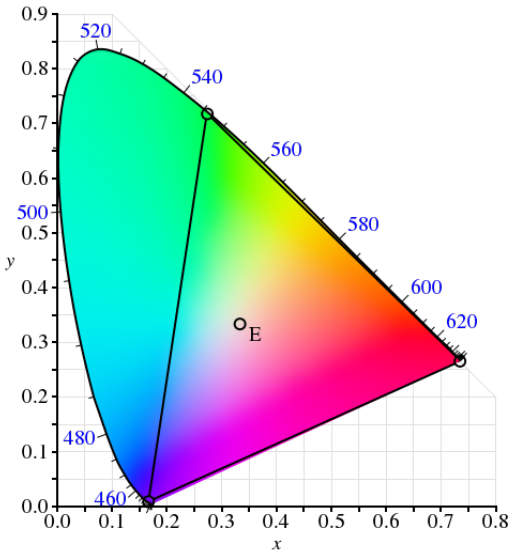

Figure 44: Chromaticities as defined in CIE (1932) containing all possible colors. The x-axis and y-axis are the x and y parameteres of the CIExyY color space. The upper edge of the color space labelled in blue with wavelength value represents all the monochromatic colours. The black triangle represent all the colours that can be described with a RGB colour space (all colours outside of this triangle might not be displayed accurately on a computer screen).

Vignetting The vignetting effect is the decrease of pixel intensity as they get further away from the center of the image. It is due to the properties of the lenses used by the camera. Indeed, the light that hit the objective with an angle has more chance to be absorbed or reflected before it reaches the sensor. As explained in the methods section, it is easily corrected following methods introduced by Hakala et al. (2010) and Lebourgeois et al. (2008).

Dark Current The dark current of digital camera sensors refers to the systematic generation of additional electrons by the photo-diodes, even when no light is hitting the sensor. The dark durrent is the superposition of a Fixed Pattern Noise (FPN) that will be the same from picture to picture, and a random noise that will change for each picture.

The FPN is due to degraded pixels in the silicon matrix that will always generate more electrons than other pixels. The location of these pixels may drift in time (Meza et al., 2010) and the number of additional electron they emit is a function of temperature and shutter speed.

The random noise is due to the random generation of electrons by the photo-diodes, attributable to impurities in the silicon matrix. Its intensity is proportional to temperature and shutter speed (Porter et al., 2008).

Shot Noise Light can be seen as a flux of photons travelling through the air and when the shutter of the camera opens and closes, a certain number of these light particles are let into the camera and will hit the sensor and be recorded in the digital image. But far from being a constant flux, photons arrive at a random pace to the camera. It means that even though photons are emitted by a stabilised, constant light source, pictures taken with the same settings will record sometimes more sometimes less photons than the expected flux. This noise, linked with the sampling of discrete particles flow, is called *Shot Noise* or *Photon Noise*.

Though this noise cannot be predicted due to the random behaviour of photons, it has been found that it respects the Poisson distribution. This property indicates that for N recorded photons, the standard deviation of the measurement will be $\sigma_{SN} = \sqrt{N}$. At first it can be

worrying that this noise is related to the signal level, ie. more light leads to more noise. But the Signal to Noise Ratio (SNR), defined as the ratio between signal level N and the standard deviation of the signal σ_{SN}, is thus equal to $\sqrt{N}$ and increases with N. In other words, increasing the amount of light entering the camera leads to higher noise level (σ_{SN}) but at the same this same noise is now smaller compared to the new signal level.

The difference between Shot Noise and random noise from the dark current can be assessed for a dark image taken in absence of light. In that situation Shot Noise is null while dark currant's random noise will still appear. However, according to Zhang et al. (2011), the Shot Noise is the most relevant source of noise in bright scenes such as snow covered areas.

7.3 Reflectance

Definition The reflectance has been given many different definitions in the literature. In this study, reflectance always refers to the Hemispherical-Directional Reflectance Factor (HDRF) as defined in Erhlich et al. (2012). The HDRF defines how a surface reflects all incoming radiation toward one specific reflection angle for a specific wavelength. In our case the incoming radiation is composed of the direct beam from the sun which has an incident angle defined by its zenith and azimuth (θ_0, ϕ_0), the diffuse radiation scattered by the sky and the position of the observer relative to the surface (θ', ϕ'):

$$HDRF(\theta_0, \phi_0, \theta', \phi', \lambda) = \pi\Omega \frac{dI_r(\theta_0, \phi_0, \theta', \phi', \lambda)}{dI_{glob}(\theta_0, \phi_0, \lambda)} = \frac{Radiance}{Irradiance} \tag{16}$$

Where Ω is the solid angle of reflection, dI_{glob} is the sum of direct (from a direction (θ_0, ϕ_0)) and diffuse incoming radiation and dI_r is the radiance of the reflected beam in direction (θ', ϕ'). Thus it can be seen that a snow patch the HDRF is defined as the ratio between radiance of the reflected beam and the irradiance of the snow patch for a specific wavelength λ. If the sun position and the direct to diffuse radiation ratio are known it is possible to split the irradiance into direct and diffuse components and thus to get back to the Bidirectional Reflectance Distribution Function (BRDF) as given by Warren (1982).

As mentioned in the previous section, a digital camera is used to determine the luminance, i.e. the visible part of the radiant flux, and not the radiance. Thus it is possible to calculate the spectrally integrated visible HDRF, i.e. $\overline{HDRF}_{vis}$, using Equation 17 and the luminous efficiency function $\overline{y}(\lambda)$ (presented in Figure 42) :

$$\overline{HDRF}_{vis}(\theta_0, \phi_0, \theta', \phi') = \pi\Omega \frac{\int_{380}^{780} \overline{y}(\lambda) dI_r(\theta_0, \phi_0, \theta', \phi', \lambda)}{\int_{380}^{780} \overline{y}(\lambda) dI_{glob}(\theta_0, \phi_0, \lambda)} \tag{17}$$

Where $\overline{y}(\lambda)dI_r(\theta 0, \phi_0, \theta', \phi')$ is the visible part of the reflected beam radiance (ie. luminance) and $\overline{y}(\lambda)dI_{glob}(\theta_0, \phi_0, \lambda)$ the visible part of the irradiance (ie. illuminance).

Therefore, it is possible to estimate the $\overline{HDRF}_{vis}$ by measuring the luminance of a surface, $L(\theta_0, \phi_0, \theta', \phi')$, and the illuminance of a scene, $Il(\theta_0, \phi_0)$:

$$\overline{HDRF}_{vis}(\theta_0, \phi_0, \theta', \phi') = \pi\Omega \frac{L(\theta_0, \phi_0, \theta', \phi')}{Il(\theta_0, \phi_0)} \tag{18}$$

Equation 18 is the foundation of the method presented in this study. The reflectance is calculated as a function of the scene luminance and illuminance. It has been seen that the luminance can be inferred from the digital images using Equations 13, 14 and 15. But the illuminance is still to be determined. And this will be done using a so called Lambertian surface.

Lambertian surface A Lambertian surface has the characteristic, unlike snow, to diffuse evenly the incoming radiation in all directions. Therefore its reflectance does not depend on the sun position nor on the viewing angle. Also, if its reflectance is known, the Equation 18 can be used to determine its illuminance from its luminance. This property will be used later to estimate the illuminance of the snow patch of which reflectance is to be determined.

8 Materials and Methods

Estimating snow reflectance from optical pictures is a two step process. The first step is a series of laboratory experiments to calibrate the camera in order to assess its accuracy. The second step is the data acquisition in the field and data processing. It is reported that these two steps are independent from each other, meaning that the fieldwork can be carried out with a non-calibrated camera without affecting the data acquisition results.

8.1 Camera Set-Up

The camera set-up involves the errors assessment and the camera calibration. As mentioned in the Background section, camera calibration in particular can be an obstacle not easy to overcome. The present study also aims to propose a series of relevant experiments that do not require high expertise nor expensive materials from the user.

8.1.1 Errors Assessment

The errors assessment consists in correcting the bias introduced by vignetting and in estimating the various sources of noise in the pictures.

Vignetting Estimation The vignetting correction was done following the method of Hakala et al. (2010) and Lebourgeois et al. (2008). During the snow mapping campaign conducted by Emiliano Cimoli, 500 pictures of snowy surfaces were taken from the UAV from different angles and with different light conditions. By averaging all those pictures, the effect of light conditions, slope or small features such as sastrugis could be removed. The result is a white uniform image where the reduction in the intensity of the pixels as they are further from the sensor which can be related to the vignetting only. The white image was then divided by its maximal pixel value to get a standardized image ranging from 0 to 1. This image is expected to have values close to one in the center of the image and decreasing values as the pixels are located further away from the center. Then a polynomial was fitted to each channel of the white image to remove the effect of noise. This polynomial gave a value to each pixel and reads as follows:

$$P_k(i,j) = ar^2 + br + c + di + ej \tag{19}$$

Where P_k is the correction polynomial for the channel $k \in [R, G, B]$ for the pixel (i, j) distant of r from the center of the image and a, b, c, d, e are fitted coefficients. The terms di and ej are added to account for the possibility that the optical center of the image (determined by the alignment of the lenses) do not hit the actual center of the sensor. Then this polynomial was applied on any new image to correct the intensity of each pixel to its original level and thereby correct vignetting.

Dark Current estimation The FPN and the random noise related to the dark current can be detected by taking pictures in absence of light, i.e. taken in a dark environment and the lens laid is left on. These dark pictures, called Dark Frames will show a constant FPN superposed with a random noise as seen in Figure 45. To estimate the FPN, the Dark Frames can be averaged into a Master Dark Frame. Due to its randomness, the magnitude of the random noise in the Master Dark Frame will be reduced as seen in Figure 45 and the FPN will appear more clearly. In other words, the Master Dark Frame is an estimated map of the Fixed Pattern Noise. Then, once the FPN calculated, the random noise can be quantified (but not removed) by observing how much the single Dark Frames vary from the Master Dark Frame.

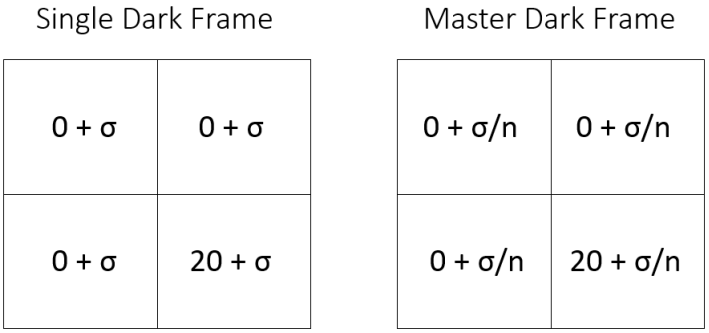

Figure 45: In a dark frame the real value of digital numbers in each pixels is equal to zero. However, Fixed Pattern Noise will be added random noise σ and increase the DN of the dark frame with a magnitude dependent on the shutter speed and sensor temperature. By averaging n dark frames into a master dark frame, the random noise is reduced by $1/n$ due to its random pattern, making more clear the FPN (that gives for example a DN of 20 to the lower right pixel). FPN can then be removed from a single picture by subtracting the master dark frame from it.

Usually it is recommended to estimate the Master Dark Frame before and after a picture is shot so that the FPN can be removed from the resulting image. However this was not done at the time of the UAV campaign. Since the Fixed Pattern itself may change over long time scales (Meza et al., 2010), the dark current could not be corrected a posteriori. However, an estimation of the magnitude of the dark current was studied four month after the fieldwork to evaluate how much it might affect the images from the field campaign. The FPN and random noise were estimated at different shutter speeds and at the temperatures of -20°C and 20°C. For each shutter speed, 4 Dark Frames are taken. The random noise magnitude is evaluated as the standard deviation of the digital numbers over the single Dark Frames. The FPN magnitude is estimated as the maximum value of digital numbers in the Master Dark Frame.

Shot noise The shot noise is the part of the noise that can be related to the mean number of photon entering the camera.

In a black room, the camera was installed in front of three screens that were illuminated by a white light source constant in time. Pictures were taken of the same scene for 58 different settings and were corrected for vignetting. In every picture, 45 samples of 5x5 pixels were selected at fixed location in the image (Figure 46). Due to their small size each sample is assumed to be a surface of homogeneous color, i.e. the pixels within each sample should all have the same DN in red, green and blue channels. Because of the noise these DN will deviate from their ideal value and while the mean DN for the sample is an estimate of the real DN, the standard deviation of the pixels within each sample quantifies the noise. This observed noise is the superposition of differences sources, the Shot Noise is one of them but other sources, not explicated in the present analysis, might also affect the overall noise level. Determining the participation of the Shot Noise is the aim of this experiment.

By plotting sample standard deviation as a function of sample mean for all samples and all camera settings, it can be assessed if the Shot Noise plays an important role. Indeed, if noise magnitude (i.e. sample standard deviation) shows a dependence to the square root of the sample mean, it can be concluded that Shot noise is the dominant source of noise.

8.1.2 Camera Calibration

The purpose of the camera calibration is to relate the DN value of a pixel to the luminance of the object present in the picture. Equations 13, 14 and 15 describe this relationship and the two

coefficients a_T and b_T are to be found experimentally. This calibration method uses a constant light input and varies the settings of the camera in the same way as Dymond and Trotter (1997).

The experimental set-up is the same as explained for the shot noise assessment (Figure 46): 45 samples of 5x5 pixels were selected at fixed locations in 58 images of the same scene taken with different exposure (by changing shutter time or aperture). The ISO was set to 100 and the light conditions were constant. Averaging the DN of the sample allowed to reduce the effect of noise and Y was calculated for the mean red, green and blue counts in each sample.

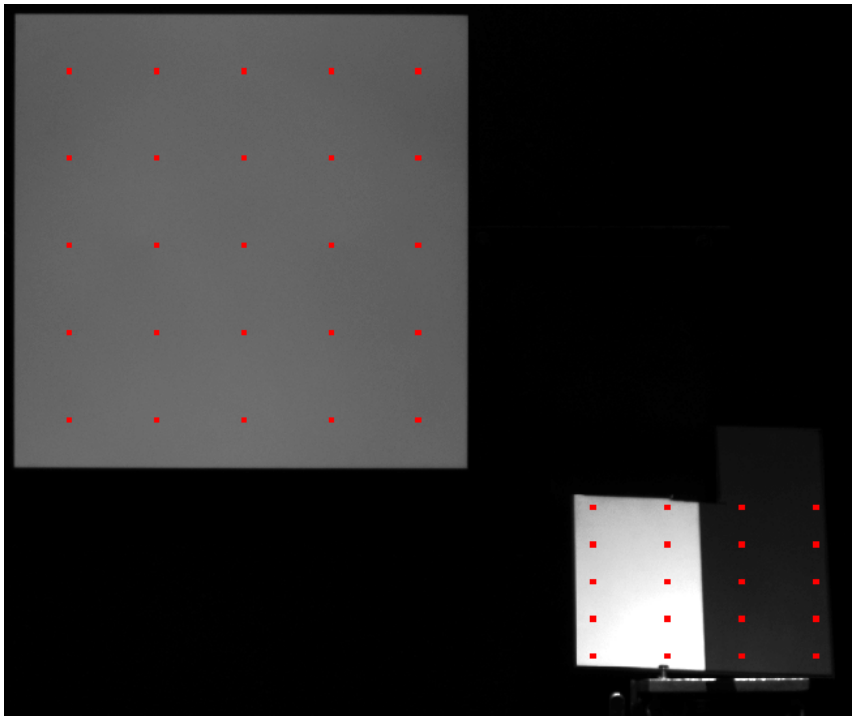

Figure 46: Experimental setting for the calibration of the camera and the evaluation of the shot noise. Each red square is a sample composed of 5x5 pixels. It can be seen that the different samples are under different illumination depending on their location. Therefore, by changing the camera settings and keeping the illumination constant throughout the experiment, the calibration can be constructed on several values of constant illumination.

For two pictures that are taken from the same scene but with different settings, the luminance L_1 of a sample in image 1 should be equal to the luminance L_2 of the same sample in image 2. And applying equation 13 it leads to:

$$\frac{Y^{a_T}}{b_T E_{v1}} = \frac{Y^{a_T}}{b_T E_{v2}} \tag{20}$$

And by replacing E_v by its definition in equation 15 it leads to the following equation:

$$(\frac{Y_1}{Y_2})^{a_T} = \frac{T_1}{f_1^2}\frac{f_2^2}{T_2} \tag{21}$$

Where $\frac{Y_1}{Y_2}$ can be calculated from equation 14 applied on the RGB counts of the two pixels and $\frac{T_1}{f_1^2}\frac{f_2^2}{T_2}$ are the settings used for the two pictures.

Eventually, for every possible pair of images and for each sample, $\frac{T_1}{f_1^2}\frac{f_2^2}{T_2}$ and $\frac{Y_1}{Y_2}$ were reported on a graph in order to determine the coefficient a_t.

This calibration method does not determine the b_T and therefore do not need the absolute measurement of the sample luminance. It only relates the relative increase in brightness $\frac{Y_1}{Y_2}$ with

the relative increase in exposure. Since the snow reflectance, as explained further, is determined relatively to a reference surface of known reflectance, this calibration method is enough and b_t is not needed.

8.2 Fieldwork Campaign and Data Processing

The goal of the calibration was to link DN to luminance in order to determine reflectance in aerial pictures of snow taken by a digital camera mounted on a UAV. In this section is presented how these pictures were acquired and how they are used to determine snow reflectance.

8.2.1 Study Site

The snow reflectance survey took place in the Tasersuaq area (67°10′45.90”N 53°14′18.26”W), Sisimiut county, West Greenland on April 26, 2015. It was chosen because located within the hydro-power basin from which Sisimiut takes its electricity and because Emiliano Cimoli's project had interest in mapping the snow there. The area consists in a gentle slope facing NW on the orographic left side of a valley. Heavy snowfall took place few days before the field campaign and the low temperatures in the next days preserved the snow from melting. Exposed to winds blowing through the valley, the day of the survey the snow was uneven with many surface patterns as sastrugi and deposition-erosion structures due to snow drift. The experiment took place around 11:40 AM. The solar zenith angle, e.g. the angle between the sun and the horizon, was 56°. The area where the pictures were taken was levelled so no correction for slope was made on solar zenith angle.

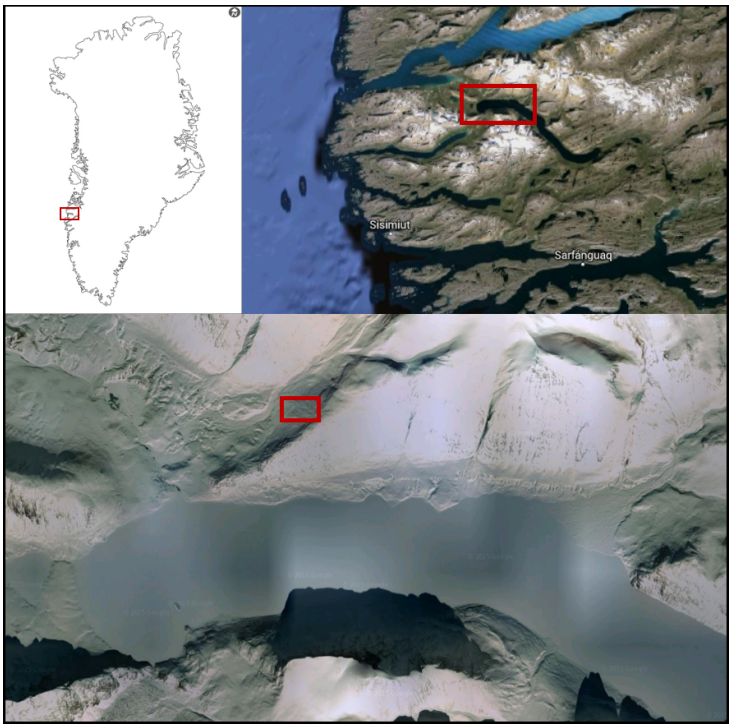

Figure 47: Location of the fieldwork area.

8.2.2 Fieldwork Plan

The experiment, similar to the one proposed by (Hakala et al., 2010), was conducted as follows:

- A homogeneous and unspoiled snow surface was selected. Lambertian surfaces (Labsphere's Spectralon SRT-SP-100) of reflectance 10% and 90% for visible light are laid in the snow (Figure 49).
- The snow spectral reflectance is measured with the ASD FieldSpec 4 spectrometer relatively to the 90% reflective Lambertian surface.
- The UAV, equipped with the digital camera taking pictures every second, is flown vertically above the area of interest up to 8 meters . It was made sure that the reference Lambertian surfaces appeared in most of the pictures.
- After the flight, the relative spectral reflectance of the snow patch is measured again, to prevent eventual changes in the light conditions.

8.2.3 Equipment List

The fieldwork plan described above requires the three instruments that will be further described in this section: the spectrometer, the digital camera and the UAV.

ASD FiledSpec 4 Spectroradiometer A spectroradiometer, also called spectrometer, measures the spectral power distribution of a radiation source, i.e. the power that is emitted by the source for each wavelength. For the ASD FiledSpec 4 and as seen in Figure 48, a pistol, that acquire light from the source of interest, is connected by optical fibre to the FieldSpec where light is analysed. A Dell Latitude laptop remotely connected with the Fieldspec allows real-time control and visualization of the data acquisition.

Figure 48: The ASD FiledSpec 4 Spectroradiometer in use.

In the FieldSpec body the incoming electromagnetic signal is separated into its monochromatic beams (in the same way as done by a prism) by a film called holographic diffraction grating. The beams are then sent to the sensor, a silicon photo-diode array, which converts linearly the monochromatic beam's intensity into a current. The geometry of the system is defined such as each column of photo-diode will receive a beam of different wavelength. This allows a spectral resolution of 3 nm at 700 nm. Having several photo-diodes receiving the same monochromatic beam (the ones placed in the same column) allows to reduce noise. Also the

spectral sensitivity of photo-diodes define the spectral range of the FieldSpec. In the present case, it can record radiation of the visible and near infra-red domains (390 to 1050 nm). The current is then converted to digital number by the analogical to digital converter and the data is transferred to the laptop.

In the present study it was chosen to gather relative reflectance data in order to obtain directly the reflectance ratio between the sample and the Lambertian surface. Each measurement was conducted as follows:

- The spectrometer has to be optimized, using the automatic procedure *optimization*. This adjusts the instrument settings in relation to light conditions and time of data acquisition.
- In the same way as for digital cameras, the dark current of the spectrometer sensor has to be removed. It was done by recording the sensor activity when covering the pistol. It was then removed automatically from the following measurement.
- The spectral intensity of the 90% reflective Lambertian surface is measured and stored by the laptop as reference.
- The surface of interest can be measured and its spectral power is divided by the one of the reference surface. The data is then given as relative reflectance with respect to the reference.

UAV The UAV used in the present study is the commercial hexacopter DJI S900. The choice of the drone was limited by the funding. The present study does not aim at testing the UAV itself. Further assessment of the pros and cons of different UAV models should be conducted. The present plateform offered a payload of 5 kg allowing to carry the DSLR camera. The autonomy in flight with the camera was around 6 min for one 5400 mah battery, less time was used for the present survey.

Camera In the present study, the camera used is the Digital Single Lens Reflex (DSLR) Nikon D3200 with a Nikkor 18-55 mm f 3.5 lens mounted. The SLR technology is a system of image pointing that involves a mirror and a prism to allow the photographer to exactly see the size of the picture that will appear on the sensor. Shutter speed was set to 1/800 s to avoid blurry pictures, ISO to 100 to reduce noise, focal length to 18 mm to maximize field of view and aperture to f-18 to ensure proper exposure of the pictures.

8.2.4 Data Processing

Once the pictures acquired and the camera calibrated, the snow reflectance could be estimated from single pictures. Then different overlapping pictures were investigated to analyse the repeatability of the method.

Snow reflectance from Single Pictures The pictures are selected so that the reference Lambertian surface and the snow patch of interest appear in the picture. The selected RAW images are converted to `.dng`, a format that allows to process RAW images, and uploaded in Matlab and corrected for vignetting before further calculations.

As explained in Equation 18, the reflectance of a surface is calculated from its observed luminance and from its illuminance. The observed luminance can be calculated from the average DN in the snow patch of interest and Equation 13. To calculate the illuminance, the Lambertian surface is necessary. Indeed, by assuming that the illumination is homogeneous in the picture, the amount of light received by the Lambertian surface and by the snow patch of interest can

be considered equal. In other words the illuminance of the reference Lambertian surface Il_{ref} is equal to the illuminance of the snow patch of interest Il_{snow}. If put in relation to Equation 18 it gives:

$$\pi\Omega_{snow}\frac{L_{snow}(\theta_0,\phi_0,\theta',\phi')}{\overline{HDRF}_{vis,snow}(\theta_0,\phi_0,\theta',\phi')} = \pi\Omega_{ref}\frac{L_{ref}}{\overline{HDRF}_{vis,ref}} \tag{22}$$

Where the reflectance $\overline{HDRF}_{vis,ref}$ of the reference Lambertian surface is known and independent from sun and viewing angle. Ω_{snow} Ω_{ref} are the solid angle for which the luminance is measured. They are thus related to the footprint of the pixel in the image. Since the reference and snow surfaces are located close to each other the pixel footprint on the snow patch can be assumed equal to the pixel footprint on the Lambertian surface. Therefore it is assumed $\Omega_{snow} = \Omega_{ref}$. The validity of these assumptions will be discussed later on. Therefore, Equation 22 allow under these conditions a direct estimation of the snow patch reflectance as a function of the snow patch luminance, the Lambertian surface known reflectance and luminance:

$$\overline{HDRF}_{vis,snow}(\theta_0,\phi_0,\theta',\phi',\lambda) = \overline{HDRF}_{vis,ref}\frac{L_{snow}(\theta_0,\phi_0,\theta',\phi')}{L_{ref}} \tag{23}$$

The luminance is estimated from the digital number of each channel accordingly to Equations 13, 14 and 15. In these equations, the exposure E_v (depending on camera settings so constant within a single picture) is the same for both Lambertian surface and snow patch of interest and a_T and b_T are depend on the camera. Therefore, Equations 13, 14, 15 and 23 lead to:

$$\overline{HDRF}_{vis,snow} = \overline{HDRF}_{vis,ref}\left[\frac{Y_{snow}}{Y_{ref}}\right]^{a_T} \tag{24}$$

Where the luminance Y is calculated as linear combination of the DN value in red, green and blue channels of the raw picture (Equation 14). In theory, the Equation 24 is valid for any single pixel within the picture but in practice, random noise will be added to the DN value which makes the estimation of reflectance from a single pixel unreliable. This is addressed by selecting all the pixels from the area of interest (snow or Lambertian surface) and by calculating the mean DN in each color channel as shown in Figure 49.

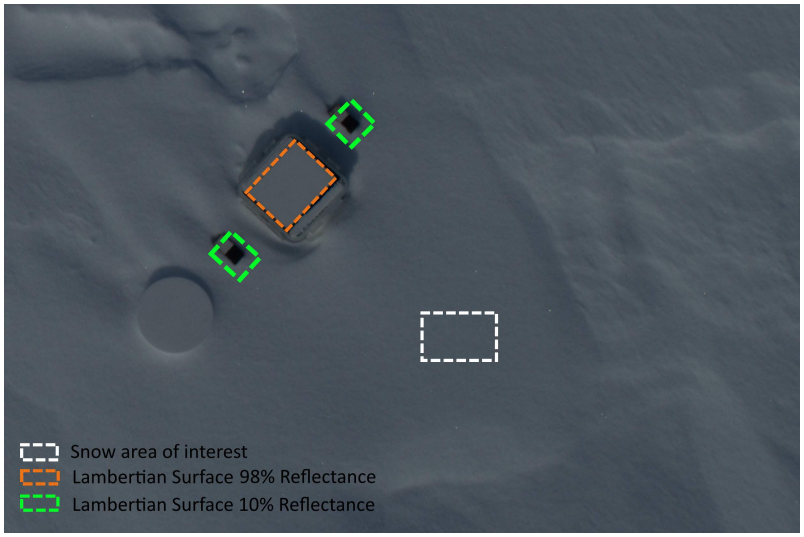

Figure 49: Areas of interest selected to investigate the calculate the snow reflectance from a single picture frame.

Though minimized by taking in the area of interest the mean DN value for each channel, the noise introduce uncertainty in the red, green and blue mean DN values. This uncertainty is given by the standard deviation σ of the red, green and blue DN values within the area of interest. It then propagates to uncertainty on the luminance and reflectance estimation (also given by their standard deviation σ) that are calculated according to the following equations:

$$\sigma_Y = \sqrt{(r\sigma_R)^2 + (g\sigma_G)^2 + (b\sigma_B)^2} \tag{25}$$

Where σ_Y is the uncertainty on luminance estimation, r, g and b are the coefficients in equation 14, and σ_k with $k \in [R, G, B]$ is the standard deviation of the DN values in the area of interest (snow patch or reference Lambertian surface).

$$\sigma_R = \sqrt{\left(\frac{\sigma_{Y_{ref}}}{Y_{ref}}\right)^2 + \left(\frac{\sigma_{Y_{snow}}}{Y_{snow}}\right)^2} \tag{26}$$

Where σ_R is the uncertainty on the reflectance estimation, Y_{ref} and Y_{snow} are the estimated luminance of the reference Lambertian surface and snow patch respectively and $\sigma_{Y_{ref}}$ and $\sigma_{Y_{snow}}$ their respective uncertainty.

For validation, the reflectance of a 10% reflective Lambertian surface present in all pictures was also estimated using the same method and the uncertainty of the estimation is reported. In absence of validation measurement for the snow reflectance from the spectrometer, it allows to compare the estimated reflectance with the known reflectance of the Lambertian surface.

Variability of Luminance Estimation in Overlapping Pictures The estimation of snow reflectance presented until here, just as the one of Hakala et al. (2010), involves a major limitation: a Lambertian surface of known reflectance has to be present in each picture. This is simply not possible if this method aims at mapping snow characteristics over large and/or complex area. The question that is then asked is: can the reference surface present on one picture be used to estimate sow reflectance in other pictures where the reference is not visible? This depends on various factors.

First if the light conditions are variable, the presence of the reference surface in the picture is necessary. Indeed, if the cloud covers the sun while the UAV is surveying an area without reference surface, the snow will then appear darker and it will be impossible to assess whether it is due to a difference in reflectance or to a reduction of incoming light. But in certain conditions such as cloud-free sky or slow-moving clouds, the light condition can be assumed constant or varying slowly. In that situation, the reference surface could be observed at the beginning and at the end of the flight and its luminance (or an interpolation between the observation made at the beginning and at the end of the survey) could be used to calculate snow reflectance in pictures where the reference is not visible.

Second, the stability of the camera mechanics and electronics is of great importance to extrapolate the observation of the luminance of the reference surface from one picture to another. Indeed, the components that control the opening and closure of the shutter or the diameter of the entrance pupil always present a certain level of precision. If these components are not precise enough, two pictures (one with the reference surface, the other without) would be taken with slightly different exposures even though the user settings are the same. In that case the picture without the reference surface could appear brighter/darker than the one with the reference surface. And it would be difficult to know whether it is due to a change in the snow reflectance or to a greater/lesser exposure than the one specified by the settings.
This variability from picture to picture can be assessed from the data acquired during the field work. Indeed by comparing the observed luminance of the reference Lambertian surface in the

different pictures where it appears it can be assessed if its value changes in a great extend. In order to reduce the effect of the number of pixels that represent the reference surface and also to reduce computational cost, a fixed number of 50 pixels, randomly selected within the Lambertian surface, was used for the luminance calculation. The Lambertian surface is the ideal target for this experiment since its reflectance is not expected to vary with the camera position if the light conditions are constant.

9 Results and Discussion

In the first part of this section, the results of the camera preparation and noise assessment are presented. The second one explains and discusses the result of the fieldwork and the estimation of snow reflectance.

9.1 Camera Set-Up

9.1.1 Vignetting Correction

After computing the white image by averaging 500 pictures of snow that were taken from different view angles, the Equation 19 was fitted to each channel of the white image. The polynomial from Equation 19 was then fitted to the the white image. Table 14 gives the resulting coefficients of Equation 19 for the three channels.

	a	b	c	d	e
Red channel	-4.9e-07	-5.2e-08	-4.5e-06	1.9e-05	0.96
Green channel	7.4e-06	-5.0e-08	-3.7e-06	1.6e-05	0.96
Blue channel	4.4e-07	-4.1e-08	-3.0e-06	1.3e-05	0.96

Table 14: Coefficients of the polynomial presented in Equation 19 after fitting to the white image for vignetting correction.

Equation 19 was then used to calculate the standardized correction of which contour plot is shown in Figure 50. As expected, the pixels in center of the image have a value close to one while the intensity of the pixels in the corners have down to 78% the intensity of the ones of the center. This finding is in agreement with the result ofHakala et al. (2010). It can also be observed that the center of the vignetting pattern is not located exactly in the center of the picture but shifted to the right indicating a small shift of the sensor from the optical axis of the camera. All images are then corrected from vignetting by dividing each channel by the related correction image and thereby rising the corner pixels to their normal intensity.

9.1.2 Dark Current Estimation

The dark current is divided into Fixed Pattern Noise and random noise that are both detected by taking four dark frames and by analysing the mean value and standard deviation for each pixel over the four frames.

Fixed Pattern Noise: The FPN is pixel dependant and constant from picture to picture. Thus the master dark frame, as the average of the single dark frame is an estimation of the FPN. Master dark frames were calculated for +20°C and 20°C and for various shutter speeds. Figure 52 shows the dark frame calculated at -20°C and for 1/800s shutter time. The amplitude of the FPN, i.e. its maximum value, appeared to be dependant on the channel, shutter speed and temperature.

At low temperature (-20^oC), the FPN has a magnitude of 10 DN independently on the color channel and shutter time. At room temperature (20^oC) the magnitude of the FPN in the blue channel increases up to 46 DN for shutter times greater than $1/5s$, as shown in Figure 51. The green channel, in the same conditions, shows an FPN of which magnitude goes from 10 DN for short exposure up to 20 DN for long shutter time. The FPN of the red channel however, is not sensitive to the changes in temperature and shutter speed and remains of lower than 10

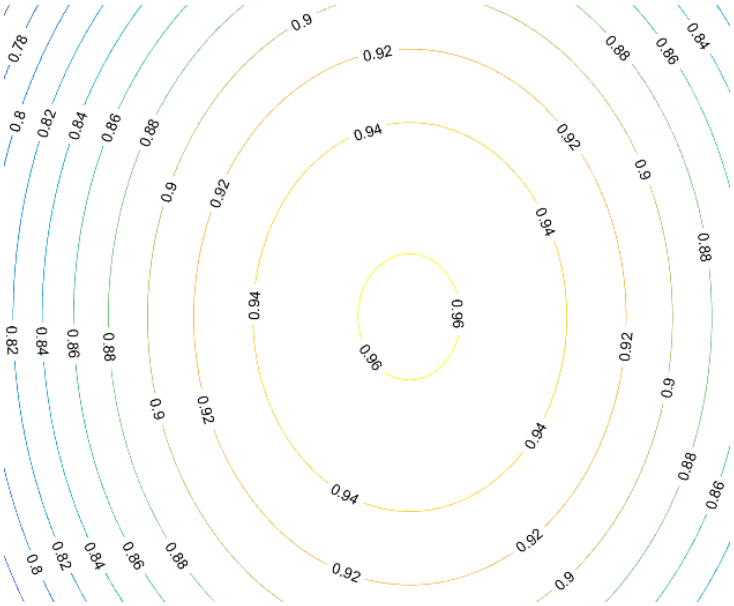

Figure 50: Contour plot of the vignetting correction image for the red channel. It shows, for an homogeneous light input how the intensity of the pixels decrease as they are located further from the center of the image. This decrease is present in every pictures. To be corrected from vignetting, each channel of an image has to be divided by the appropriate channel of the correction image. The shift toward the right indicates that the alignment between lens and sensor is not perfect.

DN. In all channels and for all conditions, pixels significantly affected by PN were found to be relatively scarce (as can be seen in Figure 52).

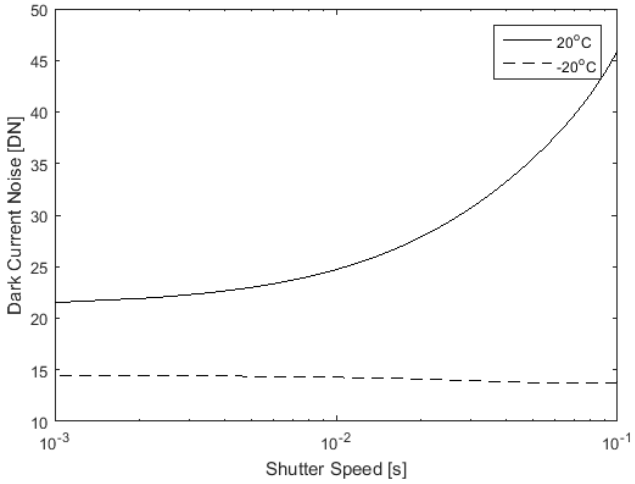

Figure 51: FPN for the blue channel. It can be observed that for high temperatures the noise increases with the shutter speed. The curves are 3^{rd} degree polynomial fitted to the data for clarity of representation.

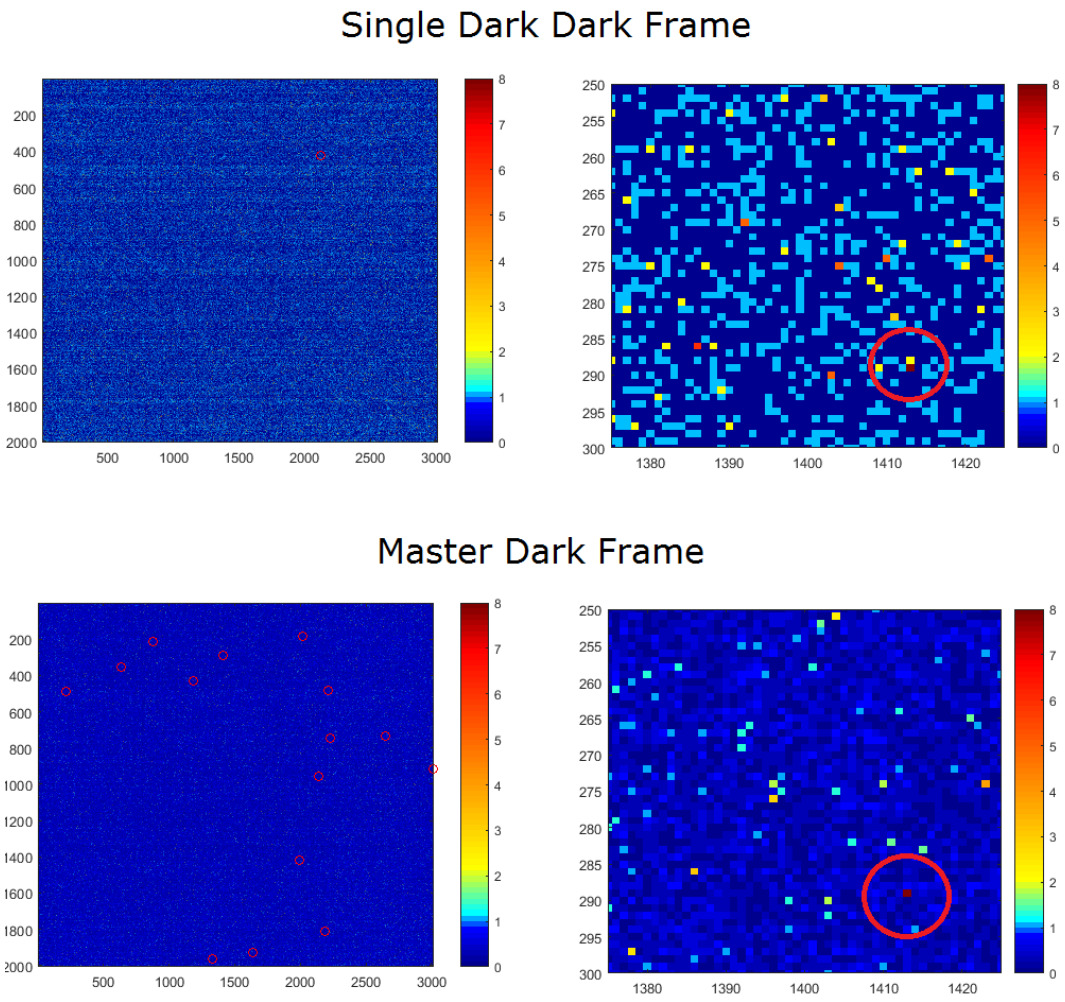

Figure 52: Single and master dark frames (full frame on the left, zoomed to the red area on the right) in the red channel for shutter speed equal to $1/800s$ and temperature equal to -20^oC, i.e. the fieldwork operational conditions. It shows the superposition of dark current's FPN and random noise. By averaging single dark frames, the random noise can be reduced and the FPN highlighted. The red pixel on the right hand side appeared to belong to the FPN because it showed a higher DN in all dark frames. The pixels highlighted in the master dark frame belong to FPN.

It is usually recommended to estimate and remove the FPN by acquiring a master dark frame before and after pictures are taken and by removing it from the pictures. In the present study, on site estimation of the FPN was not conducted. And since the FPN can change over months, no correction a posteriori could be done. Nevertheless, the presented assessment of the FPN, conducted four months after the field work, can be used to estimate the magnitude of the uncorrected FPN in the pictures used later for snow reflectance estimation. Considering the conditions of the snow reflectance exeriment (low shutter time of 1/800 s and air temperature of -10^oC) it can be concluded that the uncorrected fixed pattern noise cannot exceed 15 DN per pixel for all the color channels. Additionally, the scarceness of the pixels affected by FPN reduces its actual impact on the pictures. Indeed, since snow reflectance estimation is conducted on many neighbouring pixels, only few of them are potentially biased due to FPN. Therefore the FPN is not considered as an import source of error in the estimation of snow reflectance.

However, if the reflectance estimation is done using few pixels such as Hakala et al. (2010), "hot pixels" affected by FPN can create a significant bias in the result. Also, at higher temper-

atures and shutter speeds, the FPN can be considered as a main source of error and should be removed as suggested.

Random Noise The dark current random noise is visible in dark frames as the random deviation from the FPN. In the present study, it is given by the standard deviation of pixels over four dark frames. Sine the standard deviation of each pixel rarely surpass 1 DN it indicates a dark current random noise no higher than 4 or 5 DN per pixel which can be neglected compared to other sources of error such as Shot Noise. This is in agreement with Porter et al. (2008) that also described a small random noise for the tested settings. He reported however, that for much longer exposures (not used in the present study) random noise can increase significantly.

9.1.3 Shot Noise Estimation

The Shot Noise, unlike the dark current, is only present when light enters the camera. Using the experimental setting presented in the method section, pictures of three illuminated screens were taken with different exposure. Samples of 5x5 pixels are selected in fixed locations in the pictures. In a picture, the standard deviation of the pixels that compose a sample is an indicator of how noisy the picture is. To differentiate the shot noise from the other noise sources it is considered as the noise of which amplitude is proportional to the square root of the sample mean. This could be assessed by plotting sample standard deviation as function of sample mean for all samples and all camera settings. Figure 53 displays an example of shot noise modelling for the green channel while Table 15 show the coefficients and R^2 values for the other channels.

Table 15: Coefficient and R^2 of the shot noise error estimation

	a	R^2
Red channel	0.45	0.87
Green channel	0.45	0.86
Blue channel	0.46	0.88

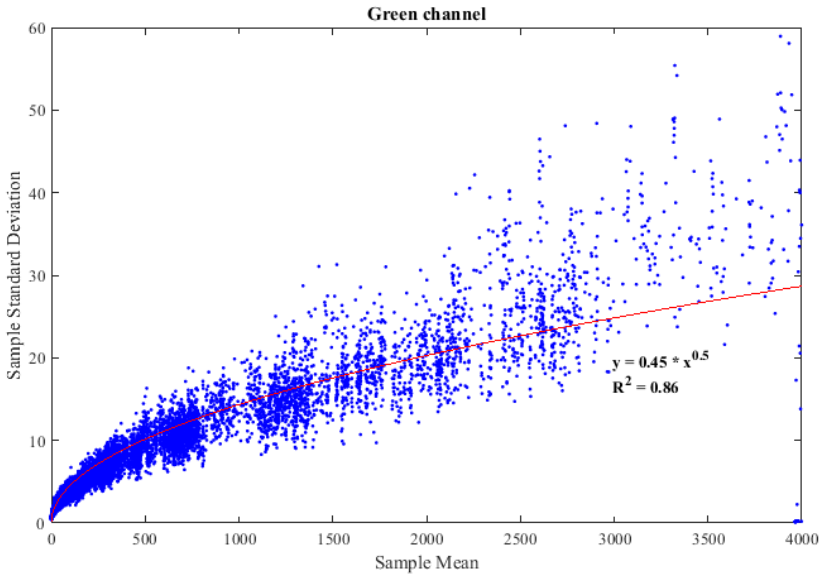

Figure 53: Shot noise modelling using a square root fit (red line) between the within-sample standard deviation (blue dots) and the sample mean. The equation and R^2 of the fit is given;

From Figure 53 it can be seen that for mean DN less than 1500, the shot noise explains quite well the samples standard deviation. For sample mean greater than 1500 DN, the standard deviation deviates from the regression line (Figure 53), meaning that another source of noise, not dependant on the square root of mean DN, plays an important role. Same conclusion are inferred from similar plots in the blue and red channels. Additionally it should be noted that the pictures of snow that are used for snow reflectance estimation have very low exposure (to avoid blurry pictures from the moving UAV). And the DN in these pictures do not exceed 200 DN. Since this evel of intensity is lower than the 1500 DN mentionned earlier, it can be assumed that the shot noise will be a good estimation of the noise that applies on that pixel. By using the fitted curves of which characteristics are reported in Table 15 the deviation deviation caused by noise can be estimated = by $\sigma = 0.45\sqrt{DN}$. For the snow pictures it means that no more than a deviation of 6 DN from the expected value can be expected.

9.1.4 Camera Calibration

The camera is calibrated as explained in the methods section. Pictures of a scene were taken with various camera settings and for constant illumination. Samples of 5x5 pixels were selected in fixed locations and the sample CIE luminance Y was calculated from Equation 14 using sample's mean DN in red, green and blue channels. Also the exposure E_v for each pictures was calculated from Equation 15. Considering 45 samples and 58 camera settings it gave 2610 luminance values for the calibration. For each pair of luminance, the increase in exposure $\frac{E_v 1}{E_v 2}$ was plotted as a function of the increase of luminance $\frac{Y_1}{Y_2}$ in order to determine the a_T coefficient of Equation 21. The plot is displayed in Figure 54.

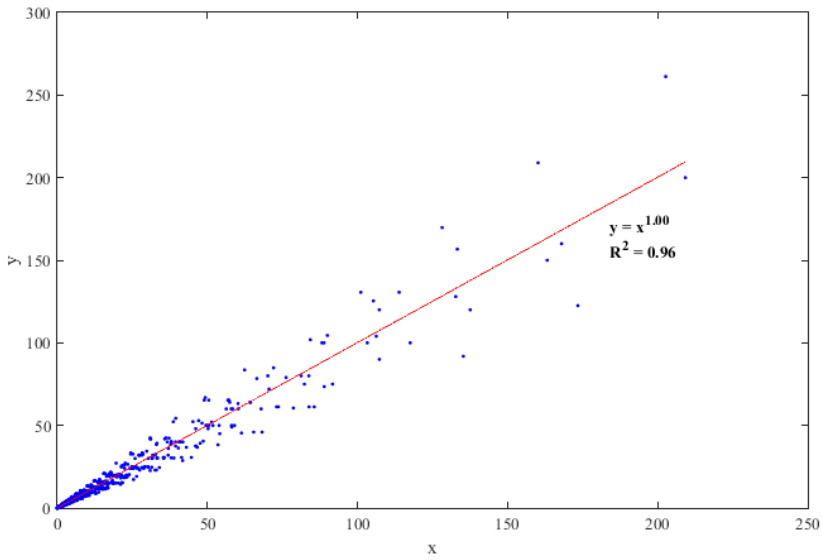

Figure 54: Plot resulting from the calibration of the camera. The increase in exposure between two samples is plotted as function of the increase in luminance and fitted according to Equation 21.

As displayed in Figure 54, the coefficient a_T is very close to one. It indicates that the luminance indicator Y inferred from the red, green and blue DN from the camera is proportional to the exposure E_v defined by the camera settings. The large number of points that was used to determine that curve (58 pictures x 45 samples per pictures = 2610 samples of different intensities) shows that this relationship is valid for a large range of sample intensity. The behaviour of the camera is proportional to the actual luminance, when 10% more light is let

into the camera, the estimated luminance increases by 10%.

In other words and applied to the snow reflectance estimation, it means that when snow is more or less bright (as defined by the CIE luminance Y) than a reference surface, the same can be inferred from its absolute luminance. Once again, since the reflectance will be determined in relation to a reference surface of known reflectance, the "relativeness" of the CIE luminance Y is not an issue. The reliability of this linear regression ($R^2 = 0.96$) is also very important since it means that it can be used in various light conditions.

So from now on, the absolute luminance L is defined as the ratio between the CIE luminance Y and an unknown coefficient b_T. By applying this finding to Equation 23, a new estimation of the snow reflectance can be done from the CIE luminance Y instead of the absolute luminance L. And from the following equation it can be seen that the coefficient b_T does not affect the reflectance estimation.

$$\overline{HDRF}_{vis,snow}(\theta_0, \phi_0, \theta', \phi', \lambda) = \overline{HDRF}_{vis,ref} \frac{Y_{snow}(\theta_0, \phi_0, \theta', \phi')}{Y_{ref}} \tag{27}$$

9.2 Fieldwork Campaign

The experiment was conducted on the 26^th of April 2015. As already mentioned, heavy snowfalls in the previous days and low temperatures prevented the snow from metamorphism and therefore from loosing its reflectance. The air temperature was -10^o and the sky was clear with a thin and sparse layer of moist dragged by strong winds. The light conditions were unstable and therefore not optimal. The snow area selected to be surveyed and the reference surface are shown in Figure 49.

The drone was flown for four minutes, between 11:36 and 11:40, acquiring 24 usable pictures. In total, six spectral measurements of the snow reflectance were taken with the ASD FieldSpec 4 spectroradiometer: three of them were taken before the flight and the rest right after. The spectral reflectance are given in relative units to the reflectance of a reference surface which was a 98% reflective Lambertian surface. In Figure 55 are plotted the relative reflectance of the snow patch as the average of the three measurements done before and after the flight.

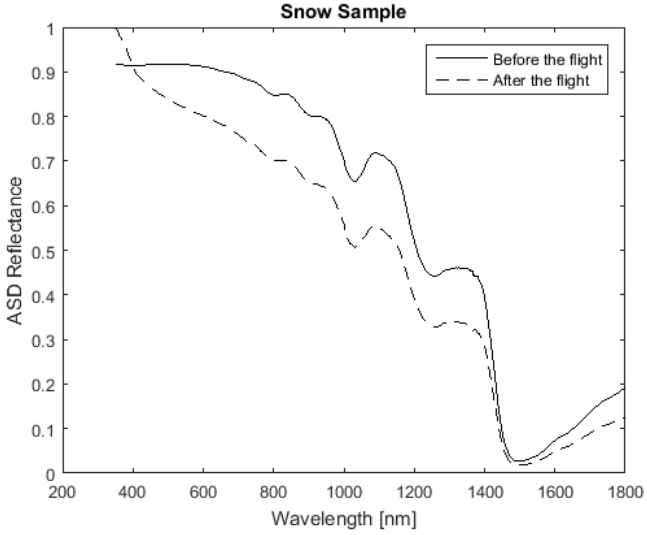

Figure 55: Erroneous measurement of snow spectral reflectance taken at four minutes interval before and after the flight.

It can be observed that, according to this measurement, the snow reflectance significantly

changed during the flight, e.g. from 0.9 to 0.8 in the red wavelengths. However, such aa big change of reflectance during four minutes is not attributable to any natural process. Also the spectral reflectance curve measured after the flight shows great inconsistencies with higher absorption in the high wavelengths. Indeed the reflectance drops from 1 in the blue wavelengths to 0.7 in the near-infrared. Snow is expected to absorb (and reflect) the visible light independently to the wavelength (Warren, 1982), while the measurement indicates that snow would lead to a blue colour of the snow. Therefore it is reasonable to assume that the measurement is subjected to human error.

The snow spectral reflectance curve measured before the flight shows a normal behaviour. Nevertheless since the same procedure was followed during both measurements, severe doubts arise on the reliability of this first measurement.

As a consequence, none of the spectral measurements of snow were used assuming that they were all equally subjected to doubts. The reflectance estimated from digital images were thus validated by the presence of other Lambertian surfaces of known reflectance (not used as reference) in the pictures.

9.2.1 Snow Reflectance Estimation from Single Digital Images

Once the 17 selected pictures uploaded in Matlab and corrected for the vignetting error. The areas of interest (snow patch, reference Lambertian surface and validation Lambertian surface), shown in Figure 49, are selected in each picture and the mean DN for the red, green and blue channels within the area along with their standard deviation are calculated. The reflectance of the snow patch and validation Lambertian surface are then calculated according to Equation 24. Table 16 presents the estimated reflectance values of the snow patch and of the validation Lambertian surface.

Table 16: Estimated reflectance of the same snow patch and of a 10% reflective Lambertian surface as calculated from the digital images taken from the UAV. The uncertainty on the reflectance value is given by Equation 26

Picture ID	Snow Patch Estimated HDRF	Validation Surface Estimated HDRF
A-12	0.97 ± 0.06	0.14 ± 0.01
A-13	0.98 ± 0.08	0.14 ± 0.02
A-14	0.98 ± 0.08	0.14 ± 0.02
A-15	0.98 ± 0.06	0.15 ± 0.01
A-16	0.98 ± 0.06	0.16 ± 0.01
A-17	0.98 ± 0.05	0.16 ± 0.02
A-21	0.98 ± 0.08	0.15 ± 0.02
A-24	0.96 ± 0.04	0.16 ± 0.02
A-25	0.97 ± 0.04	0.16 ± 0.02
A-26	0.98 ± 0.05	0.13 ± 0.01
A-27	0.97 ± 0.04	0.15 ± 0.02
A-28	0.97 ± 0.05	0.17 ± 0.02
A-29	0.97 ± 0.07	0.17 ± 0.03
A-30	0.97 ± 0.05	0.21 ± 0.03
A-31	0.98 ± 0.04	0.20 ± 0.02
A-32	0.98 ± 0.05	0.20 ± 0.07
A-33	0.98 ± 0.04	0.25 ± 0.04

Though snow reflectance could not be measured properly using the spectroradiometer, Table 16 shows that snow reflectance estimations in qualitative agreement with the literature on fresh and clean snow. However, a direct comparison with values from the literature is impossible

due to the strong sensitivity of the snow reflectance with incidence angle and to the grain size, that was not measured on the field. It is thus difficult to quantify the deviation of this measurement. It can be seen from Table 16 that the estimated snow reflectance values do not vary significantly from picture to picture though they are taken from different angles. Further investigation should determine whether this is due to a small variability of the snow reflectance for the present observation angles or if the accuracy of the reflectance estimation is not enough to capture it.

The estimated reflectance of the validation Lambertian surface gives many information about the errors that applies to the present approach, but also on how to prevent them or remove them.

First, the estimated reflectance can be as far as 0.15 away from its real value of 0.10 and the Root Mean Square Error (square root of MSE, usual indicator of measurement deviation from real value) is 0.07 for the 17 observations which is relatively high for a real reflectance value of 0.10. Also, the reflectance is always overestimated which indicates a systematic positive bias of the estimation.

Second, the deviation from the expected reflectance value seems to increase with picture sequential number. It is due to the fact that, for the sequence of selected picture, the UAV was flying up and the camera was getting further from the Lambertian surface. It resulted in a decreasing number of pixels used for reflectance estimation as low as 10 pixels for picture A-33. As mentioned when assessing the sources of noise in digital images, the only way to remove random noise is to average the value of neighbouring pixels. If not enough pixels are used, the result will be more subject to deviation. It is clearly visible in Figure 56 where the pixels are obviously taking different values over the homogeneous Lambertian surface. This issue can be limited, if not removed, by defining a minimum number of pixel for the reflectance estimation.

A clear degradation of the observation can be observed when the number of pixels in the area of interest is lower than 50, i.e. between A-29 and A-30. By restricting the estimation to the pictures where the area of interest contains more than 50 pixels, as a first estimate, (first 13 pictures) the RMSE decreases to 0.05. Further investigation of the relation between measurement reliability and number of available pixels should be conducted. This increased deviation with camera's height does not apply to the presented snow reflectance estimation since equal pixels were selected from the snow patch in every pictures.

Third, it has to be noted the that the brightness of the validation Lambertian surface is significantly lower than the one of the snow. Since the camera settings were chosen in order to reduce blur in bright snow pictures the exposure was thus very low. It resulted in very low DN within the validation Lambertian surface as low as 9. It has been reported previously the different sources of noise and some of them depend on the exposure (Shot Noise) and some do not. At this level of pixel brightness, the noise will inevitably appear relatively stronger compared to the original signal. For an example, the Signal to Noise Ratio (SNR), as defined by the ratio between the pixel value and the noise level, can be estimated for the shot noise to be $9/\sqrt{9} = 3$. It means that the signal (real image) is only three times higher than the noise. In comparison, a pixel of snow would count 200 DN and a SNR of 14. Therefore a digital camera will be more suitable to estimate reflectance over a bright area (less noise relatively to the signal) than over a dark one.

The RSME estimated from the first 13 pictures can be compared with previous studies to contextualize the goodness of the method. Hakala et al. (2010) and Corripio (2004) achieve a value of 0.02. However, Corripio (2004) reports that the maximum error obtained is 0.065. Therefore, considering that this single validation point is obtained for a high SNR, the result obtained is compatible with literature data. However, a more extensive validation is necessarily required to properly assess the goodness of the method.

Table 17 shows the red, green and blue DN recorded for the different surfaces of interest

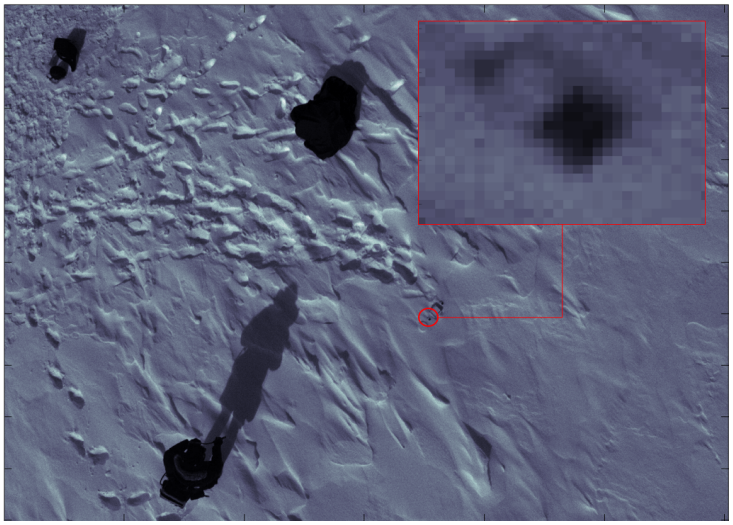

Figure 56: Close view of the validation Lambertian surface in picture A-29. The surface, normally homogeneous, appears to be affected by noise.

and their reasulting relative luminance Y along with their estimated reflectance from picture A-25. The uncertainty propagation is done accordingly to Equation 26. It can be noticed the difference in red, green and blue DN between the 10% reflective Lambertian surface and the snow.

Table 17: Average DN, relative luminance Y and estimated reflectance $HDRF$ along with their uncertainty as measured on the two Lambertian surfaces and on snow sample from picture A-25. The luminance Y is evaluated according to Equation 14, while the reflectance is evaluated according to Equation 24. The green DN used in the calculation is the average of the two green channels.

	Red	**Green**	**Blue**	**Y**	**HDRF**
		$\overline{DN} \pm \sigma$		$\overline{Y} \pm \sigma_Y$	$\overline{HDRF} \pm \sigma_{HDRF}$
98% Lambertian surface	85 ± 4	191 ± 6	168 ± 6	167 ± 6	Reference
10% Lambertian surface	14 ± 2	30 ± 3	27 ± 4	26 ± 2	0.16 ± 0.02
Snow patch	83 ± 4	189 ± 6	170 ± 6	165 ± 6	0.97 ± 0.04

The uncertainty on the reflectance estimation is calculated from the standard deviation of the red, green and blue DN and using Equation 26. It represent in average 5% of the snow reflectance estimation and less for the validation Lambertian surface. It is clearly correlated with the camera height (increasing with picture sequential number) and thus with the number of pixels used in the estimation. In other terms, the variability of the red, green and blue DN in the areas of interest (both considered homogeneous) increases with the number of pixels that are used to describe the surface. Similar conclusions are obtained from the next section. However, due to time limitation, this behaviour could not be addressed.

It can be concluded from this experiment that the reflectance estimation method should need further testing and validation, especially for the ranges of brightness that can take a snowy surface. The fact that the estimated reflectance of the snow does not significantly change from picture to picture could be a proof of the stability of the estimation. But once again the estimation of the snow reflectance with conventional methods should be compared to the estimated value. Also, the relation between estimation's uncertainty and the number of pixels used for the estimation should be further investigated.

9.2.2 Variability of Luminance Estimation in Overlapping Pictures

From the all the pictures taken during the flight, 20 pictures display the reference Lambertian surface. The relative luminance Y of the 98% reflective Lambertian surface is then calculated for these pictures. The calculation was based on 50 pixels randomly distributed within the surface. Figure 57 presents the estimated luminance Y of the reference Lambertian surface in the different pictures. It can be seen that they are significantly different from one other.

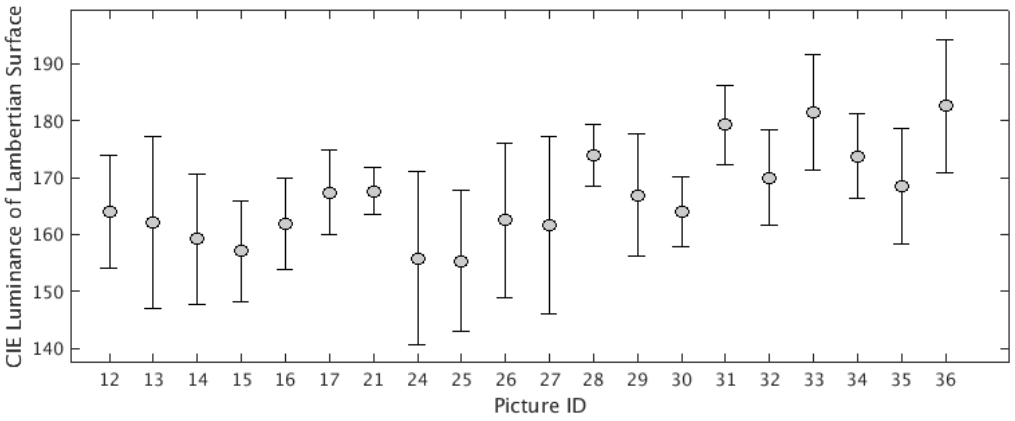

Figure 57: Plot of the estimated relative luminance Y of the reference Lambertian surface in 20 different pictures. Error bars are the standard deviation of the measurement.

The fact that the luminance of the reference surface increases with photo sequential number indicates that, since the UAV had an upward movement during the experiment, the higher the camera is, the brighter the pixels on the reference surface. To visualise this behaviour the calculation of the distance between camera and reference Lambertian surface.

This was done by computing the snow surface 3D model from the 52 pictures acquired during the flight using the Structure from Motion method and the software Agisoft (Westoby et al., 2012). This technique uses matching patterns on the pictures to recreate a 3D model of the scene, that is scaled on a local reference system. This allows to retrieve the 20 camera positions relatively to the reference surface. UAV flight height was calculated to range from 1.6 to 7.5 meters above the snow surface. Then the estimated luminance of the Lambertian surface could be plotted versus the distance between camera an Lambertian surface as displayed in Figure 58.

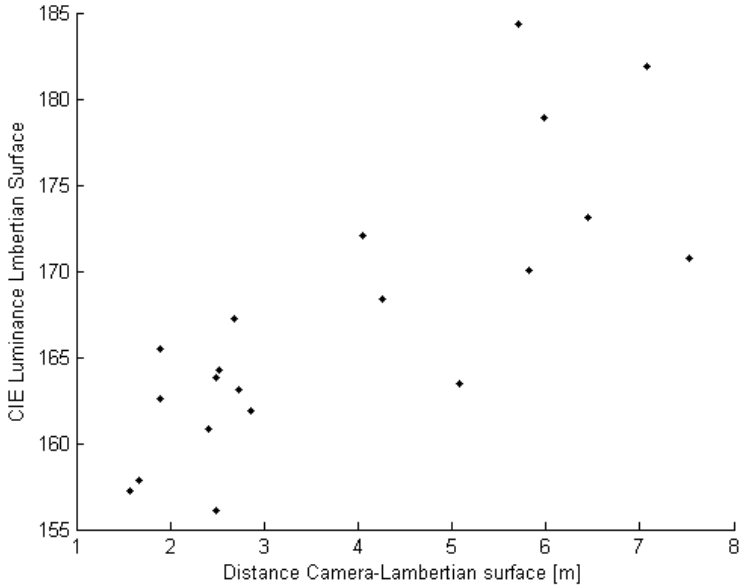

Figure 58: Scatter plots between estimated CIE luminance Y of the reference Lambertian surface and the distance between camera and observed surface for different pictures. A clear elevation trend is visible and a linear fit between x and y shows a R^2 of 0.66.

This dependence of luminance observation on the distance between camera and the object of measurement was not expected.

A first explanation addresses the different footprint of a pixel in the picture. Indeed the luminance observed by one pixel is not punctual but is done for the whole surface that is covered by the pixel. If the ideal luminance is defined as the luminous intensity emitted in a specific direction by an small elementary surface (unit cd/m^2), the one observed by the pixel is dependant on the area that represent the pixel and that has a non-negligible area. Therefore a pixel covering a larger area will lead to measuring more luminance than a pixel of small footprint. Since the footprint is a function of elevation, the trend observed in Figure 58 is natural and indicates need of a compensation for the different pixel footprints in the pictures. However, investigation of this dependence of luminance measurement to the pixel footprint could not be conducted due to time limitation. In future work, and in order to describe how the luminance observation varies from picture to picture, this effect should be explicated and corrected.

A second explanation can be made considering Figure 57 where luminance estimations are presented in chronological order. Therefore it indicates that the luminance estimation increases also with time. Whether the luminance estimation is dependant on elevation or on time could have been determined by flying the drone up then down above the target. However the experiment was stopped after the UAV reached its highest position. Thus the trend in luminance cannot be addressed to one or the other variable. It should be noted that the changing light conditions during the experiment could explain a trend in time. Though the weather conditions during the experiment can be suspected of such changing conditions, no mean could be found to assess if it was the case. It is recommended that future testing of this method should be conducted in constant light conditions.

10 Conclusion and Recommendations

The present work consist in a preliminary study of a new approach to estimate snow reflectance from aerial digital pictures. Some of the experiments that were conducted showed encouraging results while others did not give the expected result.

The calibration process showed that the CIE relative luminance Y, calculated from the DN of a set of pixels in a digital image was proportional to the absolute luminance L. This finding allows to use the camera as a reliable tool to measure luminance relatively to a reference level. It was conducted with basic equipment and did not require complex calculation nor determining the camera spectral sensitivity. In that way the proposed calibration gives satisfactory results from a simple and accessible protocol.

Other experiments allowed to quantify different sources of errors and noise. Vignetting effect was successfully calculated and removed from the pictures. Dark current Fixed Pattern Noise and random noise were quantified and appear to have little impact on the reflectance estimation. Shot noise was determined to be the most relevant source of noise in the conditions for which snow reflectance is estimated. Its effect was modelled as a function of pixel intensity, which allows to estimate reflectance measurement.

During the fieldwork in Western Greenland, aerial digital pictures of snow could be taken from an Unmanned Aerial Vehicle. By using a reference surface of known reflectance it was possible to estimate the Hemispherical Directional Reflectance Factor of a snow patch. This value ranged from 0.97 to 0.98 with an uncertainty of 0.04 to 0.08. However, the spectral reflectance of the snow patch measured on the field with a spectroradiometer were discarded due to human mistake and so no direct validation of the snow reflectance estimation could be made.

Another attempt to assess the quality of the reflectance estimation was done by estimating the reflectance of a 10% reflective Lambertian surface in different pictures. The deviation between reflectance estimation and real value led to a Root Mean Square Error of 0.05. It is within the range of error obtained in other studies (Corripio et al. (2004) had a maximum error of 0.06 on snow reflectance) but is relatively high compared to the real reflectance of the validation surface. Though this experiment did not discarded or validated the presented method, it allowed show how the number of pixels used for reflectance estimation on one hand and the level of exposure on the other can affect the reliability of the reflectance estimation. A minimum number of at least 50 pixels was found necessary for a reliable reflectance estimation and it was observed that low brightness of the validation surface (i.e. low red, green and blue DN of its pixels) led to a relatively high level of noise and low Signal to Noise Ratio.

Eventually, the estimations of relative luminance of the reference Lambertian surface, used for reflectance calculation, are compared for 20 pictures in order to assess the variability of luminance estimation from picture to picture. These values are found significantly different from one picture to the other. It was found that there is an increase in luminance that can be due to either the increasing distance between target and camera or to the chronological order in which the pictures were taken. It was not possible to address this increase in luminance to a specific cause.

Since the presented study was conducted over a relatively short period, many topics will require further investigation in future work. The authors suggest the following actions for the testing and use of the presented method:

- In order to remove dark current FPN, dark frames should be taken before and after the measurement and the master dark frame should be calculated and subtracted from all pictures.

- The exposure should be set carefully. It has to maximize the exposure of the pictures in order to reduce the impact of noise but also to avoid blurry picture (especially if taken from a UAV) at any cost. Saturation of the image, as defined by an exposure that exceeds the capacity of the sensor to differentiate intensity levels, is also to be avoided.
- Further assessment of the snow reflectance estimation accuracy should be conducted by taking proper validation measurements of snow reflectance with a spectroradiometer or by applying the estimation method to a validation Lambertian surface of which reflectance value would be similar to the one of snow.
- The mapping of larger area will require an assessment of whether the reference surface is necessary in each picture. For that purpose, the cause that determined the increase in luminance of the reference surface measured during the flight needs to be assessed.
- Further investigations needs to made to assess whether the camera is sensitive enough to measure differences in reflectance linked to the view angles. If the method was sensitive enough, the localisation of the camera for the different pictures might also allow to extract the view angle for each reflectance measurement. In the case of snow, this could allow to gather a dataset of Hemispherical Directional Reflectance Factors from the snow and how snow reflects light depending on the viewing angle.
- Once several HDRF values acquired, they can be used to calculate the spectrally integrated visible albedo of snow which is of prime importance in climate modelling and energy balance.
- Eventually, the relationship between snow optical properties such as HDRF or albedo and its physical properties can be investigated. Related to its grain size according to Warren and Wiscombe (1980), the snow reflectance could be used to spot snow drift areas (such as done by Corripio et al. (2004)) or to infer further information about the property of the snow pack.

References

Terrengmodell svalbard, 2014. available at https://data.npolar.no/dataset/dce53a47-c726-4845-85c3-a65b46fe2fea.

Annan, A., Cosway, S. W., and Sigurdsson, T. Gpr for snowpack water content. In *Fith International Conference on Ground Penetrating Radar(Kitchener, Ontario, Canada)*, pages 465–476, 1995.

Balk, B. and Elder, K. Combining binary regression tree and geostatistical methods to estimate snow distribution in a mountain watershed. *Water Resources Research*, 36(1):13–26, 2000.

Bang, B., Nielsen, A., Sundsbo, P. A., and Wiik, T. Computer simulation of wind speed, wind pressure and snow accumulation around buidings (snow-sim). *Energy and buildings*, 21: 231–243, 1994.

Berry, R. and Burnell, J. *The Handbook of Astronomical Image Processing*. Willmann-Bell, Inc., 2006.

Brooks, P., Schmidt, S., and Williams, M. Winter production of co2 and n2o from alpine tundra: environmental controls and relationship to inter-system c and n fluxes. *Oecologia*, 110:403–413, 1997.

Bruland, O. and Cooper, E. Snow distribution and vegetation. In Kuhry, P., editor, *Proceedings of Arctic Feedbacks to Global Changen, Rovaniemi, Finland*, Rovaniemi Painatuskeskus Oy, Rovaniemi, Finland, 2001.

Bruland, O., Sand, K., and Killingtveit, A. Snow distribution at a high arctic site at svalbard. *Nordic Hydrology*, 32(1):1–12, 2001.

Bruland, O., Liston, G. E., Vonk, J., Sand, K., and Killingtveit, A. Modelling the snow distribution at two high arctic sites at svalbard, norway, and an alpine site in central norway. *Nordic Hydrology*, 2004.

CIE. In *Commission internationale de l'Eclairage proceedings*. Cambridge University Press, 1932.

Clark, M., Hendrikx, J., Slater, A., Kavetski, D., Anderson, B., Cullen, N., Kerr, T., Hreinsson, E. O., and Woods, R. Representing spatial variability of snow water equivalent in hydrologic and land-surface models: A review. *Water Resources Research*, 47, 2011.

Cline, D. Snow surface energy exchanges and snow melt at a continental midlatitude alpine site. *Water Ressources Research*, (33):689–701, 1997.

Colman, R., McAvaney, B., Frase, J., Rikus, L., and Dahni, R. Snow and cloud feedbacks modelled by an atmospheric general circulation model. *Climate Dyn.*, 9:253–265, 1994.

Corripio, J. Snow surface albedo estimation using terrestrial photography. *Int. J. Remote Sensing*, 25(24):5705–5729, 2004.

Corripio, J., Durand, Y., Guyomarc'h, G., Mérindol, L., Lecorps, D., and Pugliése, P. Land-based remote sensing of snow for the validation of a snow transport model. *Cold Regions Science and Technology*, (39):93–104, 2004.

Dadic, R., Mott, R., Lehning, M., and Burlando, P. Wind influence on snow distribution and accumulation over glaciers. *Journal of Geophysical Research*, 115, 2010. F01012.

Debevec, P. and Malik, J. Recovering high dyamic range radiance maps from photographs. In *ACM SIGGRAPH*, pages 369–378, 1997.

Dormann, C., McPherson, J., Araujo, M., Bivan, R., Bolliger, J., Carl, G., Davies, R., Hirzel, A., Jetz, W., Kissling, D., Kühn, I., Ohlemüller, R., Peres-Neto, P., Reineking, B., Schröder, B., Schurr, . M., and Wilson, R. Methods to account for spatial autocorrelaiton in the analysis of species distributional data: a review. *Ecography*, 30:609–628, 2007.

Dozier, J. A clear-sky spectral solar radiation model for snow-covered mountainous terrain. *Water Ressources Research*, 16, 1980.

Dozier, J. and Frew, J. Rapid calculation of terrain parameters for radiation modelling from digital elevation data. *IEEE Transactions on Geoscience and Remote Sensing*, 28(5), 1990.

Dozier, J., Bruno, J., and Downey, P. A faster solution to the horizon problem. *Computer and Geosciences*, 7(2):145–151, 1981.

Dymond, J. and Trotter, C. M. Directional reflectance of vegetation measured by a calibrated digital camera. *Applied Optics*, 36(18):4314–4320, 1997.

Eckerstorfer, M. and Christiansen, H. H. The 'high arctic maritime snow climate' in central svalbard. *Arctic, Antarctic and Alpine Research*, 43(1):11–21, 2011.

Elder, K., Michaelsen, J., and Dozier, J. Small basin modeling of snow water equivalence using binary regression tree methods. In *Biochemistry of seasonally snow-covered catchments*, 1995. (Proceedings of a Boulder symposium, July 1995) Publ. no.228.

Elder, K., Rosenthal, W., and Davis, R. Estimating the spatial distribution of snow water equivalent in a montane watershed. *Hydrological Processes*, 12:1793–1808, 1998.

Erhlich, A., Bierwirth, E., Wendisch, M., Herber, A., and Gayet, J.-F. Airborne hyperspectral observations of surface and cloud directional reflectivity using a commercial digital camera. *Atmos. Chem. Phys.*, (12):3493–3510, 2012.

Erxleben, J., k. Elder, and Davis, R. Comparison of spatial distribution of snow water equivalence in a montane watershed. *Hydrological Processes*, 2002.

Frew, J. *The Image Processing Workbench*. PhD thesis, Department of Geography, University of California, Santa Barbara, 1990.

Gittleman, J. and Kot, M. Statistics and a null model for estimating phylogenetic effects. *Systematic Zoology*, 39(3):227–241, 1990.

Grünewald, T., Stötter, J., Pomeroy, J., Dadic, R., Baños, I. M., Marturià, J., Spross, M., Hopkinson, C., Burlando, P., and Lehning, M. Statistical modelling of the snow depth distribution in open alpine terrain. *Hydrology and Earth System Sciences*, 17:3005–3021, 2013.

Hakala, T., Suomalainen, J., and Peltoniemi, J. I. Acquisition of bidirectional reflectance factor using a micro unmanned aerial vehicle and a consumer camera. *Remote Sensing*, (2):819–832, 2010.

Hartman, M., Baron, J., Lammers, R., Cline, D., Band, L., Liston, G., and Taque, C. Simulation of snow distribution and hydrology in a mountain basin. *Wat. Res. Res.*, 35(5):1587–1603, 1999.

Humlum, O. Modeling late 20th-century precipitation in nordeskiold land, svalbard, by geomorphic means. *Norwegian Journal of Geography*, 2002.

Humlum, O., Instanes, A., and Sollid, J. L. Permafrost in svalbard: a review of research history, climatic background and engineering challenges. *Polar Research*, 22:191–215, 2003.

Jaedicke, C. and Sandvik, A. The influence of drifting snow on the location of glaciers on western svalbard. *Geografiska Annaler*, 2001.

Jeadicke, C. *Drifting snow and snow accumulation in complex Arctic terrain - Field Experiments and numerical modelling.* PhD thesis, Geophysical Institute, University of Bergen, 2001.

Jeadicke, C., Thiis, T. K., and Bang, B. The snowdrift pattern around a small hill in the high arctic. *Proceedings of the 4th international conference on snow engineering, Trondheim, Norway*, 2000.

Kirkwood, R. B. and Sterne, J. Essential medical statistics (2nd edition). *Statistics in Medicine*, 27, 2005.

Knap, W. H. and Oerlemans, J. Narrowband and broadband conversion of landsat tm glacier albedos. *International Journal of Remote Sensing*, 1999.

Krause, P., Boyle, D. P., and Bäse, F. Comparison of different efficiency cirteria for hydrological model assessmnent. *Advances in Geoscience*, (5):89–97, 2005.

Kuhn, I. and Dormann, C. Less than eight (and a half) misconceptions of spatial analysis. *Journal of Biogeography*, 39:995–1003, 2012.

Lebourgeois, V., Bégué, A., Labbé, S., Mallavan, B., Prévot, L., and Roux, B. Can commercial digital cameras be used as multispectral sensors? a crop monitoring test. *Sensors*, (8):7300–7322, 2008.

Legendre, P. Spatial autocorrelation: Trouble or new paradigm. *Ecology*, 74(6):1659–1673, 1993.

Lehning, M., Völksch, I., Gustafsson, D., Nguyen, T., Stähli, M., and Zappa, M. Alpine3d: A detailed model of mountain surface processes and its applicationn to snow hydrology. *Hydrological Prcoesses*, 20:2111–2128, 2006.

Lehning, M., Löwe, H., Ryser, M., and N., R. Inhomogeneous precipitation distribution and snow transport in steep terrain. *Water Ressources Research*, 44, 2008. W07404.

Lehning, M., T., G., and M., S. Mountain snow distribution governed by an altitudinal gradient and terrain roughness. *Geophysical Research Letters*, 38, 2011. L19504.

Lelong, C., Burger, P., Jubelin, G., Roux, B., Labbé, S., and Bayet, F. Assessment of unmanned aerial vehicles imagery for quantitative monitoring of wheat crop in small plots. *Sensors*, (8): 3557–3585, 2008.

Liston, G. E. and Sturm, M. A snow transport model for complex terrain. *Journal of Glaciology*, 44:498–516, 1998.

Liston, G. E., R.B., H., Sturm, M., Hiemstra, C., Berezovskaya, and Tabler, R. Simulating complex snow distribution in windy environments using snow-tran-3d. *Journal of Glaciology*, 53(181):241–256, 2007.

Lloyd, C., Aurela, M., Bruland, O., Fowler, D., Friborg, T., Hansen, B., Harding, R., Hargreaves, K., Nordstroem, C., Laurila, T., Tuovinen, J.-P., Sand, K., and Vehvilainen, B. Final report of the land arctic physicl processes (lapp) project. 1999. Contract no. ENV4-CT95-0093.

Marks, D. and Dozier, J. Climate and energy exchange at the snow surface in the alpine region of sierra nevada. *Water Ressources Research*, (28):3043–3054, 1992.

Marks, D., Domingo, J., Susong, D., Link, T., and Garen, D. A spatially distributed energy balance snowmelt model for application in mountain basins. *Hydrological Processes*, 13:1935–1959, 1999.

Marsh, P. Snow cover formation and melt: recent advances and future prospects. *Hydrol. Process.*, 12:2117–2134, 1999.

Meza, P., Martin, C. S., Vera, E., and Torres, S. A quantitative evaluation of fixed-pattern noise reduction methods in imaging systems. Technical report, Center for Optics and Photonics (CEFOP), 2010.

Molotch, N., Colee, M., Bales, R., and Dozier, J. Estimating the spatial distribution of snow water equivalent in an alpine basin using binary regression tree models: the impact of digital elevation data and independant variable selection. *Hydrological Processes*, 19:1459–1479, 2005.

Neal, A. Ground penetrating radar and its use in sedimentology: principles, problems and progress. *Earth-Science Reviews*, 66:261–330, 2004.

Pomeroy, J., Marsh, P., and Gray, D. Application of a distributed blowing snow model to the arctic. *Hydrological Processes*, 11:1451–1464, 1997.

Porter, W. C., Kopp, B., Dunlap, J. C., and Bodegom, E. Dark current measurements in a cmos imager. *Sensor, Cameras and Systems for Industrial/Scientific Applications*, 2008.

Prokop, A., Schon, P., Vionnet, V., Naaim-Bouvet, F., Guyomarc'h, G., Durand, Y., Bellot, H., Singer, F., and Nishimura, K. A comparison of terrain-based parameter, wind-field modelling and tls snow depth data for snow drift modelling. *International Snow Science Workshop Grenoble*, pages 108–113, 2013.

Purves, R., Barton, J., Mackaness, W., and Sugden, D. The development of a rule-based spatial model of wind transport and deposition of snow. *Annals of Glaciology*, 26:197–202, 1998.

Roe, G. H. Orographic precipitation. *Annual Review of Earth and Planetary Sciences*, 33: 645–671, 2005.

Roy, G., Hayan, S., and Julian, W. Sky modelling from digital imagery. Technical report, University of Sydney, Murdoch University, 1998.

Sauter, T., Möller, M., Finkelnburg, R., Grabiec, M., Scherer, D., and Schneider, C. Snowdrift modelling for the vestfonna ice cap, north-eastern svalbard. *The Cryosphere*, pages 1287–1301, 2013.

Schwaebel, T., Menning, S., and Bunz, U. Photoscopy: Spectroscopic information from camera snapshots? *Chemical Science*, (5):1422–1428, 2013.

Sigernes, F., Dyrland, M., Peters, N., Lorentzen, D., Svensøe, T., Heia, K., Chernouss, S., Deehr, C., and Kosch, M. The absolute sensitivity of digital cameras. *Optics Express*, 17(22), 2009.

Therneau, T. M. and Atkinson, E. J. An introduction to recursive partitioning using the rpart routines. divsion of biostatistics 61, 1997.

Thiis, T. K. A comparison of numerical simulations and full scale measurements of snow drift around buildings. *Wind and structures*, 3(2):73–81, 2000.

Tohsing, K., Schrempf, M., Riechelmann, S., Schilke, H., and Seckmeyer, G. Measuring high-resolution sky luminance distributions with a ccd camera. *Applied Optics*, 52(8):1564–1574, 2013.

Ulaby, F., Moore, R., and Fung, A. *Microwave remote sensing, Active and passive*, volume III. Addison-Wesley Pub. Company, 1986.

Van Der Wal, R., Madan, N., Van Lieshout, S., Dormann, C., Langvatn, R., and Albon, S. Trading forage quality for quantity? plant phenology and patch choice by svalbard reindeer. *Oecologia*, 123:108–115, 2000.

Wadsworth, editor. *Classification and Regression Trees*. Belmont, 1984.

Warren, S. Optical properties of the snow. *Reviews of Geophysics and Space Physics*, 20(1): 67–89, 1982.

Warren, S. and Wiscombe, W. A model for the spectral albedo of snow. ii: Snow containing atmospheric aerosols. *Journal of Atmospheric Sciences*, 37:2734–2745, 1980.

Westoby, M., Brasington, J., Glasser, N., Hambrey, M., and Reynolds, J. 'structure-from-motion' photogrammetry: A low-cost, effectuve tool for geoscience applications. *Geomorphology*, 2012.

Winstral, A. and Marks, D. Simulating wind fields and snow redistribution using terrain-based parameters to model snow accumulation and malt over a semi-arid mountain catchment. *Hydrological Processes*, 16:3585–3603, 2002.

Winstral, A., Elder, K., and Davis, R. Spatial snow modeling of snow-redistributed snow using terrain based parameters. *Journal of hydrometeorology*, 3:524–538, 2002.

Winstral, A., Marks, D., and Gurney, R. Simulating wind-affected snow accumulations at catchment to basin scales. *Advances in Water Ressources*, 55:64–79, 2013.

Winther, J., Bruland, O., Sand, ., Gerland, S., Marechal, D., B.Ivanov, Glowacki, P., and König, M. Snow research in svalbard - an overview. *Polar Research*, 22(2):125–144, 2003.

Wiscombe, W. and Warren, S. A model for the spectral albedo of snow. i: Pure snow. *Journal of Atmospheric Sciences*, 37:2712–2733, 1980.

Wüller, D. and Gabele, H. The usage of digital cameras as luminance meters. In Martin, R. A., DiCarlo, J. M., and Sampat, N., editors, *Digital Photography III*, volume 6502, 2007.

Wurzer, A., A., S., and P., F. Critical review of challenges and potentials for snow drift simulation. 2010. 2010 International Snow Science Workshop.

Zhang, C., Yao, S., and Xu, J. Noise in a cmos digital pixel sensor. *Journal of Semiconductors*, 2011.

A - Tools for Model Assessment

In the present study, several numerical models are introduced and though their application might be different, their quality is assessed using specific tools presented in this section.

Mean Square Error

The Mean Square Error (MSE) of a model is the average of the squared residuals (i.e. difference between the predicted and observed value):

$$MSE = \frac{1}{N}\sum_{i=1}^{N}(y_{model,i} - y_{obs,i})^2 \tag{28}$$

Where N is the number of samples, $y_{model,i}$ is the value predicted by the model and $y_{obs,i}$ is the observed value.

Mean Error

The Mean Error (ME) of a model is the average of the model's residuals:

$$ME = \frac{1}{N}\sum_{i=1}^{N} y_{model,i} - y_{obs_i} \tag{29}$$

The ME is useful to evaluate how much, on average, a model overestimates or underestimates the observations. The ME is also addressed as *bias* of the model.

R^2

The R^2, also called coefficient of determination or Nash-Sutcliffe efficiency (Krause et al., 2005) indicates the percentage of the variance of the data that a model can explain. Its value is evaluated as :

$$R^2 = 1 - \frac{MSE_{model}}{Var(y_{obs})} = 1 - \frac{\sum_{i=1}^{N}(y_{model,i} - y_{obs,i})^2}{\sum_{i=1}^{N}(y_{obs,i} - \overline{y_{obs}})^2} \tag{30}$$

Where $Var(y_{obs})$ is the variance in the observed data and MSE_{model} is defined by Equation 28. The R^2 allows to apprehend the error of the model (given by the MSE) with regards to the intrinsic variability of the data (given by the variance). It is also interpreted as the percentage of variance explained by the model. The R^2 can take values from one when there is optimal agreement between the model and the data to $-\infty$ when the MSE exceeds the data variance. Since the variance can be also seen as the MSE of a model that would give to each point the mean observed value (also called constant model, giving R^2=0), the R^2 also describes how much the investigated model is better than a constant model.

Prediction Interval

The prediction interval (*p.i.*) of a model is the range around a predicted value where the real value can be expected for a given probability. In the present study, the *p.i.* is used to give an estimation of the uncertainty of the model outcome based on the difference between predicted and observed values.

Here, the probability used is 95% and, assuming a normal distribution of the residuals. The prediction interval is, according to Kirkwood and Sterne (2005), calculated as:

$$p.i. = 1.96 \times \sqrt{\frac{\sum_{i=1}^{n}(y_{model,i} - y_{obs,i} - \overline{y_{model} - y_{obs}})}{n-1}} \tag{31}$$

Spatial Autocorrelation Indicator

Spatial autocorrelation is the general property of a distributed dataset for which samples show higher correlation (positive autocorrelation) or lower correlation (negative autocorrelation) with neighbouring samples than with more remote samples (Legendre, 1993). Ecological data such as snow depth is naturally subject to autocorrelation since neighbouring sites are likely to receive similar amounts of precipitation, wind or radiation and thus similar snow depth. In linear modelling however, spatial autocorrelation of the residuals is a violation of the assumptions that residuals are independent (Kuhn and Dormann, 2012). It can happen for example when a non-linear process is erroneously modelled as linear or when a spatially autocorrelated predictor is omitted from the model (Dormann et al., 2007). This violation results in unreliable estimation of the errors and coefficients of linear models (Kuhn and Dormann, 2012). In this study, spatial autocorrelation in the residuals of linear models used to calibrate Sx were diagnosed using the Moran's I index (Gittleman and Kot, 1990), that is defined for a dataset of N samples as:

$$I = \frac{N}{\sum_i \sum_j w_{ij}} \frac{\sum_i \sum_j w_{ij}(z_i - \overline{z})(z_j - \overline{z})}{\sum_i (z_i - \overline{z})^2} \tag{32}$$

where w_{ij} are the spatial weights, organized in a $N \times N$ matrix where:

$$w_{ij} = \frac{1}{distance(z_i, z_j)} \tag{33}$$

Moran's I varies, as shown in Figure 59 between -1 (more dispersed data than a random distribution) and 1 (more correlated data than a random distribution). For a precise assessment of autocorrelation, the Moran's I index needs to be compared with the Moran's I of a randomly distributed dataset of the same size. This comparison is used to test the null hypothesis that there is no significant spatial autocorrelation of the residuals. The output of this test is a p-value statistic. And if this p-value is lower than a significance of 0.05 the null hypothesis may be rejected meaning that there is significant spatial autocorrelation in the data (Gittleman and Kot, 1990). In this study, Moran's I and p-value are evaluated using the `R` package `ape`.

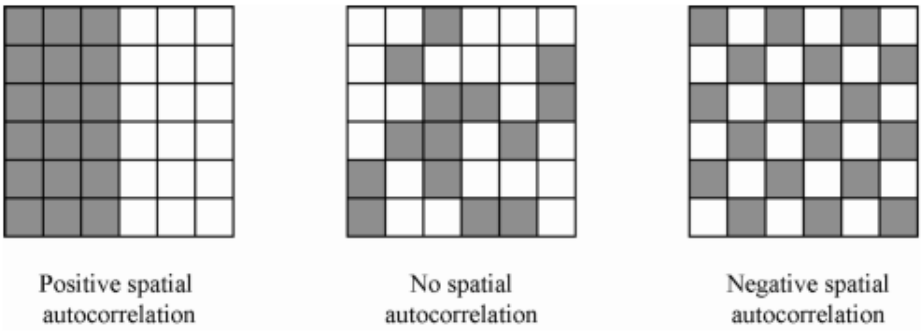

Figure 59: Illustration of positive, null and negative spatial autocorrelation. The Moran's I value for the first case would be 1, 0 and -1 from left to right.

B - Distribution Plots of the Predictors

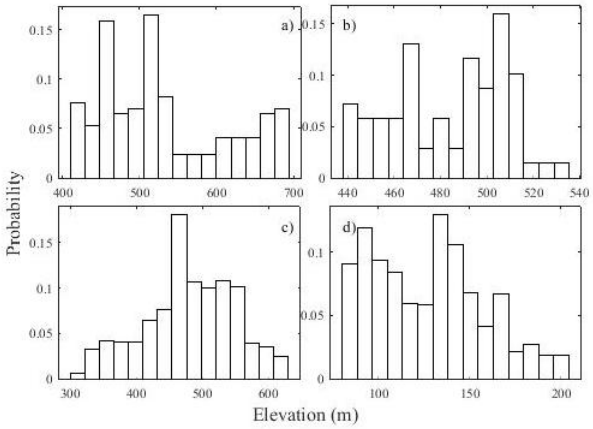

Figure 60: Distribution of samples elevations in a) Breinosa, b) Larsbreen, c) Longyearbreen and d) South Facing Slope.

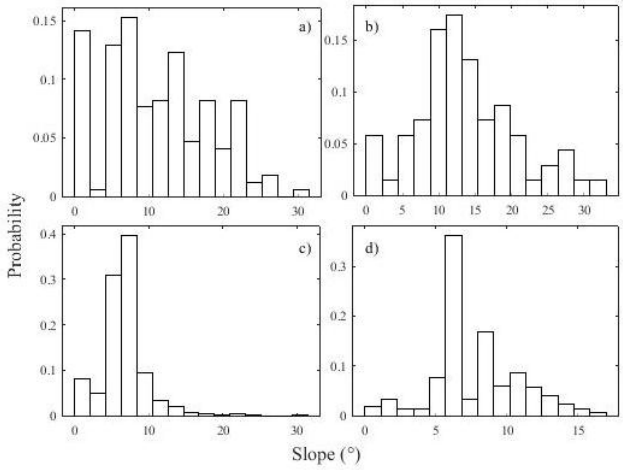

Figure 61: Distribution of samples slopes angles in a) Breinosa, b) Larsbreen, c) Longyearbreen and d) South Facing Slope.

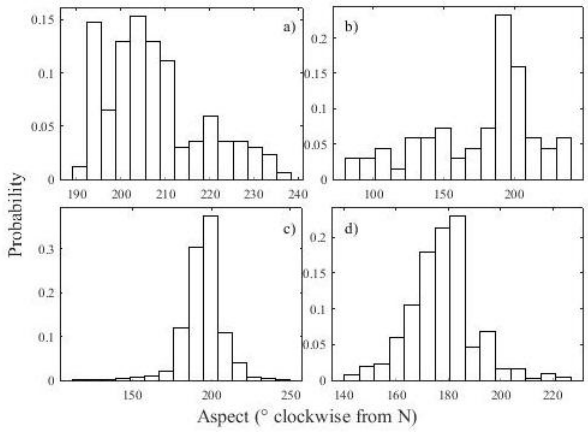

Figure 62: Distribution of samples aspects values in a) Breinosa, b) Larsbreen, c) Longyearbreen and d) South Facing Slope.

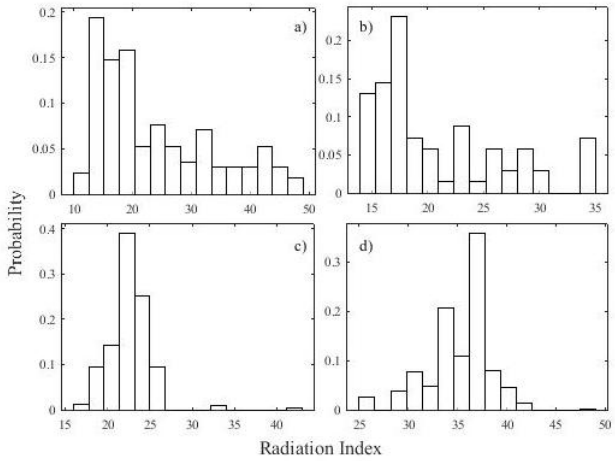

Figure 63: Distribution of samples radiation index values in a) Breinosa, b) Larsbreen, c) Longyearbreen and d) South Facing Slope.

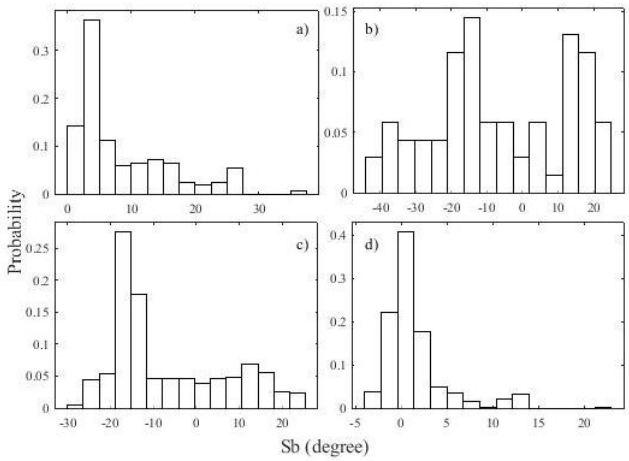

Figure 64: Distribution of samples Sb Drift values in a) Breinosa, b) Larsbreen, c) Longyearbreen and d) South Facing Slope.

C Diagnostic of Linear Models used for the Calibration of Sx

In the following figures are displayed the diagnostic plots of the different linear models that have been tried. They were used as a basis for the choice of which linear model (no transformation or with log transformation) would be used to compare the different Sx.

The first plot is the residual versus the fitted value. The residuals should have mean of zero and, ideally should not be higher or lower for a specific range of fitted value. In other word the average curve in red should be horizontal on zero.

The second plot is the QQplot and is commonly used to assess the normal distribution of a dataset (here the residuals). The standardized residuals (residuals devided by their standard deviation) should appear as close as possible to the dotted line.

The third plot, like the first one, also help to assess the independence of the residuals and to make sure that the standardized residuals do not take lower or higher values for specific ranges of fitted values.

The last plot is more suitable or the detection of outliers. It present the standardized residuals as function of their leverage, i.e. their effect on the model. An isolated point in a linear regression will for example have a high leverage. From that plot it can be assessed how much it affects the overall regression and whether it is far from its expected value. It can be then decided, for example if an isolated point that has both high leverage and high residuals, whether the point should be considered as outlier.

C.1 Diagnostic of the 5 m Models

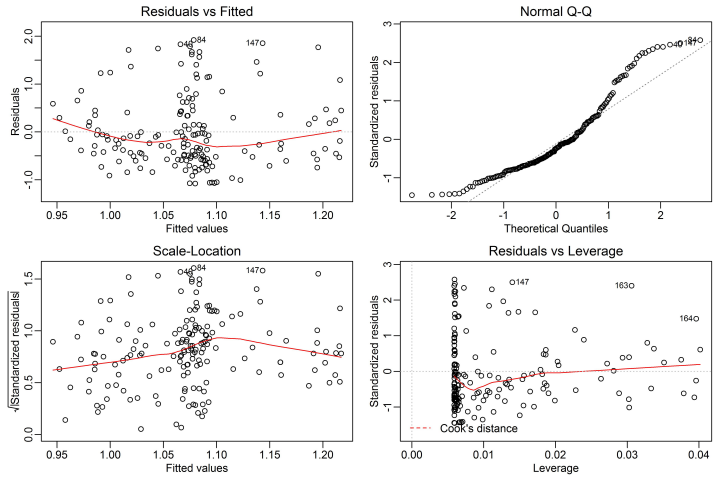

(a) no transformation

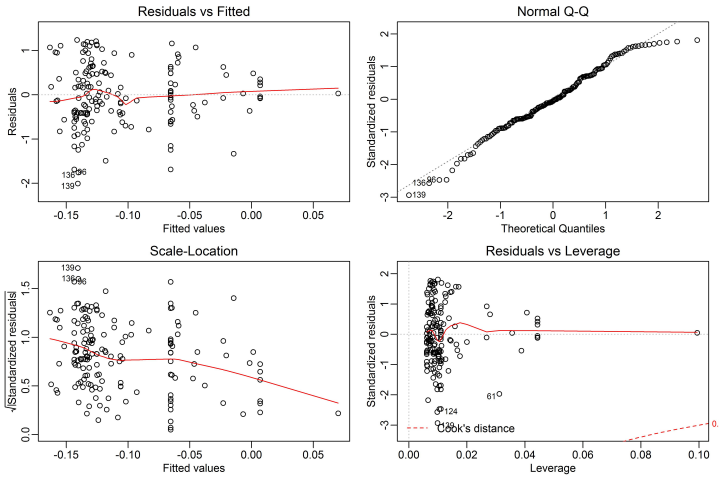

(b) log transformation

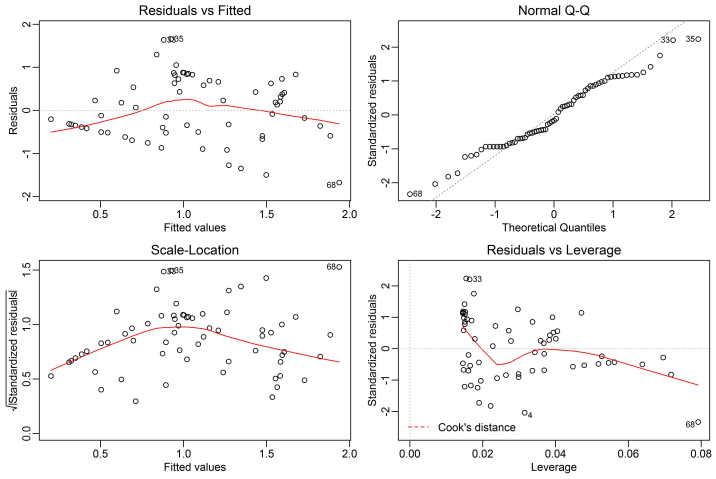

(c) no transformation

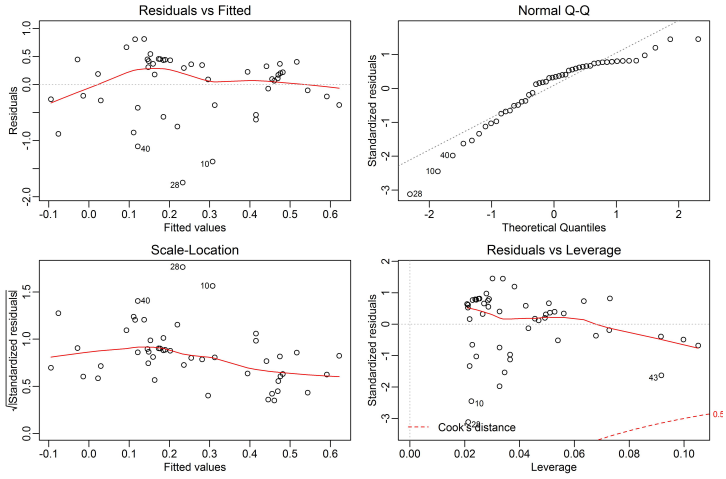

(d) log transformation

Figure 65: Diagnostic plot of the linear models built in Breinosa and Larsbreen for the 5m DEM.

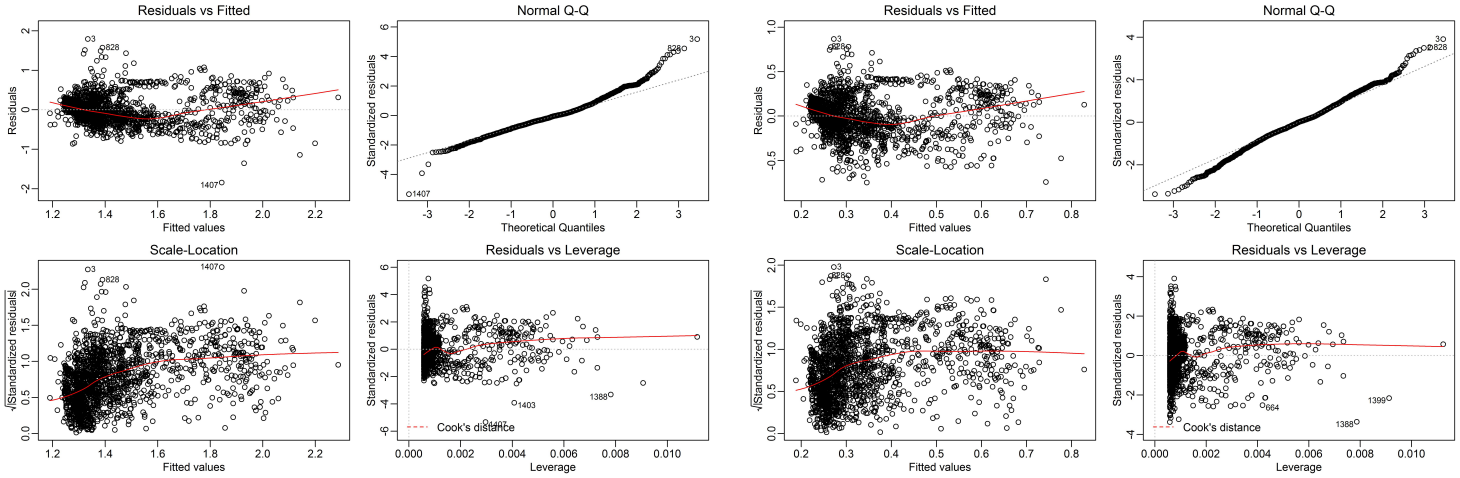

(a) no transformation

(b) log transformation

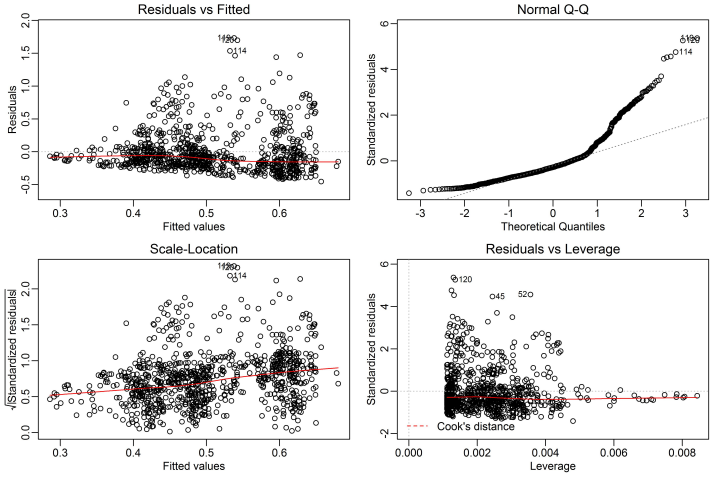

(c) no transformation

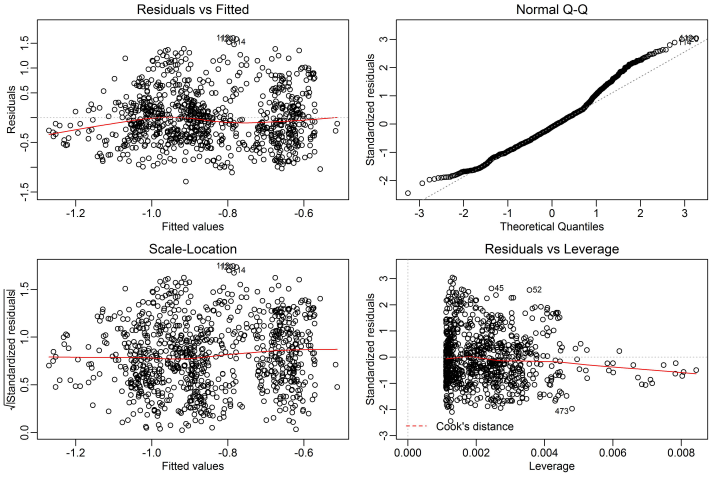

(d) log transformation

Figure 66: Diagnostic plot of the linear models built in Longyearbreen and SFS for the 5m DEM.

C.2 Linear models made with the 50m DEM

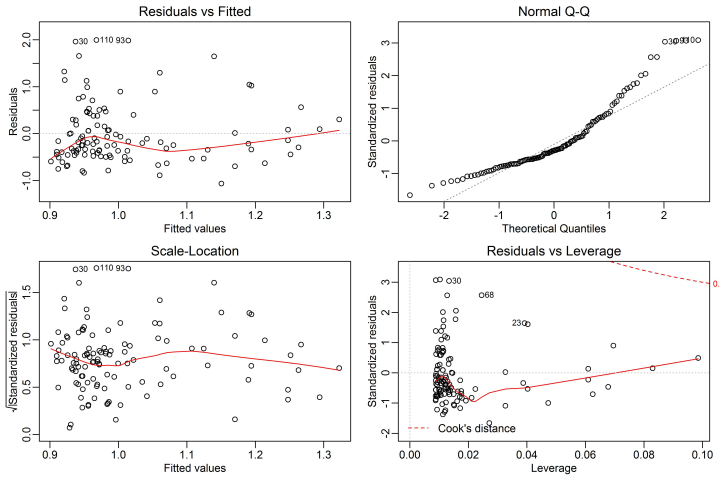

(a) no transformation

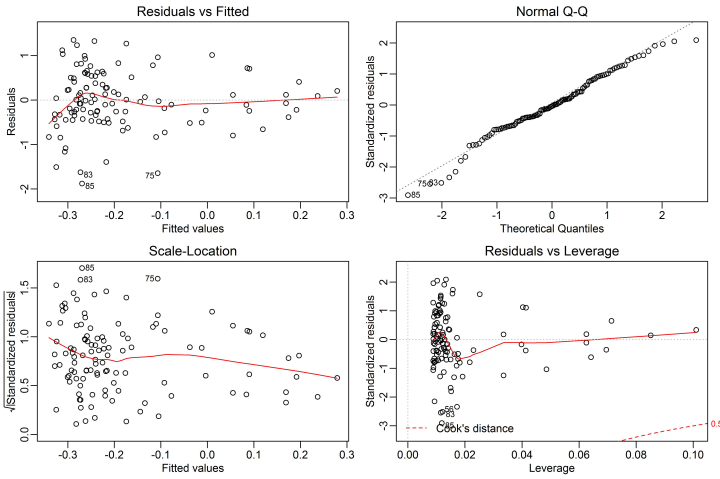

(b) log transformation

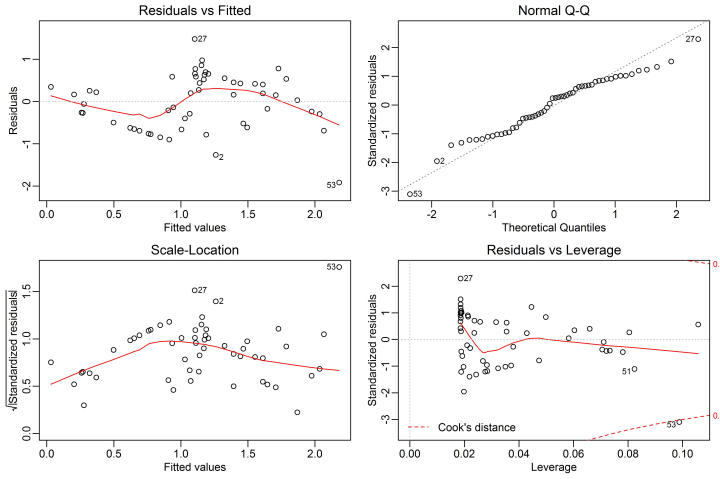

(c) no transformation

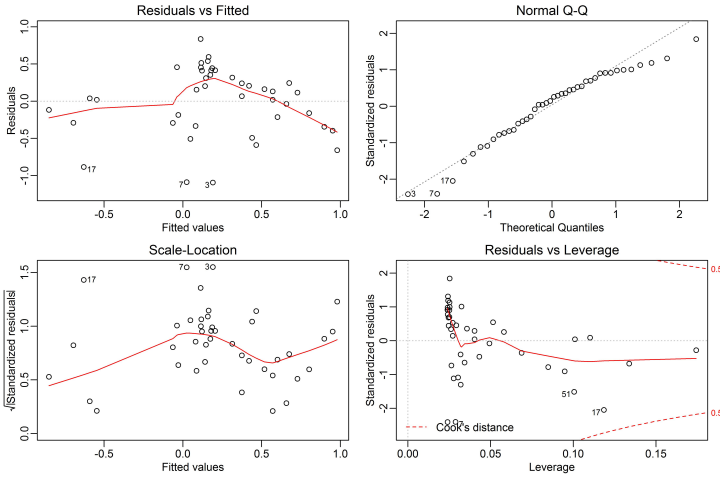

(d) log transformation

Figure 67: Diagnostic plot of the linear models built in Breinosa and Larsbreen for the 50m DEM.

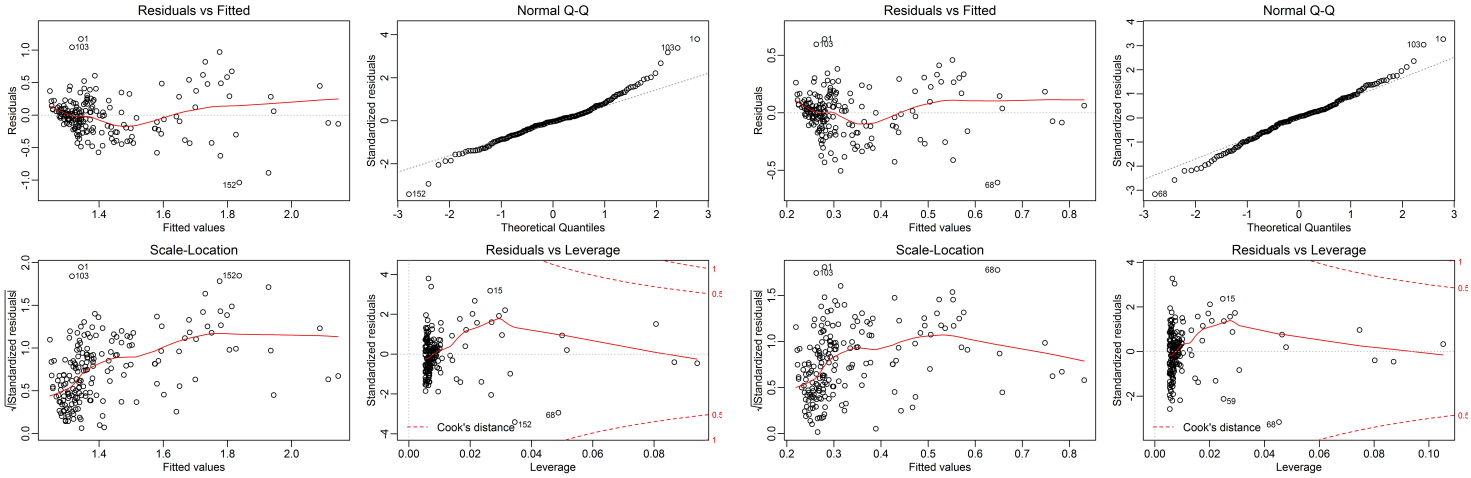

(a) no transformation

(b) log transformation

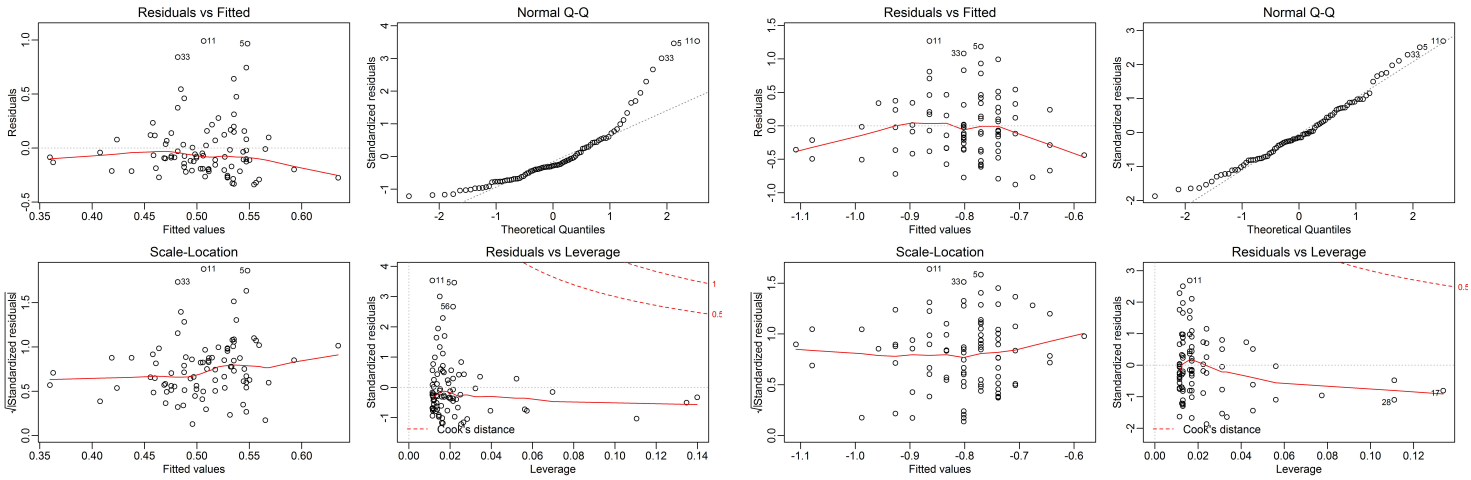

(c) no transformation

(d) log transformation

Figure 68: Diagnostic plot of the linear models built in Longyearbreen and SFS for the 50m DEM.

C.3 Linear Models between Snow Depth and $\overline{Sx}$ After Calibration

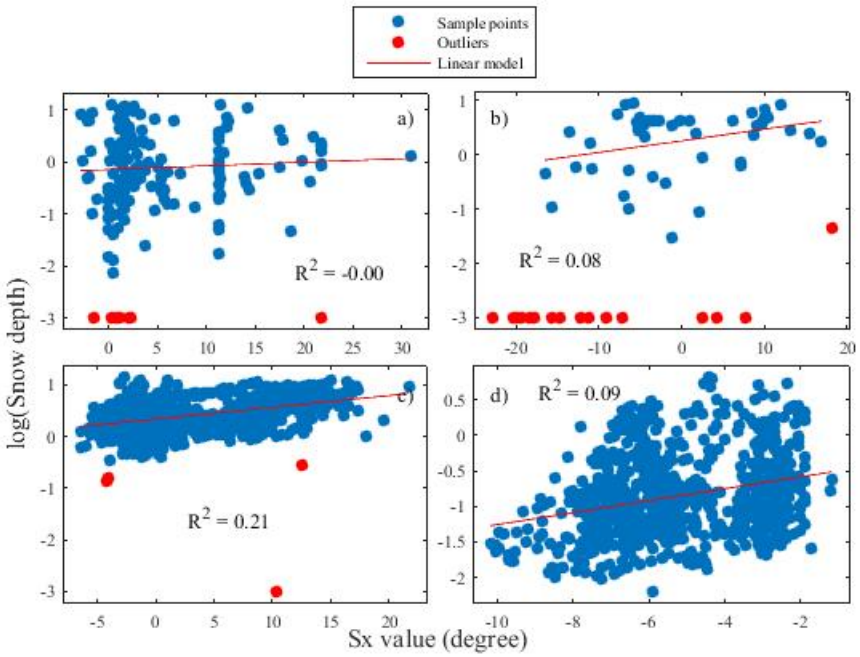

Figure 69: Calibration result of drift Sx in a) Breinosa, b) Larsbreen, c) Longyearbreen and d) South Facing Slope. As expected, a) does not show any correlation between Sx and Snow depth. In Larsbreen the Sx used is the one calculated with the optimal h and $dmax$ found in Longyearbreen. The outliers that have a log(snow depth) of -3 are the samples where measured snow depth was zero and this value was manually given to them so that they appear on the plot.

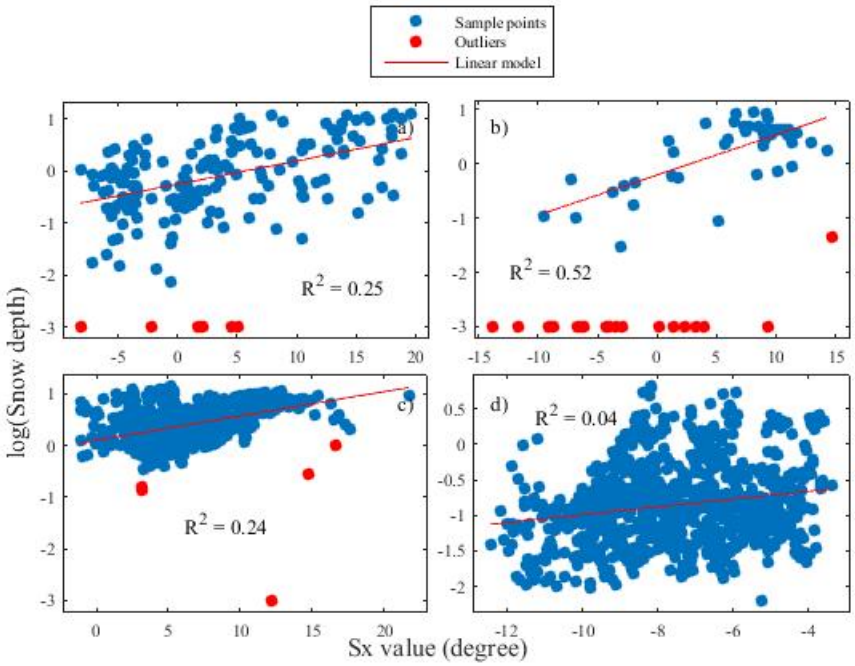

Figure 70: Calibration result of precipitation Sx in a) Breinosa, b) Larsbreen, c) Longyearbreen and d) South Facing Slope. In Larsbreen the Sx used is the one calculated with the optimal h and $dmax$ found in Longyearbreen. The outliers that have a log(snow depth) of -3 are the samples where measured snow depth was zero and this value was manually given to them so that they appear on the plot.

List of Figures

List of Tables